Novel Methods in Ball Bond Reliability Using In-Situ Sensing and On-Chip Microheaters

by

Samuel Kim

A thesis
presented to the University of Waterloo
in fulfillment of the
thesis requirement for the degree of
Master of Applied Science
in
Mechanical Engineering

Waterloo, Ontario, Canada, 2012

© Samuel Kim 2012

Author's Declaration

I hereby declare that I am the sole author of this thesis. This is a true copy of the thesis, including any required final revisions, as accepted by my examiners.

I understand that my thesis may be made electronically available to the public.

Samuel Kim

Abstract

Wire bonding is the process of creating interconnects between the circuitry on a microchip and PCB boards or substrates so that the microchip can interact with the outside world. The materials and techniques used in this bonding process can cause a wide variation in bond quality, so wire bond reliability testing is very important in determining the quality and longevity of wire bonds. Due to the fact that microchips are encased in protective resins after bonding and their substrates attached to the larger device as a whole, once any single wire bond fails then it could jeapordize the entire device as the wire bonds cannot be individually replaced or fixed. Current methods of reliability testing are lengthy and often destroy the entire sample in the process of evaluation, so the availability of novel non-destructive, real-time monitoring methods as well as accelerated aging could reduce costs and provide realistically timed tests of novel wire bond materials which do not form Intermetallic compounds (IMCs) as rapidly as Au wire on Al substrates.

In this thesis, five new chip designs for use in wire bond reliability testing are reported, focusing on the first joint made in a wire bond, called the ball bond. These chips are scaled either to test up to 55 test bonds simultaneously or just one at a time, introducing different requirements for microchip infrastructure capabilities, such as on-chip sensing/data bus, multiplexer, and switches able to operate under High Temperature Storage (HTS) which ranges from temperatures of 150-220 ºC. There are different heating requirements for each of these microchips, needing to be heated externally or containing on-chip microheaters to heat only the ball bond under test, and not the rest of the microchip or surrounding I/O pads. Of the five chip designs, sample chips were produced by an external company. Experimental studies were then carried out with two of these chip designs. They were specifically made to test novel methods of determining ball bond reliability using in-situ, non-destructive sensing, in real-time, while the ball bond undergoes thermal aging.

Pad resistance as an analysis tool for ball bond reliability is proposed in this thesis as a new way of evaluating ball bond quality and allows for the testing of electrical connection without the need for specialized measurement probes or difficult bonding processes that contact resistance measurements require. Results are reported for pad resistance measurements of a ball bond under very high temperature storage (VHTS) at 250 ºC, a temperature exceeding typical HTS ranges to accelerate aging. Pad resistance measurements are taken using the four-wire measurement method from each corner of the bond pad, while reversing current direction every measurement to remove thermo-electric effects, and then calculating the average square resistance of the pad from this value.

The test ball bond is aged using a novel on-chip microheater which is a N+ doped Si resistive heater located directly underneath the bond pad, and can achieve temperatures up to 300 ºC while not aging any of the I/O pads surrounding it, which are located ~180 µm away. A 50 Ω resistor is placed 60 µm away from the heater to monitor the temperature. The use of a microheater allows the aging of novel wire types at temperatures much higher than those permitted for microchip operation while thermally isolating the test bond from the sensing and power bonds, which do not need to be aged. Higher temperatures allow the aging process to be sped up considerably. The microheater is programmatically cycled between 250 ºC (for 45 min) and 25 ºC (for 15 min) for up to 200 h or until the pad resistance measurements fail due breakdown of the bonding pad. Intermetallic compounds forming between the ball bond and the pad first become visible after a few hours, and then the pad becomes almost completely consumed after a day. The pad resistance is measured every few seconds while the sample is at room temperature, and the increase in pad

resistance agrees with the fact that Au/Al IMC products are known to have much higher resistance than both pure Au or Al.

Also discussed are some aging results of Au wires and Pd coated Cu (PCC) wires bonded to Al bonding pads and aged at a temperature of 200 ºC in an oven for 670 h. The oven aged Au ball bonds also saw IMC formation on the surface of the bonding pad, much like the microheater tests. The PCC ball bonds became heavily oxidized due to lack of Pd on the surface of the ball, the wire portions did not oxidize much.

In conclusion, the new structures have been demonstrated to age ball bonds faster than with conventional methods while obtaining non-destructive data. Specifically, the new microheater ages a test bond at an accelerated rate without having an observable effect on the I/O connections used to monitor the test bond. Pad resistance measurements correlate to the aging of the test bond and ensure the electrical integrity of the joint is checked.

Acknowledgements

I wish to thank my supervisor Dr. Michael Mayer for his support and assistance during the duration of my Masters research. I learned a great deal about myself and the skills and work required to succeed. I would also like to thank MK Electron, Microbonds, and K&S for their support and making this project possible. Additional funding was also made possible by the Natural Sciences and Engineering Research Council of Canada (NSERC), Ontario Centres of Excellence (OCE), and Initiative for Automotive Manufacturing Innovation (IAMI), Ontario, Canada.

Table of Contents

Author's Declaration i
Abstract ii
Acknowledgements iv
List of Figures vii
List of Tables xi
1. Introduction 1
   1.1 Wire Bonding Background 1
   1.2 Wire Bonding Materials 3
   1.3 Wire Bond Reliability 3
   1.4 Literature Review on In-Situ Measurement 5
   1.5 Literature Review on Microheater Design 7
   1.6 Literature Review on Digital IC Design 7
   1.7 Motivation 9
   1.8 Objective 9
   1.9 Thesis Outline 9
2. Microchip Designs 10
   2.1 Parallel Microsensor Chip 11
   2.2 Parallel Microsensor Chip V2 (PM Chip V2) 18
   2.3 Thick-wire Microheater Chip 18
   2.4 Microheater and Underpad Sensor (MUS) Chip 18
   2.5 Microheater and In-Situ Measurement (MISM) Chip Design 35
3. Results of Microheater Experiment 42
   3.1 Equipment 42
   3.2 Software 43
   3.3 Test Materials 43
   3.4 Characterization 45
   3.5 Effect of Ball Bond on Calibration 46
   3.6 Temperature Control Methods 47
   3.7 Testing Procedure (HTS) 51
   3.8 Pad Resistance 51
   3.9 Microheater Post-Aging Drift 52
   3.10 Resistance Analysis 53
4. Results of PM Chip Aging 57
   4.1 PCC Ball Bond Analysis 57
   4.2 PCC Wire Analysis 58
   4.3 Gold Ball Bonds 58
5. Conclusions and Outlook 61
References 62
Appendix A: Matlab scripts for operation of microheater 64
Appendix B: PM Chip bonding diagram 71
Appendix C: Bonding diagram for PM chip v2 72
Appendix D: Bonding diagrams for thick-wire microheater chip 73
Appendix E: Bonding diagrams for the MUS chip 76
Appendix F: Bonding diagrams for the MISM chip 79

List of Figures

Fig. 1: Photograph of a ball-wedge bond head. Capillary, clamp, and gas nozzle are indicated. 1
Fig. 2: Photograph of the capillary sitting upside down in a capillary holder. The tip at the top has a diameter comparable to the wire being used in the bonding. 2
Fig. 3: Ball-wedge wire bonding process showing the cyclical procedure from steps (a) where the FAB is created from the wire tip to (h) the breaking off of the wire from the tail bond. 3
Fig. 4: SEM image of splash-off of a bonding pad. The ball bond was removed by being pulled off the bond pad. 4
Fig. 5: Example of a cross-section of a ball bond joined to a bonding pad [4]. 4
Fig. 6: Four-wire method for measuring contact resistance of a ball bond. [15] 5
Fig. 7: (a) Z-force and (b) x-force sensors in Wheatstone bridge configuration. Voltages and resistance labeled to correspond with Eq 1 and 2. 6
Fig. 8: Schematic of an n-p-n (NMOS) transistor. 8
Fig. 9: Layout of three switches side-by-side, taken from a CAD screenshot. These switches are made from a PMOS and NMOS transmission gate connected together. 8
Fig. 10: Photograph of the PM chip with all I/O pads bonded and two rows of test bonding pads with double ball bonds for contact resistance measurements. 11
Fig. 11: Schematic of PM chip's multiplexer digital controller being used to control which bonding pad and stress sensor set is connected to the microchip's data bus. 12
Fig. 12: Layout of the PM chip showing the location of the various components, the test pad numbering, and the I/O pads. 13
Fig. 13: PM chip's nine-input NAND gate made from two staggered five-input NAND gates. 14
Fig. 14: Example of a 3-bit decoder where it selects one of the 2N outputs to be "on" (0 state) depending on the input. In this case "3" is the input so the 4th output is on. 14
Fig. 15: Partial view of the PM chip's multiplexer layout. Shows the six inputs to the left and two of the NAND gates on the right half. 15
Fig. 16: Schematic of the decoder used on the PM microchip. 16
Fig. 17: Diagram showing a) the size of a single NAND gate, and why instead of a b) single 56 NAND gate multiplexer, the decoder was split into c) two 28-NAND gate multiplexers. 16
Fig. 18: Layout showing the X, Y, and Z sensors surrounding the octogonal test pad used in the PM chip. 17
Fig. 19: Layout of PM chip v2 rotated 90º counterclockwise. I/O pads including Gnd, Vdd, and Vd (digital power) shown. Test pads start numbering at 0 and progress along the rows until 49. 20
Fig. 20: Two power switches side-by-side on the PM chip v2, gating the microsensors from the power and GND rails. 21
Fig. 21: Bonding pads on PM chip v2 which are connected to the microsensor Vdd and Gnd after they go through the power switches. 22
Fig. 22: Microheater test structure on PM chip v2 to test pad #24's stress sensor operation by increasing the temperature on one side of the sensors in Wheatstone bridge

configuration, generating a differential signal. 23
Fig. 23: Schematic of a previous microheater design, the thick-wire microheater chip. 24
Fig. 24: MUS chip's structure 1: localized RTDs in a Wheatstone bridge and placement of sensing connections. Associated force sensors removed from schematic view for clarity. 25
Fig. 25: Location of Structure 1's components and associated pads on the MUS chip. M0-4 are the inputs to control the decoder, Vd is the digital power supply, Gnd is the chip ground, Vhigh and Vlow measure voltage being supplied to the Wheatstone bridge RTDs, Vs is the supply voltage for the stress sensors, Z, Y, and X pads pairs are for the stress sensors, Current is for the CCS for the RTDs, and Vleft and Vright measure the voltage signal from the Wheatstone bridge RTDs. 26
Fig. 26: Close-up view of MUS chip's structure 2: linear stress sensor and its 19 signal channels. 27
Fig. 27: MUS chip's structure 2: linear stress sensor with associated input and output pads. 28
Fig. 28: Structure 2's(a) position on the MUS chip, along with a (b) close-up of the test bond site and related components. Passivated bonding areas and RTD shown as well. 29
Fig. 29: The MUS chip's structure 4 has four local z-force sensors arranged to be accessible individually or as a Wheatstone bridge. Upper right sensor does not have a bond pad opening so can be bonded to repeatedly without having the bond pad stick. 30
Fig. 30: Location of structure 3: oversized stress pad with sensor components and associated pads on MUS chip. 31
Fig. 31: Diagram showing lateral cross section of microheater on MUS chip. 32
Fig. 32: Micrograph showing the MUS chip's structure 4: microheater and its bond connections to sub-structures. Overlaid with component outlines. 32
Fig. 33: Layout view of the MUS chip showing structure 4's (a) location on the chip of the microheater and (b) the I/O pads for all the sub-structures. 33
Fig. 34: The MUS chip's stucture 5 contains a flip-flop chain and associated switches connected to a linear stress sensor. 34
Fig. 35: High level design overview of the operation of the channel multiplexer in the MUS chip's structure 5. Uses DFFs to continuously switch between signals. 36
Fig. 36: MUS chip's high power switch used to gate connections to the ground and power supply. 37
Fig. 37: Layout of the entire MISM chip. 38
Fig. 38: Layout of an individual microheater on the MISM chip with each sub-component identified. 39
Fig. 39: MISM chip's off-bus microheater. Structure is completely independent from the rest of the microchip. 40
Fig. 40: Layout of three switches on the MISM side-by-side. The layout is rotated 90 degrees in this figure to conserve space. 41
Fig. 41: Setup used for running of microheater experiments. 42
Fig. 42: Layout and connections of equipment in the microheater setup. 43
Fig. 43: Diagram showing which pieces of equipment connect to which package pin

numbers for the microheater experiment. 44
Fig. 44: Photograph of the bonded sample TC5 (MUS chip), the curved edges of the package are due to the camera's lens warping straight lines. 45
Fig. 45: Example values obtained during power characterization of sample Q01. 47
Fig. 46: RTD and microheater temperatures at various power levels. Values in dashed box are used for the determination of the heater versus RTD temperature extrapolation, as non-linear effects are observed at higher temperatures. 47
Fig. 47: Schematic showing the modifications to how the heater's voltage was measured for sample TC3. These changes do not change the temperature characteristics, but would show a resistance offset compared to other samples due to the extra line resistance from the vias and portions of the N+ dopped Si directly beside the vias at the edges of the microheater. 48
Fig. 48: Plot showing the temperature vs power characterization of a microheater before a test ball bond was made (blue, solid) and after the ball bond was made (red, dashed). 49
Fig. 49: Schematic of the PID controller feedback loop. The PID Controller directly operates the Plant, which is the system which needs control, using the error signal between the actual value and the desired value to adjust the control signal going to the Plant. 49
Fig. 50: Step response the of sample Q01's microheater. 50
Fig. 51: Pad outline with isolines (thin, green) approximating electric field generated by the current (red arrow indicates current direction) across the two bottom corners of bonding pad during 4-wire resistance measurement. 51
Fig. 52: Plot showing the linear fits of the actual temperature and reported temperature of the RTD, which are different due to irreversible changes from being heated by the microheater. The reported temperature uses pre-aging characterization data (orange) and the actual temperature uses post-aging characterization data (blue)..........52
Fig. 53: Plot showing linear fits for the reported and actual derived temperatures for the microheater after aging. The reported temperature (orange) shows the derived temperature using characterized values before aging. The actual temperature (blue) shows the derived temperature after irreversible changes have occured, using the characterizations from after the aging experiment. 53
Fig. 54: Optical image of an Au ball bond on the microheater test pad before (a) and after (b) 24 h of aging. 54
Fig. 55: Pad resistance of sample TC5 during a VHTS test. Four phases were identified, (a) phase 1 is when the pad's Al is consumed to form IMCs, (b) phase 2 has a decrease in resistance, (c) phase 3 sees an increase in resistance again, before (d) phase 4 the pad resistance stabilizes until electrical failure occurs. 54
Fig. 56: Au ball bond after 150 h of VHTS. Pad has been completely consumed and progression of IMC formation is seen along the measurement lines of for the pad resistance measurement. 55
Fig. 57: Sample Q01 after 120 hours of aging. SEM images for (a) the surface shape, (b) backscattering to highlight gold-rich areas are shown, and (c) the micrograph of the same test bond, seen from above. 56
Fig. 58: Comparison of the PCC ball bond on pad 0 (a) and pad 4 (b) before and after aging. 57

Fig. 59: Scanning electron microscope image of a PCC ball bond after HTS. 58
Fig. 60: EDS analysis showing the oxygen, copper, and palladium concentrations on a PCC ball bond and the wire. 59
Fig. 61: Micrograph of the surface of PCC wire near the ball bond, after aging. 59
Fig. 62: SEM image of PCC wire after HTS. 60
Fig. 63: Gold ball bond after high temperature aging. 60

List of Tables

Table 1 Microchips for wire bond reliability studies discussed in this thesis, their capabilities, and their bonding diagrams 10
Table 2 List of changes to the PM chip v2 19
Table 3 Structures on the MUS chip 21
Table 4 Examples of digital multiplexer input values for te PM chip 23
Table 5 Truth table for a D-flip-flop using in MUS chip 35
Table 6 Thermal Characterization of Microheaters 46
Table 7 Power Characterization of Microheaters 46
Table 8 Thermal Characterization Differences 48
Table 9 Power characterization differences 48
Table 10 PID values for the microheater 50
Table 11 Before and after aging characterization of RTD and heater 52
Table 12 Resistivities of Au, Al, and their common IMC products [16] 55
Table 13 Pad and purposes for thick-wire microheater chip 75

1. Introduction

1.1 Wire Bonding Background

Wire bonding is a microjoining process where a first level electrical interconnect is made between a microchip and a package, allowing for the microchip to interact with the outside world. Wires are typically 20-100 µm in diameter and there are two types of wire bonding technologies, ball-wedge bonding and wedge-wedge bonding. Wedge-wedge bonding works by having the wire's tip be parallel to the metal surface and then physically joining the two with normal force and ultrasonics. This process can be done at elevated or room temperatures. Ball-wedge bonding, works by melting the tip of the wire into a ball which is joined to metal bonding pads as small as twice the wire width. Ball-wedge bonding has the advantage that the subsequent wedge bond can be made at any location 360º from the ball bond, while wedge-wedge bonding has to be done in the direction of the wire in the bonding head. Also due to the small angle between the wedge bond and chip surface, a wedge-wedge bond has greater possibility for short-circuits [1] and chips cannot be bonded as densely as with ball-wedge bonds.

The ball-wedge bonding head contains a wire feed, clamp, gas nozzle and capillary as seen in Fig. 1. The gas nozzle provides special gases for certain processes to improve the Free Air Ball (FAB) quality by preventing oxidation of the ball's surface during its formation. The capillary is typically made of ceramic and is a very high precision tube ending in a tip just slightly larger than the wire diameter. In Fig. 2 the capillary is shown in a capillary holder with the tip exposed.

The steps of the ball bonding process are shown in Fig. 3 as a schematic drawing of the wire, capillary tip, and wire clamp, not to scale. During this entire procedure, the package and microchip are held at a high temperature typically between 100-220 ºC to assist in the metal joining. In the

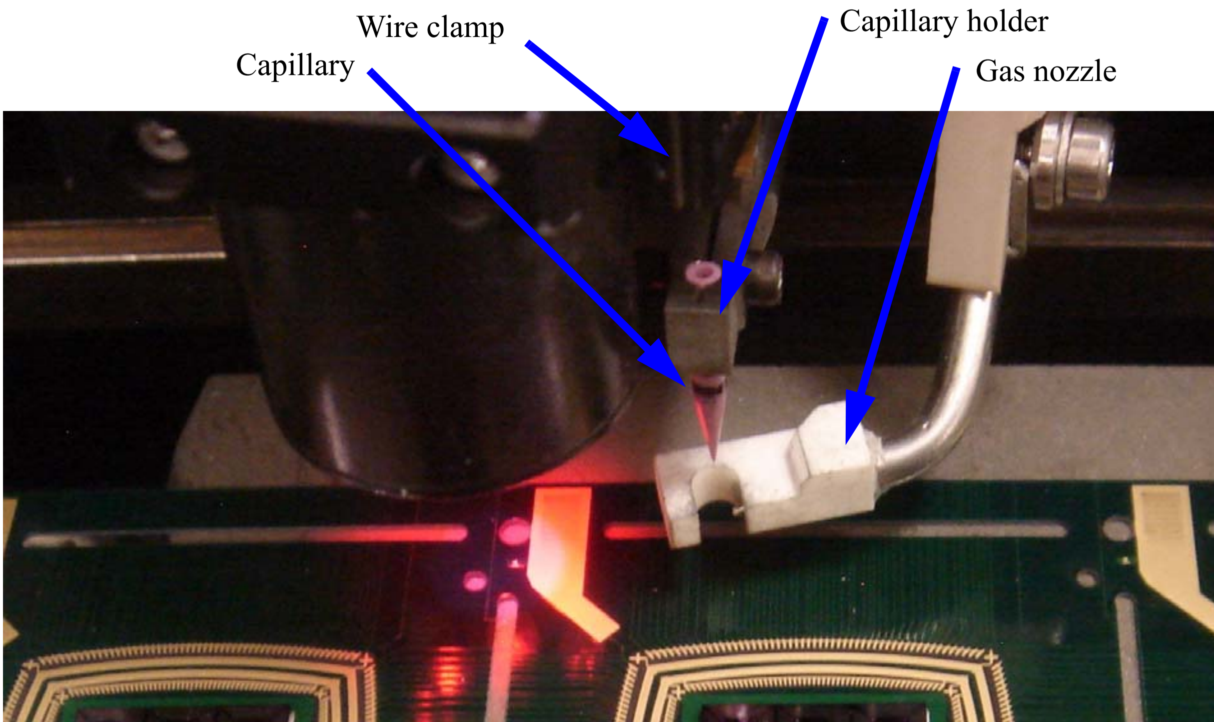

Fig. 1 Photograph of a ball-wedge bond head. Capillary, clamp, and gas nozzle are indicated. The capillary tip below the holder is approximately 1 cm in length.

first step, (a) the wire clamp is closed and the wire's tip is exposed to a high voltage spark from an electrode, melting it in a process called the Electric Flame Off (EFO). In step (b) the liquid metal's surface tension forms the FAB which quickly hardens. In step (c) the capillary descends onto a bonding pad where the metal joint is formed. In step (d), the capillary uses a combination of bond force (normal force, downwards) and ultrasonic vibrations (lateral to the surface) to make the joint between the ball and the bonding pad, which also deforms the ball, flattening it out. In step (e) the clamp is released and the wire is spooled while simultaneously moving the capillary in a specific pattern towards the wedge (tail) bond. This pattern helps create the arc of the wire between the ball and wedge bond, preventing close-by or overlapping wires from touching each other, the chip surface, or other components. In step (f) the tail bond is formed by joining the part of the wire folded under the capillary to a lead on the package, using normal force and ultrasonics. In step (g) the clamp is opened, the capillary moved upwards, and finally the clamp is closed again. Finally in step (h) the wire is broken at the tail bond by moving the bond head upwards while the clamp is closed. This new wire tip forms the next ball bond in this cyclic process.

The process parameters for making a ball bond are: ultrasonic % (a value proportional to the ultrasonic amplitude), substrate temperature, bond force amount, ultrasonic time, bond force time, and bonding gas. Ultrasonic forces are generated during the bonding stage as the capillary tip moves back-and-forth in the y-direction at microscopic distances. Ultrasonic and bond force times are applied in the 10 ms ranges. Ultrasonic % and bond force are what are typically optimized to obtain a good ball bond. These parameters alter the joint between the ball and the bonding pad, varying the amount of pad splash-off (e.g. Al flash), ball deformation, and the joint strength [2]. Splash-off is when the ultrasonic and bond force is sufficient to start pushing the bond pad's material from underneath the ball to the edges of the interface. An SEM image of splash-off, with the ball bond removed, is shown in Fig. 4. Wire bonds can be made on a variety of substrates such as Au, Pd, or Al (which can contain trace amounts of Cu or Si).

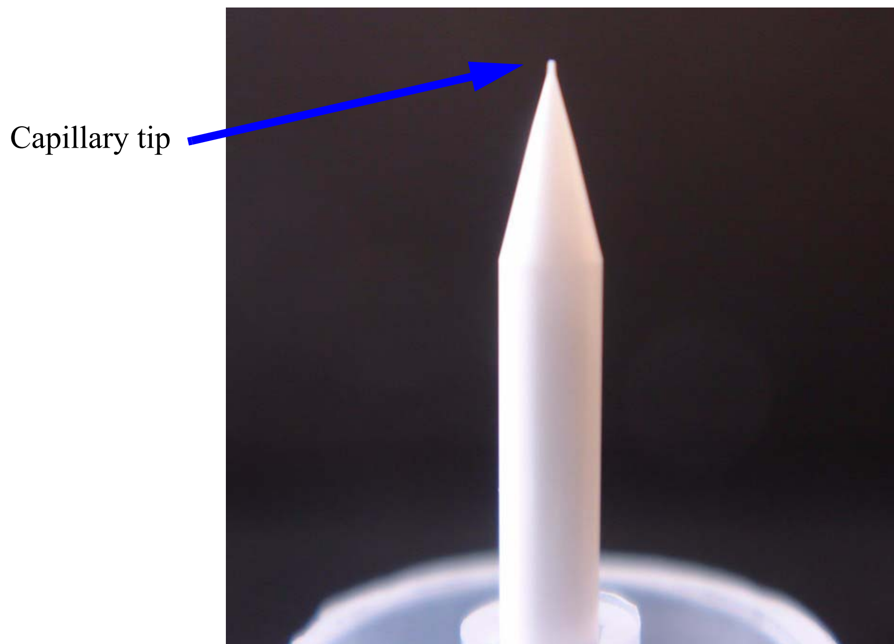

Fig. 2 Photograph of the capillary sitting upside down in a capillary holder. The tip at the top has a diameter comparable to the wire being used in the bonding.

1.2 Wire Bonding Materials

Gold has traditionally been the standard material used in wire bonding with approximately 150 tons used in the year 2004, three times more than the amount used ten years before that [3]. The advantages of gold were that it readily bonds to many bonding pad materials and is stable in the presence of different molding compounds or humidity. However, in the past 20 years the price of gold has increased from $400 USD per ounce to the modern price of over $1700 per ounce prompting manufacturers to search for alternative materials. Currently Ag, Cu, and Pd are being looked at as new materials in wire bonding, to either coat Cu wires or to replace Au completely as the new wire material [3-5]. Copper has the advantage of having better electrical and thermal properties than gold but is much harder, requiring larger forces to bond [6]. Copper oxidizes easily in air, so must be stored sealed or in a container with inert gas. When bonding the Cu FAB must also be kept from oxidizing using a shielding gas. Noble metals such as Pd reduce intermetallics compound (IMC) formation by having a low metal diffusion coefficient [4] making ideal coatings or even bonding surfaces. They are resistant to corrosion [7] and Au-Pd form a solid solution instead of IMCs at normal or even aging temperatures [8].

1.3 Wire Bond Reliability

Wire bond reliability is the study of determining which process parameters result in the longest lasting joint using different method of accelerated testing. If any of the wire bonds connecting a microchip to its package fail, then the entire microchip could become unusable and the entire product the microchip is part of could also fail. To reduce the costs of failed bonds manufacturers want to be able to determine the best bonding process parameters.

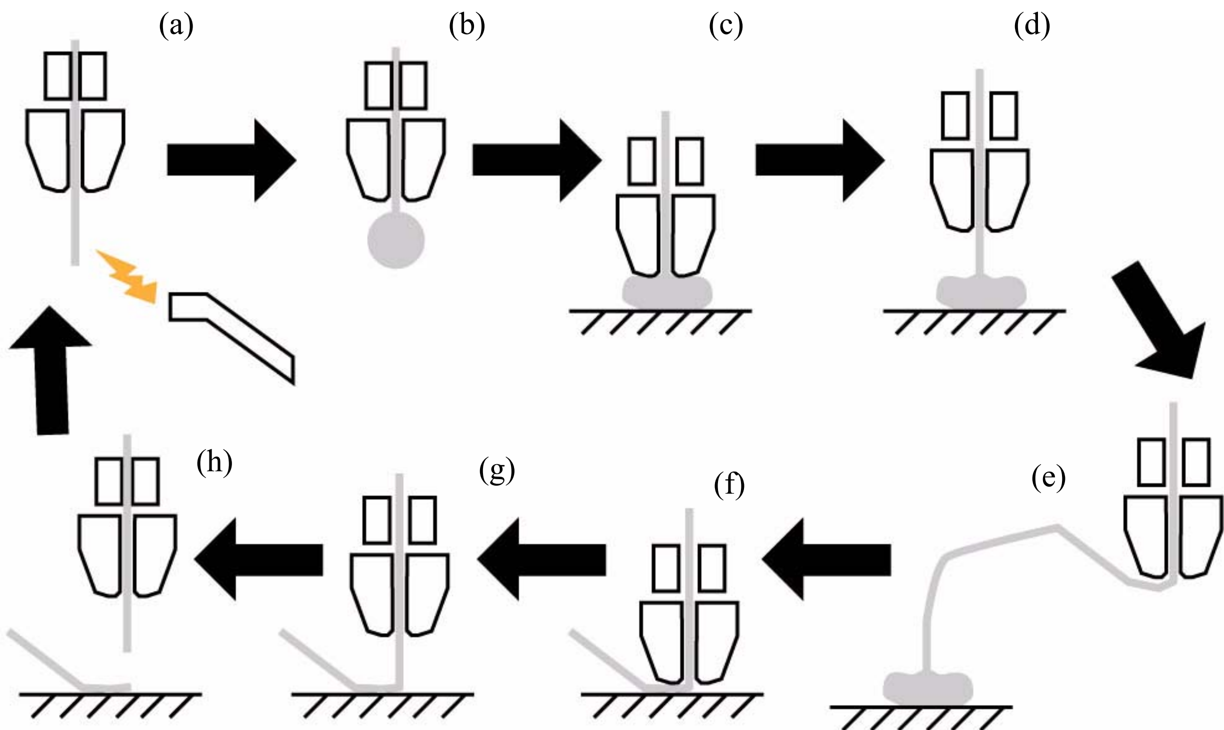

Fig. 3 Ball-wedge wire bonding process showing the cyclical procedure from steps (a) where the FAB is created from the wire tip to (h) the breaking off of the wire from the tail bond.

Two types of tests used in the industry are High Temperature Storage (HTS) [9,10,11,12] and Highly Accelerated Stress Test (HAST) [12] which use heat and even humidity to accelerate the aging of a ball bond. Then, destructive tests such as shear or pull tests are used where the ball bond is mechanically removed and the forces required are used as a metric to compare the best process. Cross-sectioning of the joint is also done to determine which intermetallics have formed at the interface. An example of a cross-section is shown in Fig. 5.

Since HAST requires humidity control of the sample, it is more difficult to do and we are considering mainly HTS tests which only require heat. HTS is typically done at 150-175 ºC because this is the typical curing temperature for the protective molds [9] that cover a bonded microchip and bake times from 500-1000 h [13] for Au ball bonds.

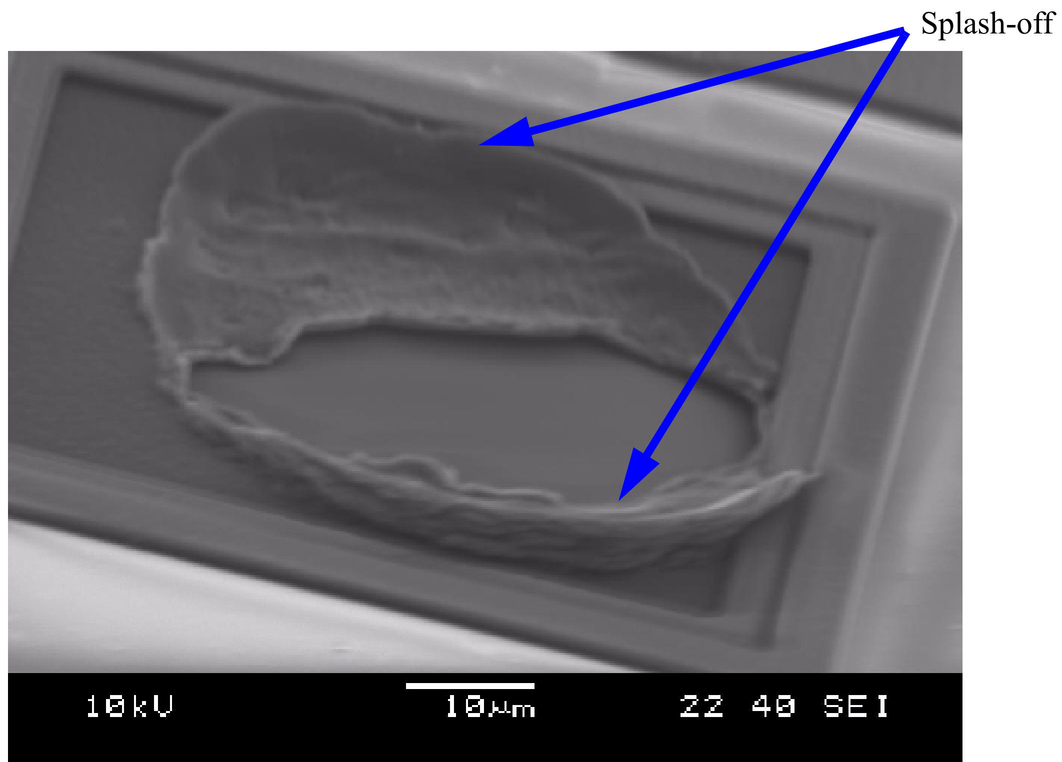

Fig. 4 SEM image of splash-off of a bonding pad. The ball bond was removed by being pulled off the bond pad.

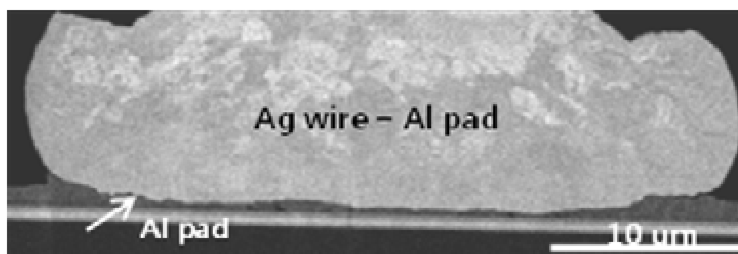

Fig. 5 Example of a cross-section of a ball bond joined to a bonding pad [4].

For copper ball bonds much higher temperatures are needed to induce IMC formation [9] with IMC formation between Cu and Al found to be a tenth of the speed that Au and Al IMCs form [14]. Large amounts of stress form at the periphery resulting in residual stresses which combined with IMC formation stresses cause voiding around the edge of the bond interface. However these processes require much higher temperatures to facilitate [9].

1.4 Literature Review on In-Situ Measurement

1.4.1 Contact Resistance

The contact resistance of a ball bond is an important factor to consider due to the fact that a ball bond can electrically fail while still maintaining a high shear force breaking point [10]. Because contact resistance is typically in the single-digit mΩ range [10], the lead resistance is as large or larger than the measured value. To remove lead resistance from the measurement, the four-wire method is used where a low-level constant current is used to drive a voltage measurement. Voltage is sensed only when there is a potential drop caused by another voltage or a current flow, so if no current is flowing through the voltage sensing leads then the lead resistance is not included in the measurement. Using this principle the current used to measure the resistance is applied separately from the voltage sensing lines. For the contact resistance of a ball bond, the current flows from the upper ball bond through to the pad and out from a metal line connected to the pad as seen in Fig. 6. The voltage is measured from the lower ball bond and out from a different metal line connected to the pad. This arrangement reduces how much of the ball bond itself is measured.

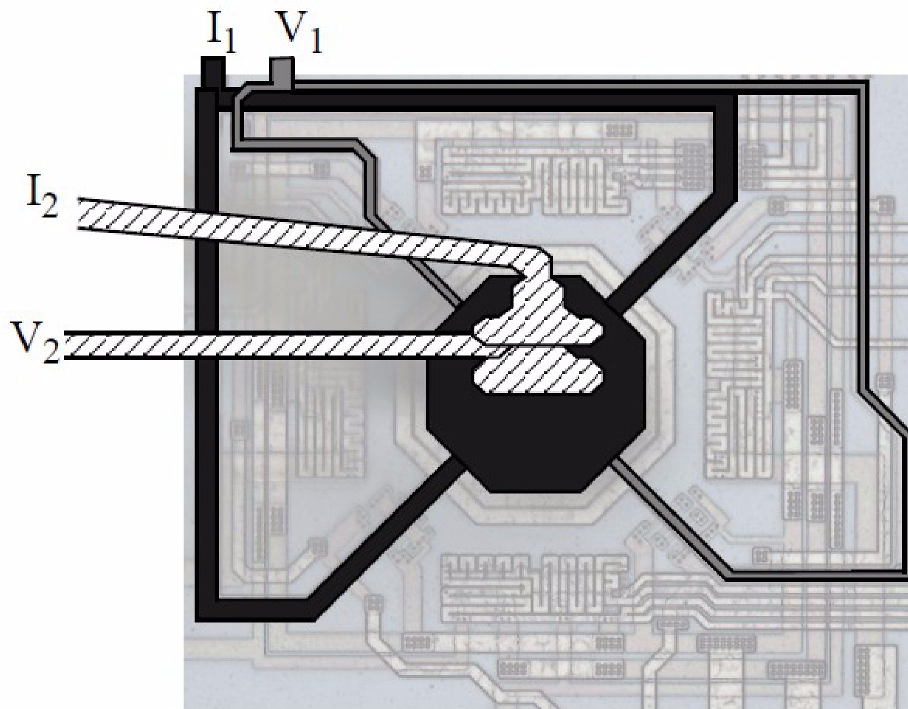

Fig. 6 Four-wire method for measuring contact resistance of a ball bond. [15]

Due to the width of the metal lines coming out of the bond pad, the current used to measure the contact resistance is limited to 1 mA for the chips that have been designed in this thesis. As a result the measured voltages are in the microvolt range so to achieve enough precision a nanovoltmeter is used to measure the voltage. Contact resistance increases for a variety of reasons such as Kirkendall voiding or IMCs having a different resistance than the base metals [10, 15, 16]. Electrical failure occurs when the voiding cuts off the connection between the wire bond and the microchip's lines connected to the pad.

Some disadvantages of using contact resistance is that they require a double ball bond [15,17] which needs different bonding parameters, and require the resistance changes to correspond to aging of the joint. Some advantages are that this method can determine the electrical integrity of the joint which can be different from the mechanical integrity.

1.4.2 Localized Stress Sensors

There are three types of stress sensors implemented on the designed chips in this thesis. Piezoelectric sensors have been shown to pick up ultrasonics from the bonding process as well as sense the effect of IMC formation on the surrounding Si matrix via volume changes [13]. These sensors work on the principle that stresses to Si change its resistance, and the sensitivity to certain directions of forces can be altered using different dopants (N or P) or different angles of doped Si lines [18].

These sensors are placed in a Wheatstone bridge to increase the sensitivity and remove the need for calibrating each sensor since only the differential signal is measured. The Wheatstone bridge method also removes any effects that change each sensor in tandem, such as uniform temperature changes. Some examples of piezoelectric sensors around the bonding pad are shown in Fig. 7, where (a) the z-force and (b) x-force sensors are schematically drawn. The differential signal is calculated as:

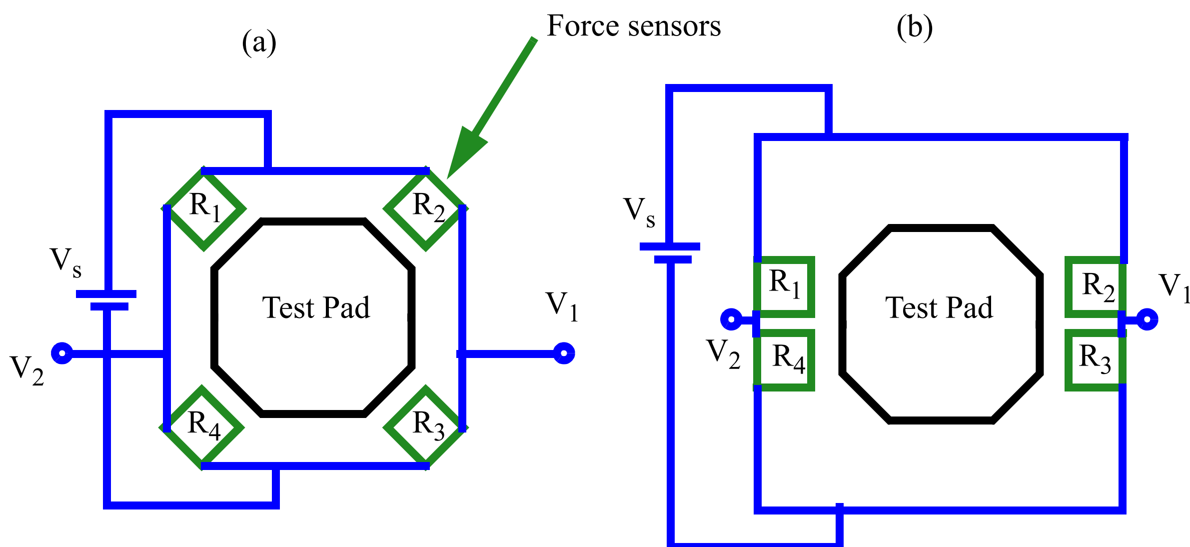

Fig. 7 (a) Z-force and (b) x-force sensors in Wheatstone bridge configuration. Voltages and resistance labeled to correspond with Eq 1 and 2.

$$S = (V_2 - V_1)/V_S \quad \textbf{[Eq. 1]}$$

Which corresponds to the resistance of the sensors:

$$S = \frac{R_1 \cdot R_4 - R_2 \cdot R_3}{(R_1 + R_3) \cdot (R_2 + R_4)} \quad \textbf{[Eq. 2]}$$

When a sensor undergoes stress, its resistance changes so by arranging them in the Wheatstone bridge correctly, specific directions of forces are amplified by the bridge. For instance, for forces in the x-direction for P+ doped sensors, R_1 and R_4 decrease if the force is unidirectional in their direction while R_2 and R_3 increase, causing the total signal change to be $\Delta R/R$, where ΔR is the change in resistance and assuming all base resistances for the sensors are the same.

1.5 Literature Review on Microheater Design

Microheaters are micrometer scale heaters which use voltage or current applied across a resistive device to generate heat. The device is usually a metal resistor or doped Si on the surface of the microchip [19,20,21,22]. This means that a microheater can be designed using standard complimentary metal-oxide semiconductor (CMOS) technologies without the need for special materials or any physical modification of the bulk Si such as etching. The microheater can be thermally isolated by removing the bulk Si beneath the microheater [18]. However, for applications where cooling of the microheater is needed (e.g. cycling of temperature), keeping it attached to a substrate or the bulk Si helps dissipate heat. The temperature vs. power, and resistance vs. temperature plots were largely linear [19], which corresponded to the results found with the microheaters designed for this thesis. Electrical isolation of a doped-Si microheater is possible by creating a diode junction between the conducting doped-Si and the surrounding substrate Si.

1.6 Literature Review on Digital IC Design

Digital integrated circuits (ICs) are essential to scale electrical circuits from the external macro-level to internal micro-level. For instance, instead of externally switching between each test pad on the microchip, a designer can reduce the number of pads as well as remove the need for an expensive multiplexer through the use of integrated circuits. There are several metrics for measuring the performance of a digital design, such as the number of metal layers, minimum transistor width, fan-in/fan-out, voltage characteristics, and thermal properties [18]. All of these affect the speed and reliability of the design during reliability testing as transistor behavior and metal capacity both depend on these parameters.

The most basic element in an IC is the diode, formed by the interface between p-type doped Si and n-type doped Si. Due to the carrier concentration differences between the n-type and p-type Si an energy barrier is created preventing current flow from the n-type to p-type regions but allowing it in the other direction. This means that a diode only conducts in one direction for all practical intents and purposes [11].

If two diodes are placed facing each other, a transistor is created by connected the middle section to a capacitor formed with silicon oxides as the dielectric and then a polysilicon conductor. As seen in Fig. 8, applying a specific voltage to the gate terminal creates a channel connecting the two ends of the gate, called the source and the drain. This is the principal behind the metal oxide semiconductor field effect transistor (MOSFET) and when both n-type and p-type MOSFETs (NMOS and PMOS) are used, this is called a complimentary MOS (CMOS) circuit which allows

for logical operations to be made. Arrays of transistors are used to create circuits which then form gates such as NAND or NOR gates, and these then combine to form entire modules [18].

The most basic CMOS logical gate is the inverter, which takes a digital 1 or 0 and changes it to a 0 or 1, respectively. Another basic CMOS device is the (transmission gate) switch, which uses the ability of the gate terminal to control whether or not the source and drain are connected, an example schematic of three switches in a column is shown in Fig. 9. Using different combinations of NMOS and PMOS transistors allows the designer to create different logical operators.

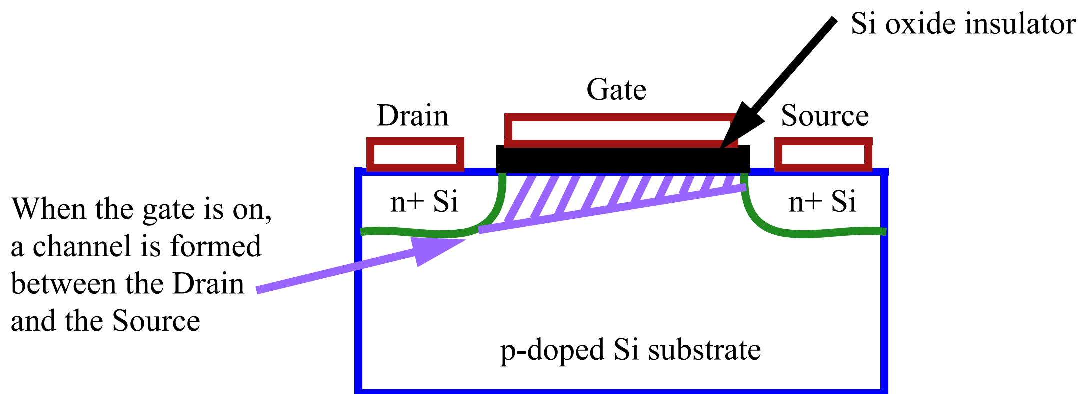

Fig. 8 Schematic of an n-p-n (NMOS) transistor.

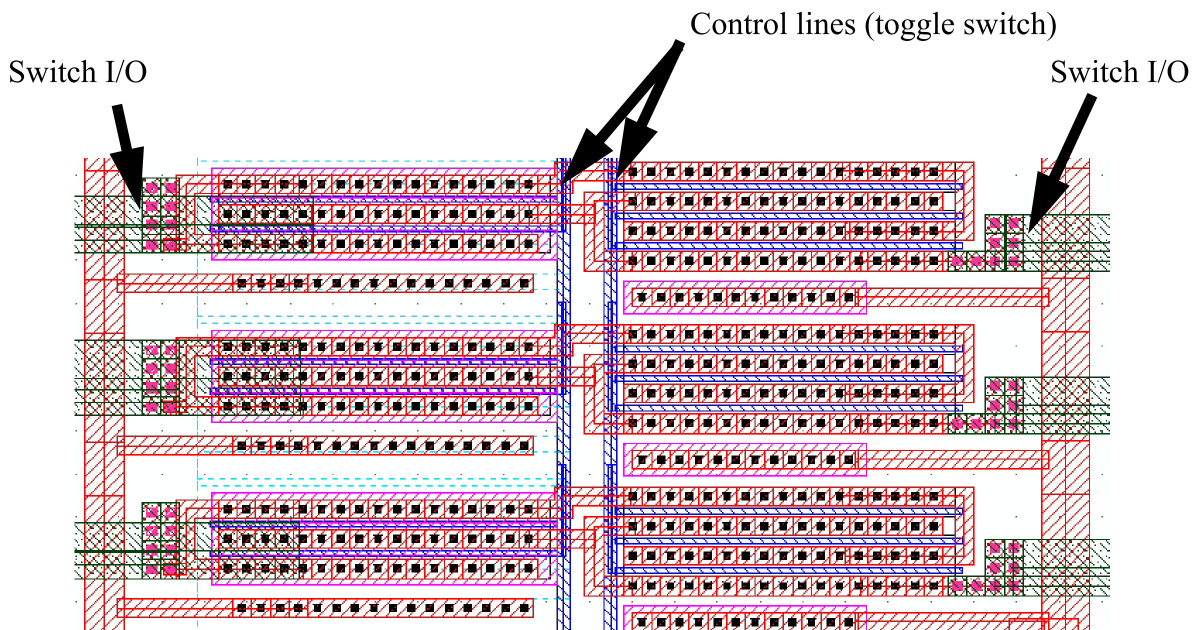

Fig. 9 Layout of three switches side-by-side, taken from a CAD screenshot. These switches are made from a PMOS and NMOS transmission gate connected together.

Digital ICs are designed using CAD programs such as Cadence® [23], which use the fabrication company's design kits to provide the designer the tools and information for the material layers and rules.

1.7 Motivation

Shear or pull tests do not verify the electrical integrity of the joint, however measuring the contact resistance of a ball bond requires a double ball bond to be made on the test pad, which is difficult. To facilitate monitoring of the electrical integrity of the test bond without the need for double ball bonds, a pad resistance measurement method is introduced in this thesis. Using the pad resistance of the test pad, both the IMC formation as well as the electrical integrity of the ball bond is measured. The pad resistance is measured in-situ using a specifically designed test pad in a typical CMOS microchip fabrication process.

Novel bonding wires being developed use thin coatings such as Pd [5] or new wire materials such as Ag or Cu [4,5], which form IMCs at much slower rates than Au with Al bonding pads. This requires higher temperatures than are used in aging tests currently so that IMCs can form in a reasonable time frame and bonding parameters can be compared. High temperatures make in-situ measurements difficult as not only do the sensing and power wire bonds age as well, digital signals and transistor operation start to fail. However, using a microheater underneath the test bond pad localizes the heat to the test bond and the power and sensing bonds do not age significantly as most of the heat dissipates into the bulk Si.

1.8 Objective

The objective of this research is to prove the feasibility of simultaneously integrating multiple types of in-situ sensing of ball bond reliability, digital integrated circuits, and heating components all onto the same chip. This would create a largely contained test-on-a-chip device which only needs the measurement and power equipment along with computer control to operate and allow for automated, parallelized reliability analysis of ball bonds non-destructively. The operation of the microheater at high temperatures is shown along with pad resistance measurements to show the increase of resistance as IMCs form. Several chip designs are made to facilitate multiple types of in-situ measurements.

1.9 Thesis Outline

Five microchip designs for wire bond reliability test are discussed in Chapter 2, all of which were designed at the University of Waterloo and fabricated off-site. Their various in-situ measurement capabilities along with their digital circuitry are explained. The experimental setup, characterization, and operation of the microheater on the Microheater and Underpad Sensor microchip is shown in Chapter 3, along with the associated pad resistance results. This includes the derivations of pad resistance, performance issues such as high temperature drift, and the software control of the temperature. Similar aging of novel wire bonds and gold wire bonds from the Parallel Microsensor chip are shown in Chapter 4 to show repeatability of IMC formation at the pad surface using either an oven or a microheater. The conclusion regarding the viability of these novel wire bond reliability methods is made in Chapter 5 along with the outlook on next steps. Bonding diagrams and listings of the software programs used to operate the experiments are contained in the Appendix.

2. Microchip Designs

In this section the five microchips designed for wire bond reliability testing are explained, with their analog and digital components listed and functionality detailed. The first microchip is the Parallel Microsensor Chip which makes uses of force sensors and contact resistance measurements for a total of 55 test bond pads, this chip was designed and fabricated in 2009. The second chip design discussed is the Parallel Microsensor Chip v2, which was an updated version of the Parallel Microsensor Chip where several improvements in the design were made, design and fabricated in 2012. The third microchip is the Thick-wire Microheater Chip which was designed to test Al ribbon bonds and was made in 2010. The fourth microchip is the Microheater and Underpad Sensor Chip which contains the microheater component as well as under-pad stress sensors, designed and fabricated in 2010. The fifth microchip is the Microheater and In-Situ Measurement chip, made in 2012. All chip designs were done using Cadence®. The functions for every chip discussed in this thesis, including their designation and where to find the corresponding bonding diagrams are below in Table 1.

Table 1: Microchips for wire bond reliability studies discussed in this thesis, their capabilities, and their bonding diagrams

Chip Structure#	Name	Capabilities	Bonding Diagram
1	Parallel Microsensor Chip (PM chip)	Force sensors, contact resistance	Appendix B
2	Parallel Microsensor Chip v2 (PM chip v2)	Force sensors, contact resistance	Appendix C
3	Thick-wire Microheater Chip	Microheater	Appendix D
4.1	Microheater and Under-pad Sensor Chip - Structure 1 (MUS chip)	Localized temperature sensors (for bonding power)	Appendix E - bonding diagram 1
4.2	Microheater and Under-pad Sensor Chip - Structure 2 (MUS chip)	Linear stress sensor	Appendix E - bonding diagram 2
4.3	Microheater and Under-pad Sensor Chip - Structure 3 (MUS chip)	Local stress sensor	Appendix E - bonding diagram 2
4.4	Microheater and Under-pad Sensor Chip - Structure 4 (MUS chip)	Microheater	Appendix E - bonding diagram 3
5	Microheater and In-Situ Measurement Chip (MISM chip)	Microheaters with stress sensors and pad resistance	Appendix F

2.1 Parallel Microsensor Chip

The Parallel Microsensor (PM) Chip was designed to be able to monitor the contact resistance and stresses of test bonds for up to 55 samples simultaneously. Layout was done using the Europractice 0.7 µm design kit. This microchip measured 4200 by 2500 µm and a photograph of a bonded chip is shown in Fig. 10. The bonding diagram for the PM chip is located in Appendix B.

Each sensor pad contains force sensors in the x, y, and z directions [15] as well as connections to allow four-wire method resistance measurements [15] of the ball bond to all be taken real-time while the chip is aging. On-chip temperature detection [24] is present to reduce additional equipment requirements while doing heated aging tests. Test structures are also available so that characterization of single sensors or digital components can be done and measurements of voltage drops throughout the microchip taken. Measuring 30 or more sensor pad readings simultaneously requires a large number of output pads, so a different approach to reading signals from the microchip is taken. A single shared bus is used by all sensor outputs, (one bus line for each output) and a digital controller is used to allow only the eight outputs from one sensor pad to be outputting to the bus at a time. An example of the process of using the digital controller to allow the desired outputs from a sensor pad to connect to the bus is shown in Fig. 11.

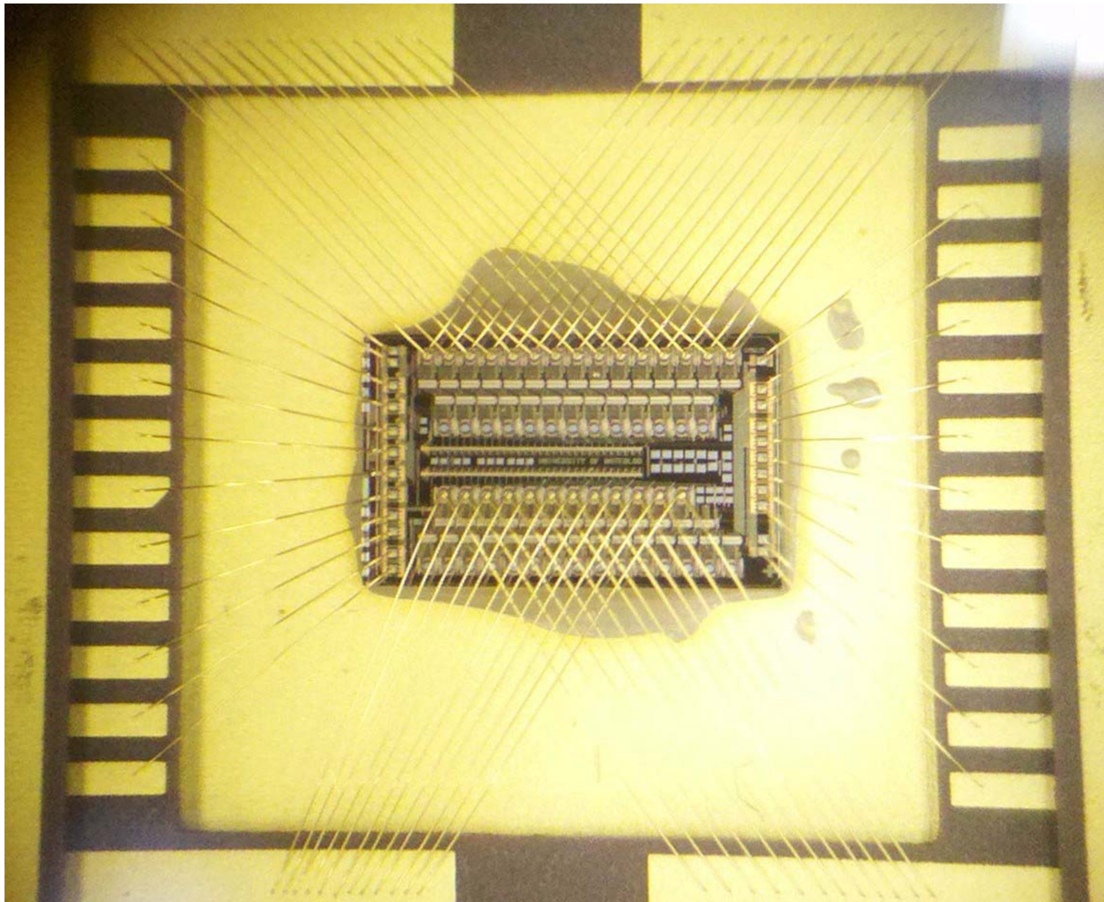

Fig. 10 Photograph of the PM chip with all I/O pads bonded and two rows of test bonding pads with double ball bonds for contact resistance measurements.

Buffering inverters are used to rectify the digital signals from the input pads to the digital controller and from the digital controller to the switches. The switches connect the test pads to the bus. The digital controller is made using a multiplexer which in turn is composed of multiple stacked NAND gates. The CAD layout of the entire microchip is shown in Fig. 12.

2.1.1 Buffering Inverters

Buffering is a method of rectifying digital signals that were sent across different parts of the chip, it results in reduced: capacitive loading, resistance seen by the buffered circuits, and voltage degradation between sub-circuits. Buffered inverters are two inverters placed in series -- this is useful because it also allows the following digital circuit to make use of both the input signal and its inversion while providing a buffered signal efficiently.

2.1.2 Switches

Switches are used to gate sensors from the data bus selectively. They are controlled by a single bit. The switches used in the microchip are implemented with transmission gates, which are regular transistors except the source and drain are used as the signal input and output.

2.1.3 NAND Gate

NAND gates are a type of logic gate which are the logical equivalent of an AND gate with an inverter (NOT gate) at its output, hence the N- prefix. Using a combination of NAND and inverter gates, larger NAND gates can be constructed of arbitrary input capacity (only constrained by the user's signal rise/fall time and capacitive requirements). To explicitly indicate the number of inputs a NAND gate has, the number of inputs is appended directly to "NAND", i.e. NAND5 gate would be a NAND gate with five inputs.

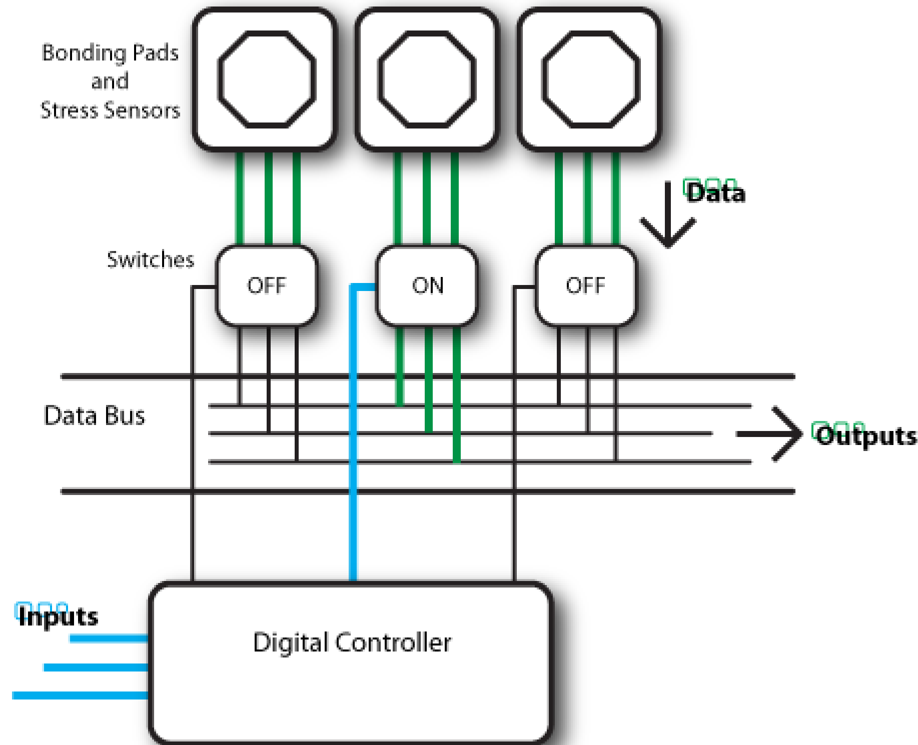

Fig. 11 Schematic of PM chip's multiplexer digital controller being used to control which bonding pad and stress sensor set is connected to the microchip's data bus.

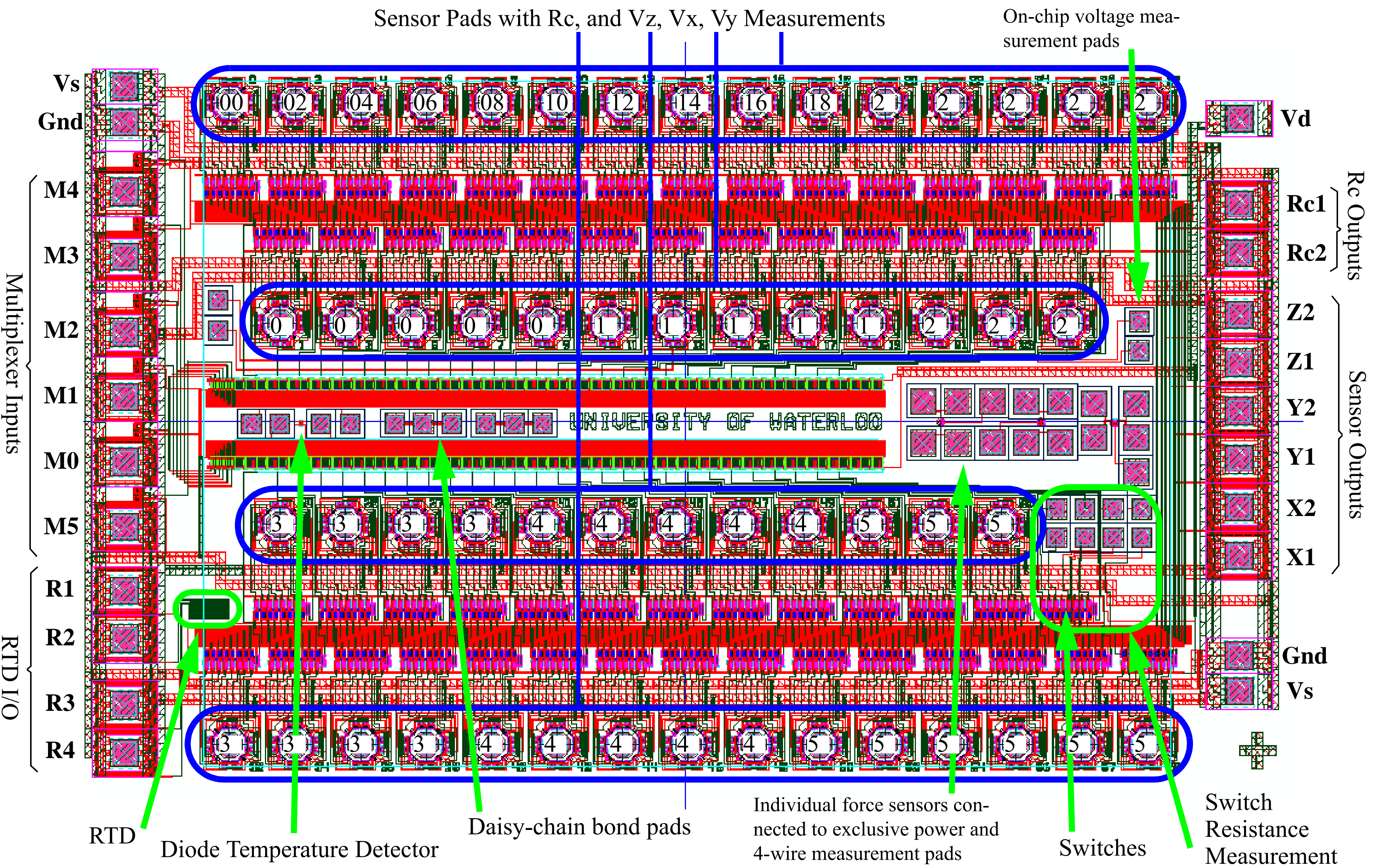

Fig. 12 Layout of the PM chip showing the location of the various components, the test pad numbering, and the I/O pads.

The NAND9 gates were required by the design due to the large number of inputs and outputs. They are constructed from two staggered NAND5s: the first stage NAND's output is fed into an inverter (effectively making it an AND gate) and connected to the input of the second stage NAND as shown in Fig. 13.

2.1.4 Multiplexer

Multiplexers are also known as decoders [25] due to their ability of transforming an input into a different combination of bits. Using N digital inputs to select one out of 2^N possible outputs to be "on", while the rest are "off". A visual example of a decoder with 3 inputs (3-bit decoder) is shown in Fig. 14, where a binary 011 (3) is inputted to set only the fourth output to be zero ("on"), while the rest remain 1 ("off"). For the microchip, six inputs are used to signal which of the sensor

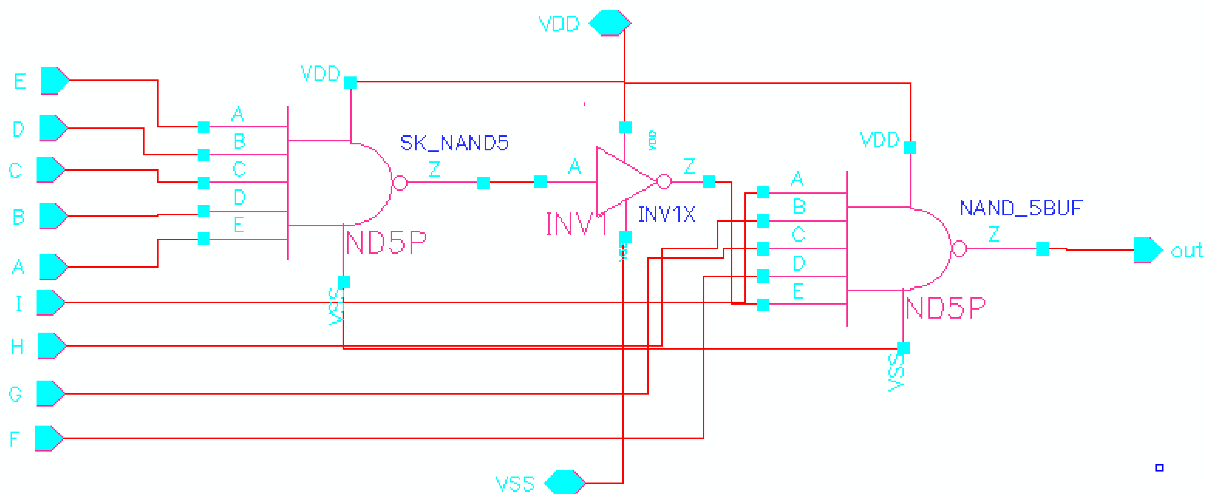

Fig. 13 PM chip's nine-input NAND gate made from two staggered five-input NAND gates.

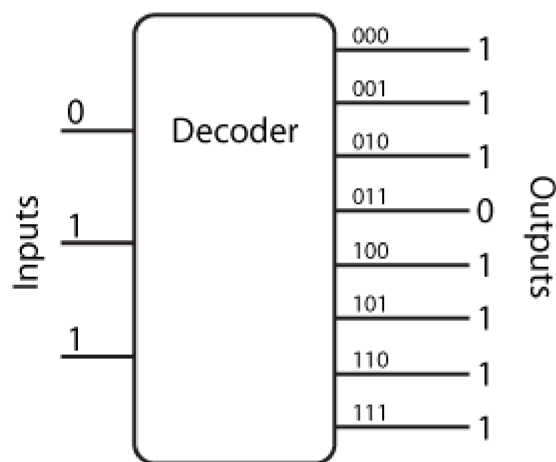

Fig. 14 Example of a 3-bit decoder where it selects one of the 2^N outputs to be "on" (0 state) depending on the input. In this case "3" is the input so the 4th output is on.

pads is outputting to the bus. Each sensor pad has a unique bit address and a series of switches that connect the sensor pad outputs to the data bus. As seen in Fig. 11, the “Digital Controller” is the decoder controlling the switches between the bus and the test pads. To see signals from Pad number 5, the binary 000101 is sent to the inputs of the decoder. The decoder closes the switch for pad number 5 and opens the switches for every other pad. As a result, the microchip’s outputs are then connected to the sensors on pad number 5 via the chip bus.

The decoder is implemented as a row of NAND gates and buffered inverter inputs as seen in the CAD view of the actual device layout in Fig. 15. The logical circuit implementation of the decoder is shown in Fig. 16; the six buffered inverters (triangular shapes) are along the top of the figure, and two of the 32 NAND gates (rectangular shapes) are on the side.

2.1.5 Due to the length of the design, there was a limitation in the number of NAND gates that could be placed in a decoder, and thus limited the number of sensor pad addresses that a single decoder could handle. While a 6-bit decoder can support up to 64 outputs, it is possible to split the decoder into two distinct halves each with only 32 outputs, reducing the length by almost 50%. By changing the NAND gate connections inside one of the decoder halves, they can have outputs assigned to addresses 0-31 and 32-63 respectively while using the same inputs, as shown in Fig. 17.

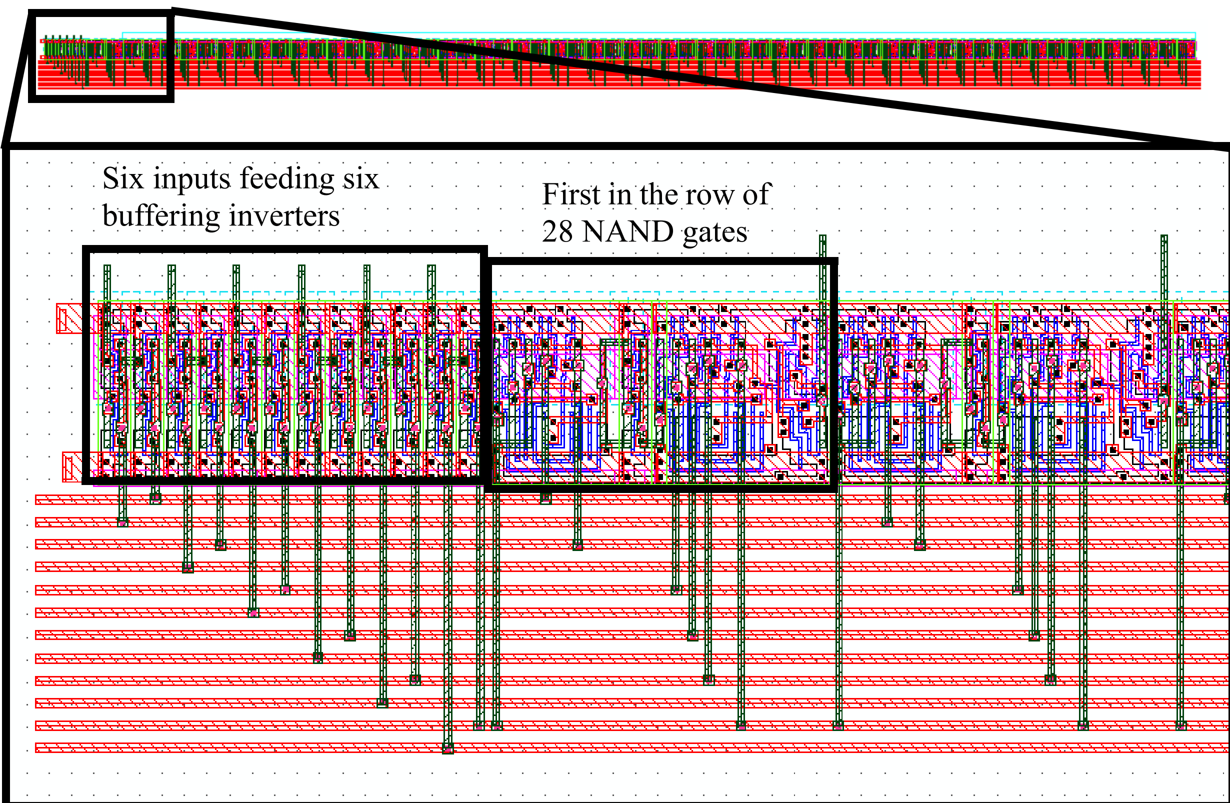

Fig. 15 Partial view of the PM chip’s multiplexer layout. Shows the six inputs to the left and two of the NAND gates on the right half.

2.1.6 Sensor Design

Force sensors have been used previously to correlate ball bond aging with changes in the stresses to the bulk Si around the joint [15], and in this microchip have been implemented around all 55 of the test bonding pads. Two types of sensors are used to measure the various forces applied locally to the bond pad. Z-force sensors measure the force normal to the surface of the chip while the lat-

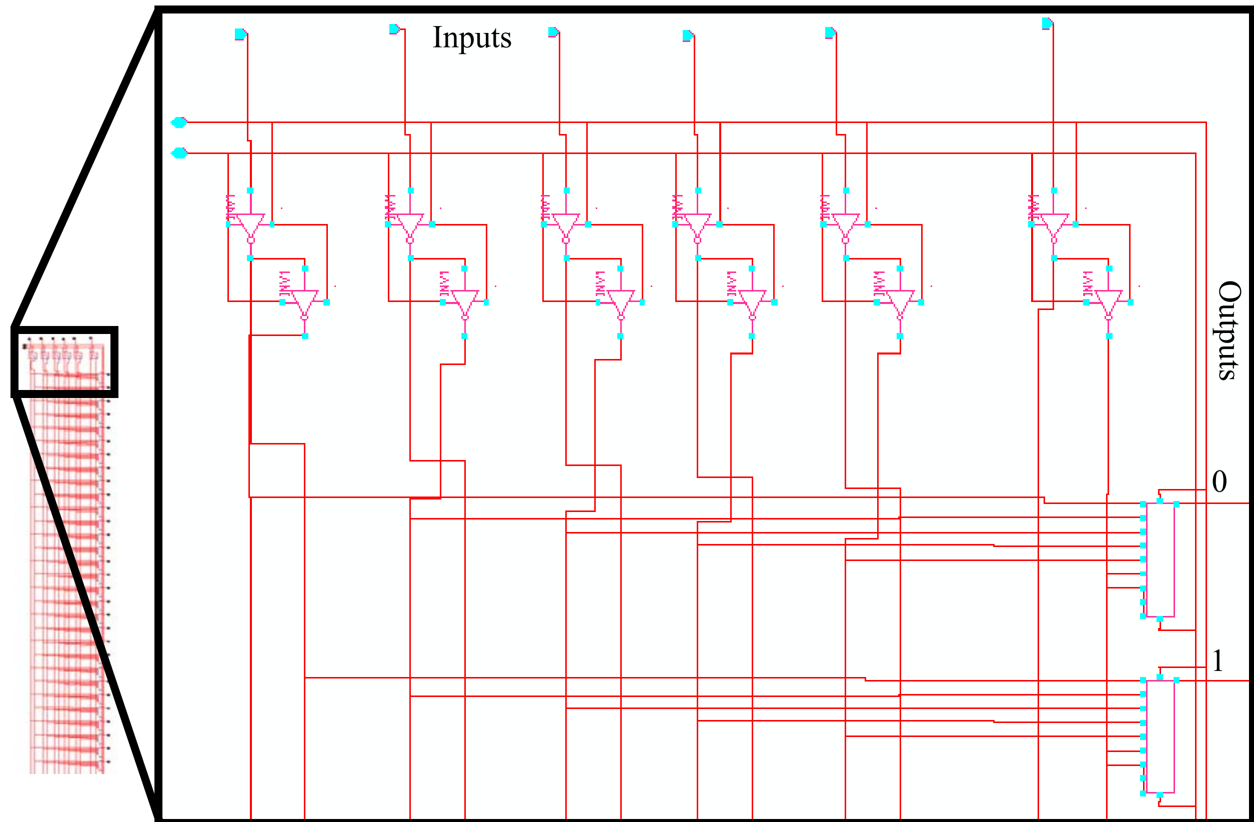

Fig. 16 Schematic of the decoder used on the PM microchip.

a) A single NAND gate is 75 µm long

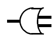

b) A decoder with 56 NAND gates is 4200 µm long, requiring a prohibitive chip size

c) A decoder with 28 NAND gates is 2100 µm long and two of them in tandem can control 56 sets of switches and not require a very long microchip design

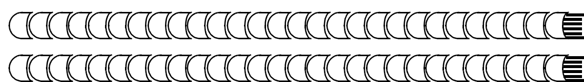

Fig. 17 Diagram showing a) the schematic of a NAND gate, and why instead of a b) single 56 NAND gate multiplexer, the decoder was split into c) two 28-NAND gate multiplexers.

eral force sensors measure the force along one direction parallel to the surface of the chip. The lateral force sensors are oriented at 90 degrees to give both x and y-force measurements, as seen in Fig. 18. The x, y, and z-sensors are located 10 µm from the test pad and come in groups of 4 to provide a Wheatstone bridge electrical connection. A Wheatstone bridge places four resistive components in a square, powered from two opposite corners, and the voltage is then measured from the two remaining corners. This configuration is used with these sensors to eliminate temperature variations and silicon impurity differences across the chip. The voltage across this Wheatstone bridge is relative to the stress experienced by the sensor.

Both sensors operate in the same fashion, the doped substrate undergoes stress (shear, tensile, etc.) and the resistivity changes is measured by the voltage drop across the Wheatstone bridge. Thus the differential voltage increases as the stress increases.

2.1.7 Wiring Design

Wiring widths are completely determined by the maximum current expected to be running through them, making them the primary design constraints for the power lines, followed by surface packing (make the lines as wide as possible in the space available).

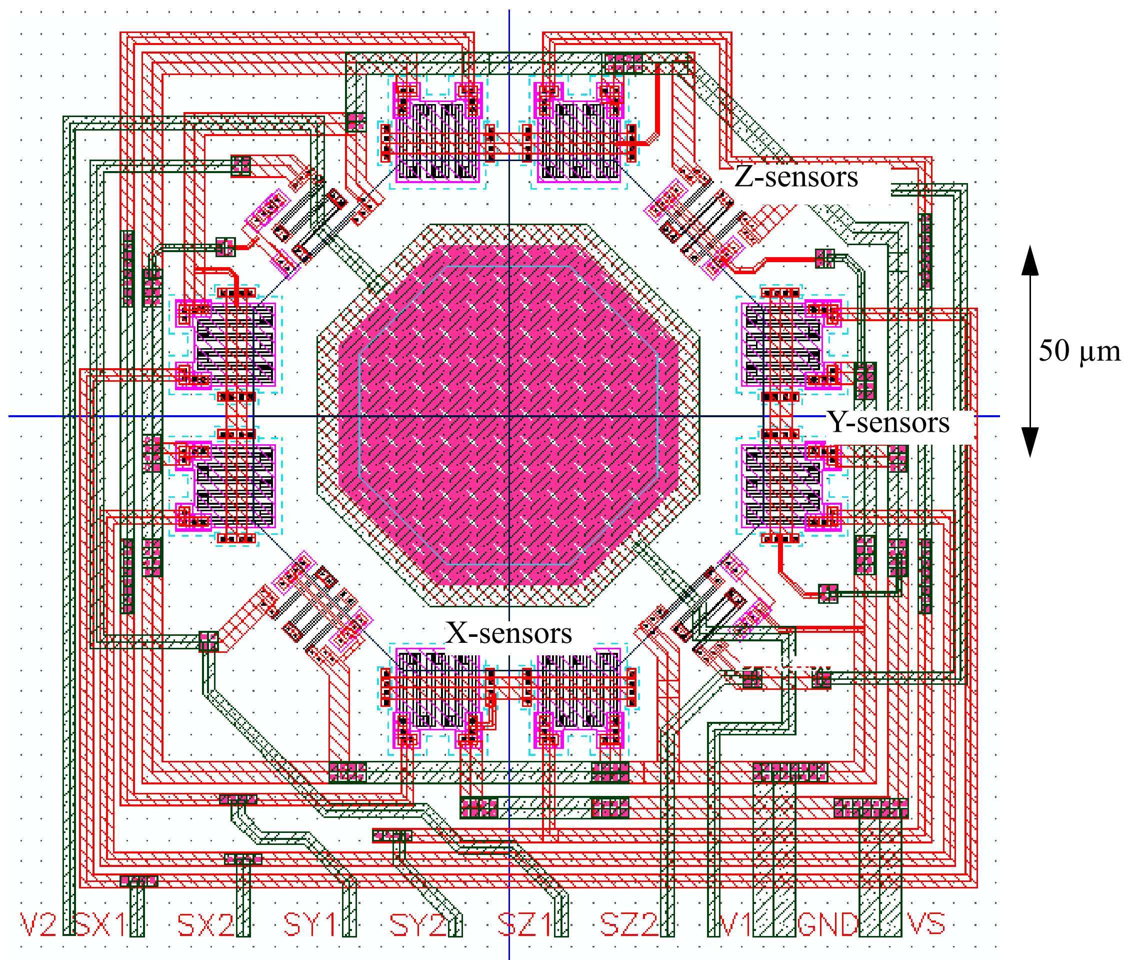

Fig. 18 Layout showing the X, Y, and Z sensors surrounding the octogonal test pad used in the PM chip.

Each sensor pad contains 4 z-sensors, 4 x-sensors, and 4 y-sensors for a total resistance of 1.46 kΩ, so at a supply voltage of 5 V, each sensor pad draws 3.4 mA. Therefore the outer rows of sensors draw a total of 188 mA. To prevent the supply lines from becoming excessively wide, current is fed in from both sides of the line, and a separate line is used for each row of sensor pads. Assuming equivalent flow from both sides, there is a maximum current of 25.5 mA @ 145 °C [3]. To provide sufficient margin of error and to account for usage at even higher temperatures, the power lines are 35μm wide. Higher temperatures can be achieved safely by lowering the supply voltage as this also reduces the current. The digital circuitry is powered by a separate voltage supply so that the voltage levels for the sensors and digital components can be changed without affecting each other.

2.1.8 Temperature Sensors

Two temperature sensors have been included on the chip. The primary sensor is a Resistance Temperature Detector (RTD), which uses changes in the resistance of a long aluminum wire to determine temperature changes. A Diode Temperature Detector (DTD) has been placed on the chip as well, which works in a similar principle. Temperature variations alter the free carrier concentrations throughout the junction and change the forward-mode voltage drop.

2.2 Parallel Microsensor Chip V2 (PM Chip V2)

The PM Chip V2 is a redesign of the previous PM Chip in the same Europractice 0.7 μm design kit and is 4200 by 2500 μm in size. The microchip was modified in seven different ways including new switches, connection lines, and numbering. Two new test structures were also added. All the changes and test structures are summarized in Table 2. The CAD layout of the entire chip is shown in Fig. 19 and the bonding diagram is contained in Appendix C.

2.3 Thick-wire Microheater Chip

A microheater design which heated a large Al pad, 1400 by 700 μm in size, the schematic is shown in Fig. 23. Layout was done using the CMC 0.5 μm design kit. This pad was made to support both ball bonds and Al ribbon bonds.

Due to the large size of the heater, estimation of actual heater temperature and consistency of heating needed more characterization. Contact resistance measurements could still be taken using this microchip. The bonding diagram for the thick-wire microheater chip is located in Appendix D.

2.4 Microheater and Underpad Sensor (MUS) Chip

This microchip was designed to implement underpad stress sensors, localized thermal power sensors during bonding, and a microheater. It measured 3400 by 3000 μm and a photograph of a bonded sample is shown in Fig. 44 in Section 3.4. The bonding diagram for the MUS chip is located in Appendix E.

Layout was done using the Europractice CMOS 0.7μm design kit. A total of six independent test structures were designed with new digital circuitry, shown in Table 3.

2.4.1 Structure 1: xyz-force + local RTD sensor

Ultrasonic vibrations during the bonding process generate thermal energy, which can be correlated to friction power. As the heating is highly localized, heat dissipation is rapid and the temperature profile follows ultrasonic movement closely. Aluminum (RTDs) are used to measure real-

Table 2: List of changes to the PM chip v2

Change #	Change name	Explanation
1	New power switches	New power switches were introduced between the force sensors and the power rails to reduce the current draw of the microchip, shown in Fig. 20. This reduces the microchips power draw and subsequent self-heating by having the current from the power rails only flowing through the active sensor. The ne power switches allow approximately 20mA of current at 150 ºC.
2	Design change: Reduction in number of test pads	The introduction of power switches increased the width of the microsensor unit, so less test pads could be fit on the microchip. Currently 50 test pads are on the microchip (5 less than before), in rows of 13, 12, 12, and 13 test pads from the top.
3	Design change: On-chip RTD removed	The on-chip RTD was removed as the ovens containing the PM chips contain its own temperature sensor which is more conveniently accessed.
4	Design change: Daisy chains for test bonds	All along the top and bottom rows, daisy chain bonding pads are placed so that the user can create test bonds to determine optimal parameters before committing to actual bonding of the test bonds. These test bonds can be removed afterward safely.
5	Design change: Alignment Markers	Alignment markers have been placed in every corner of the test chip.
6	Design change: Test pad numbering	The test pads are now numbered by row, starting from 0. Their number now exactly corresponds to the input address to the MUX.
7	Design change: Auxiliary I/O bond pads	Auxiliary bond pads for the Vdd, Gnd pads in both corners of the chip were placed in case alternative bonding recipes were needed. Vd (digital power) also has an auxiliary pad in the upper right corner. All these auxiliary pads are shown in Fig. 19.
8	Design change: Line thickness increased	The line thicknesses of all signal and sensing lines were increased where space permitted to reduce lead resistances and to increase current capacity at high temperatures.
9	Test structure: Voltage test	These bonding pads allow the user to check the voltage going to test pad #36, shown in Fig. 21.
10	Test structure: Sensor test with microheater	This test structure uses a microheater to heat a very localized part of the chip close to test pad #24, shown in Fig. 22. This heat changes the differential voltage signal across the microsensors allowing for operation and signal verification.

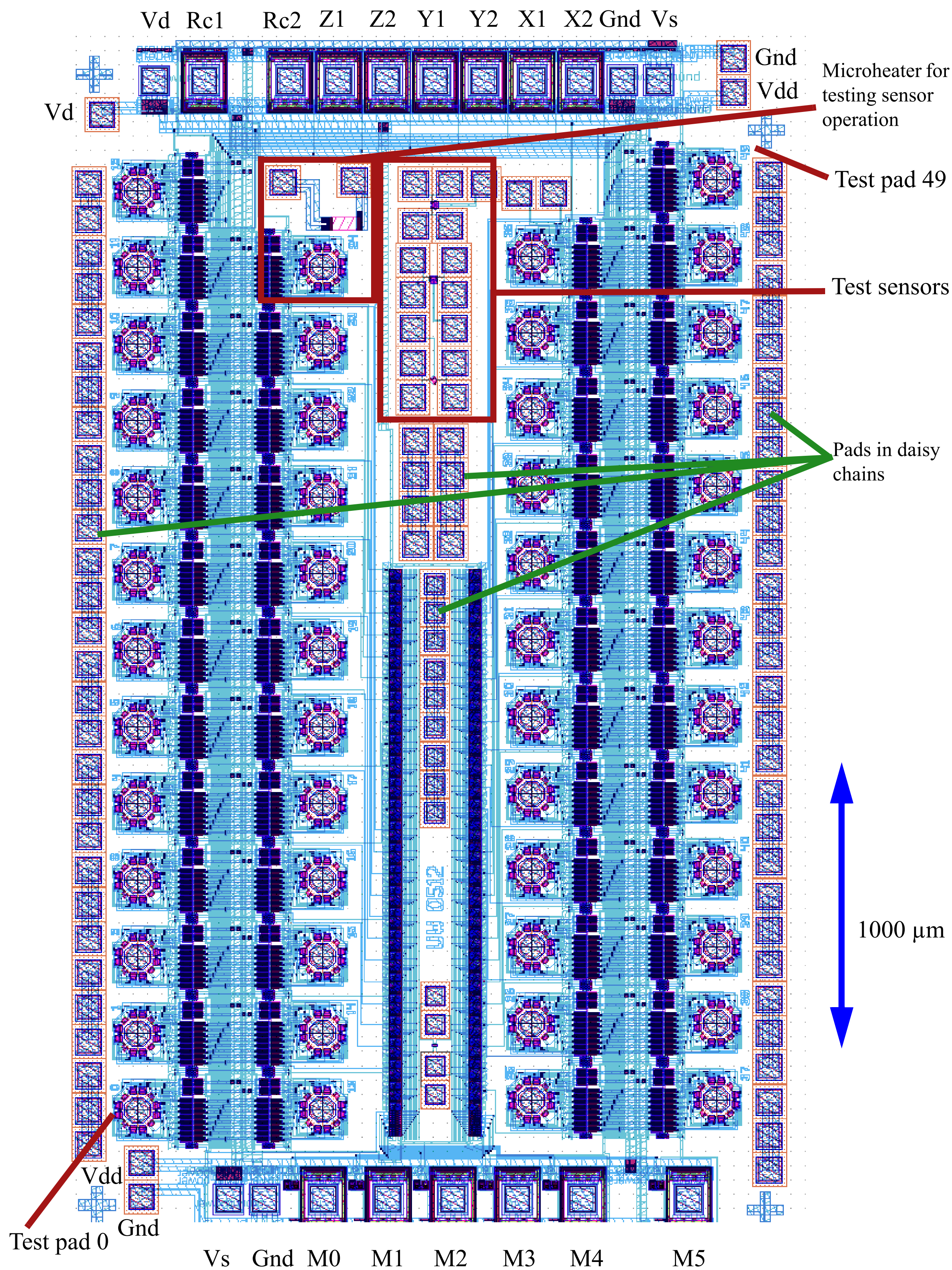

Fig. 19 Layout of PM chip v2 rotated 90º counterclockwise. I/O pads including Gnd, Vdd, and Vd (digital power) shown. Test pads start numbering at 0 and progress along the rows until 49.

time temperature changes during the bonding process local to the bond pad. As shown in Fig. 24 there are four RTDs comprised of concentric semi-circles, arranged into a Wheatstone bridge to most efficiently measure minute changes in resistance.

Twenty two of these test structures were implemented, one of which had the bonding pad removed and is coated with insulative protection. Thus, repeated tests can be done on this pad which simplifies confirmation of sensor signals and the multiplexer's operation.

Due to the large number of sensors and test pads, all sensor outputs are connected to a data bus instead of having their own individual I/O pads, which take up more space than the digital logic and bus lines. Using a multiplexer, the user can control which set of sensors for a specific pad are

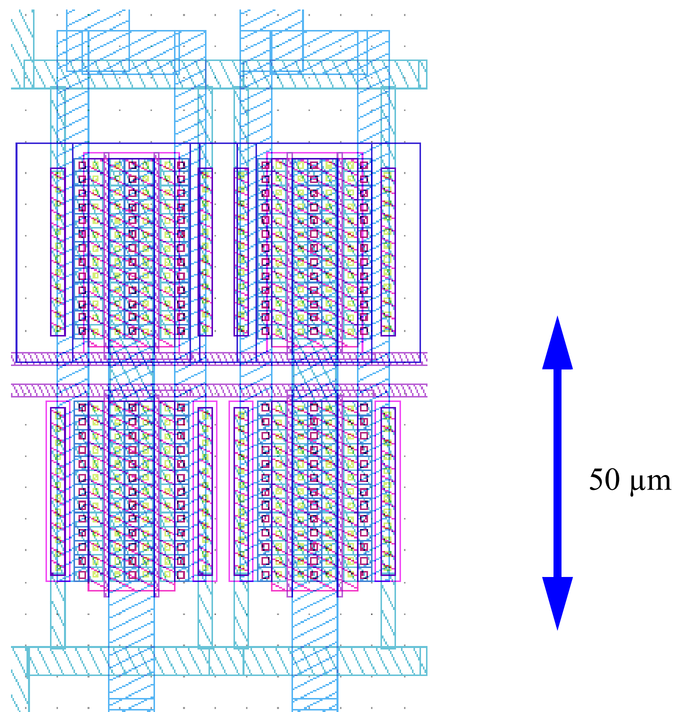

Fig. 20 Two power switches side-by-side on the PM chip v2, gating the microsensors from the power and GND rails. The number of vias and thickness of wires has been increased from the regular switches shown in Fig. 9.

Table 3: Structures on the MUS chip

Structure	Explanation
1	A total of 21 standard xyz-force sensing test pads with a local RTD connected to a multiplexer. The outputs are connected to a data bus.
2	Four localized stress sensing structure underneath octagonal test pads.
3	Nine oversized test pads with a single signal stress sensor underneath.
4	One test pad with an underpad heater.
5	Flip-flop chain for underpad stress sensor channels.
6	High current switches.

using the data bus at any time. Also, to minimize power usage, each set of sensors for a test pad are gated from the power supply and ground rails.

The octagonal test pads are 50μm in diameter. The average distance of the RTD metal lines to the center of the bondpad is 55 μm. The total resistance of each RTD section is approximately 56Ω. The vertical interconnects between each Wheatstone bridge are approximately 4Ω each, reducing the resistive sensitivity by 7%. This extraneous resistance is considered to be insignificant as there are already deviations caused by varying line thickness and the datasheet specifications [26] state that a maximal variation of 25% is possible.

The test pad has the RTDs connected as opposing pairs as seen in the upper left of Fig. 24. Since the Wheatstone bridge is mirrored to a second bond pad, heat characterization tests can be made a second time, but without simultaneous force measurements. To use the Wheatstone bridge, a constant current controls the amount of current flowing through the thin metal lines to prevent the metal lines from burning out. Each terminal of the Wheatstone bridge has an output connection so that the voltage from any two points can be measured. The voltage along the current flow is measured once at the beginning of the experiment. The differential voltage, across V+ and V-, is measured subsequently during the bonding test to derive temperature changes. The stress sensors can be powered anywhere from 3.5-5V while the digital logic is recommended to be powered at 4-5V. The multiplexer is controlled via five digital input pads labeled M0 to M4. These multiplexer

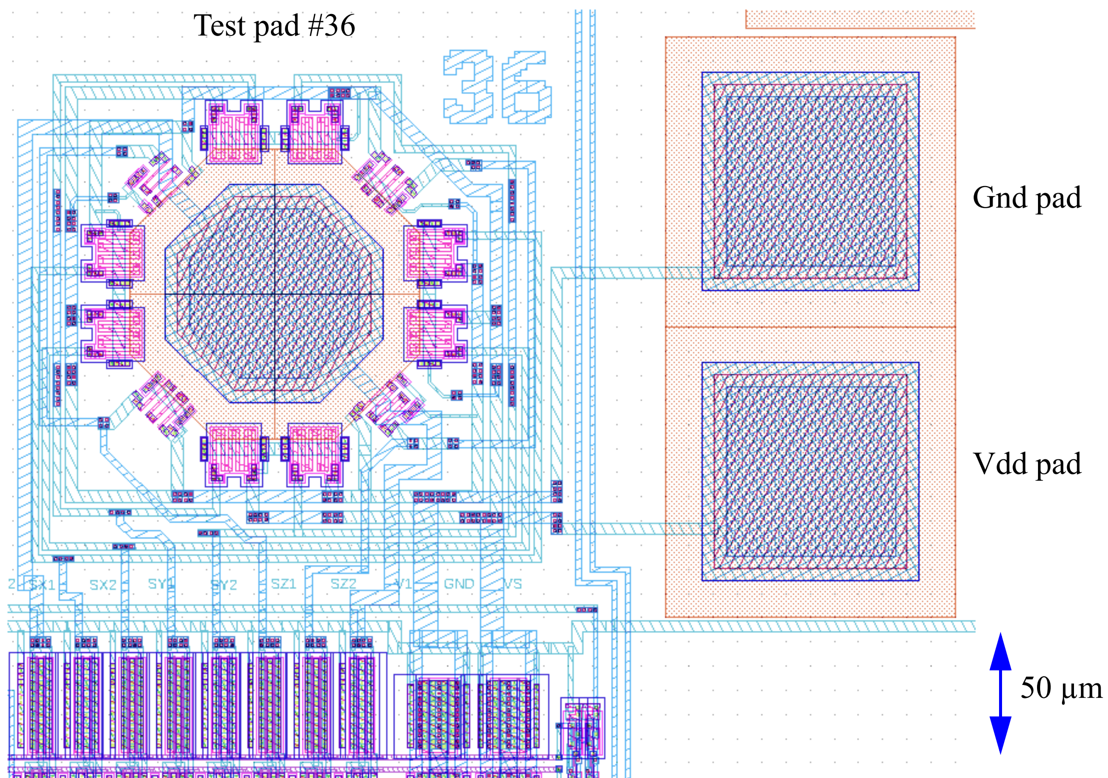

Fig. 21 Bonding pads on PM chip v2 which are connected to the microsensor Vdd and Gnd after they go through the power switches.

inputs represent the binary address the user wants to activate, where M0 is the least significant digit and M4 is the most significant digit. Examples of pad addressing is shown in Table 4.

The location of the test structures, multiplexer inputs, and data outputs on the chip are all shown in Fig. 25.

2.4.2 Structure 2: Linear Stress Sensor

This structure measures bonding forces in real-time, local to the bonding pad during the wire bonding process. To maximize z-force response along the axis of ultrasonic motion, a 0 degrees

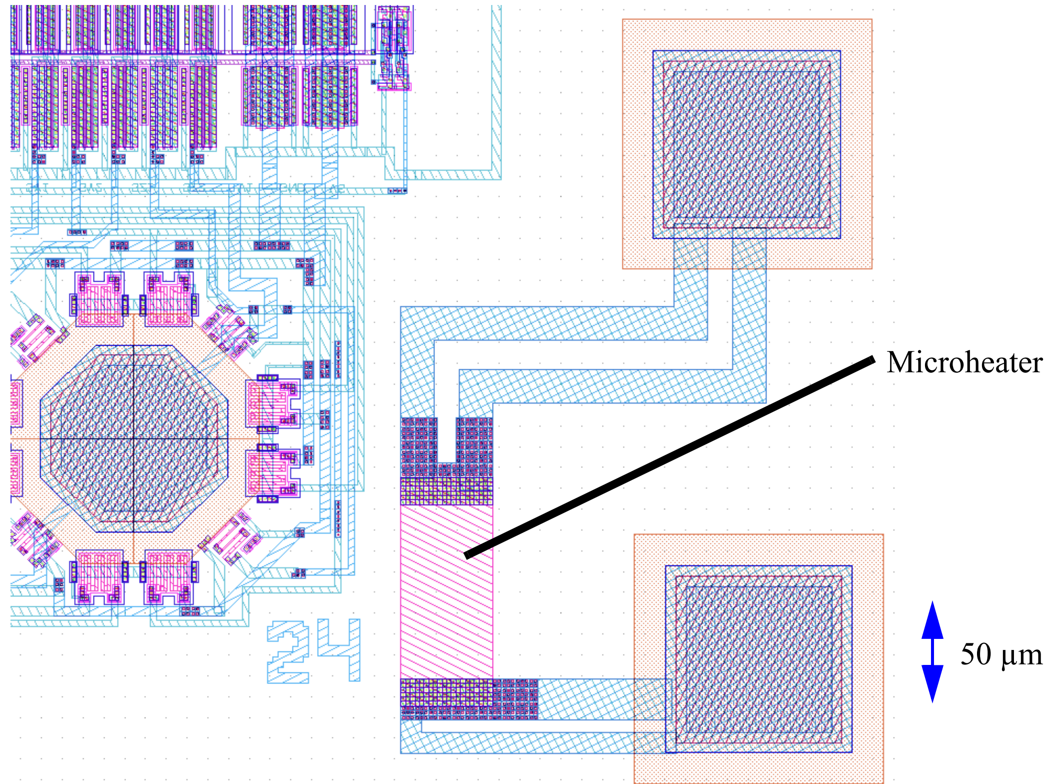

Fig. 22 Microheater test structure on PM chip v2 to test pad #24's stress sensor operation by increasing the temperature on one side of the sensors in Wheatstone bridge configuration, generating a differential signal.

Table 4: Examples of digital multiplexer input values for te PM chip

Pad #	M4	M3	M2	M1	M0
0	0	0	0	0	0
1	0	0	0	0	1
10	0	1	0	1	0
20	1		1	0	0
21	1	0	1	0	1

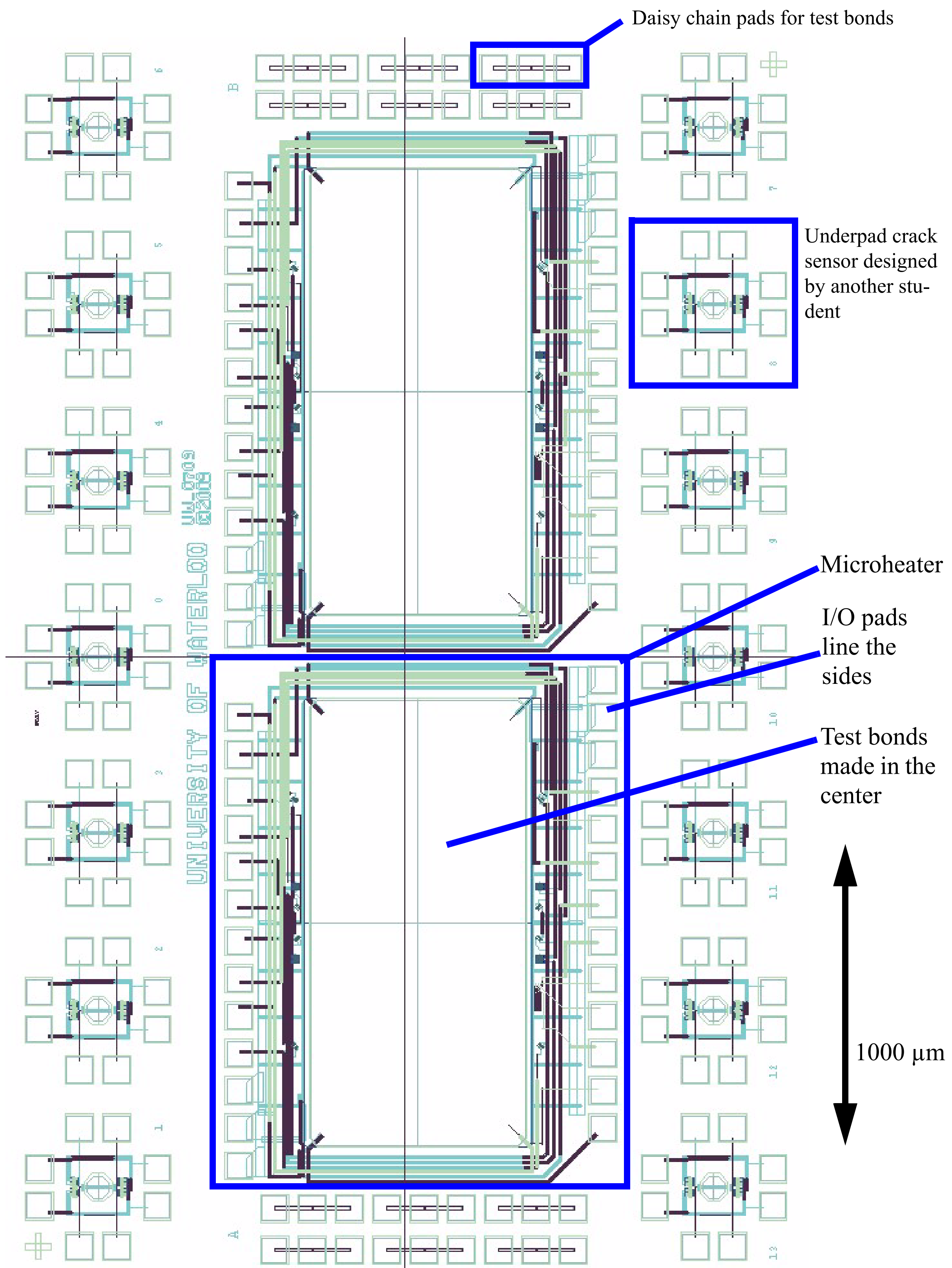

Fig. 23 Schematic of a previous microheater design, the thick-wire microheater chip.

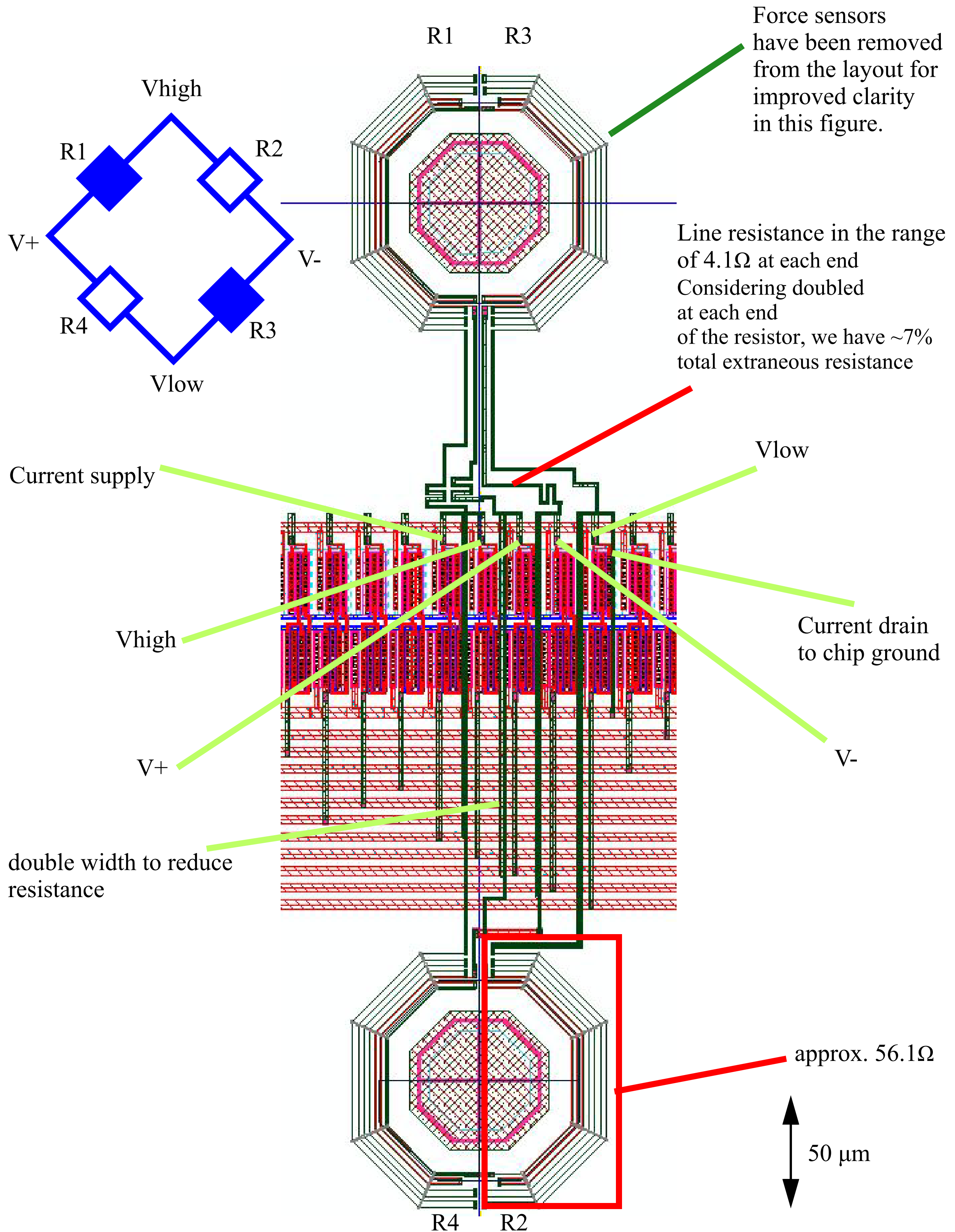

Fig. 24 MUS chip's structure 1: localized RTDs in a Wheatstone bridge and placement of sensing connections. Associated force sensors removed from schematic view for clarity.

orientation, N+ doped line (relative to silicon substrate plane) was calculated to be most efficient. The line is separated into segments with pitch of 4μm, with each segment being a separate channel which can be measured in parallel, seen in Fig. 26. This N+ doping in the 0 degrees planar-direction causes the line to be sensitive primarily to z-force stresses with some x-force components as well. There are a total of 19 channels represented by 20 output bonding pads. Extraneous signals from x-forces can be minimized by controlling ultrasound direction relative to the sensor line to reduce unwanted force components. The square resistance of N+ active area is 67.5Ω/sqr, as the line width is 2μm and the pitch is 4μm, the resulting nominal channel resistance is 135Ω. The maximum allowable current is approximately 1mA.

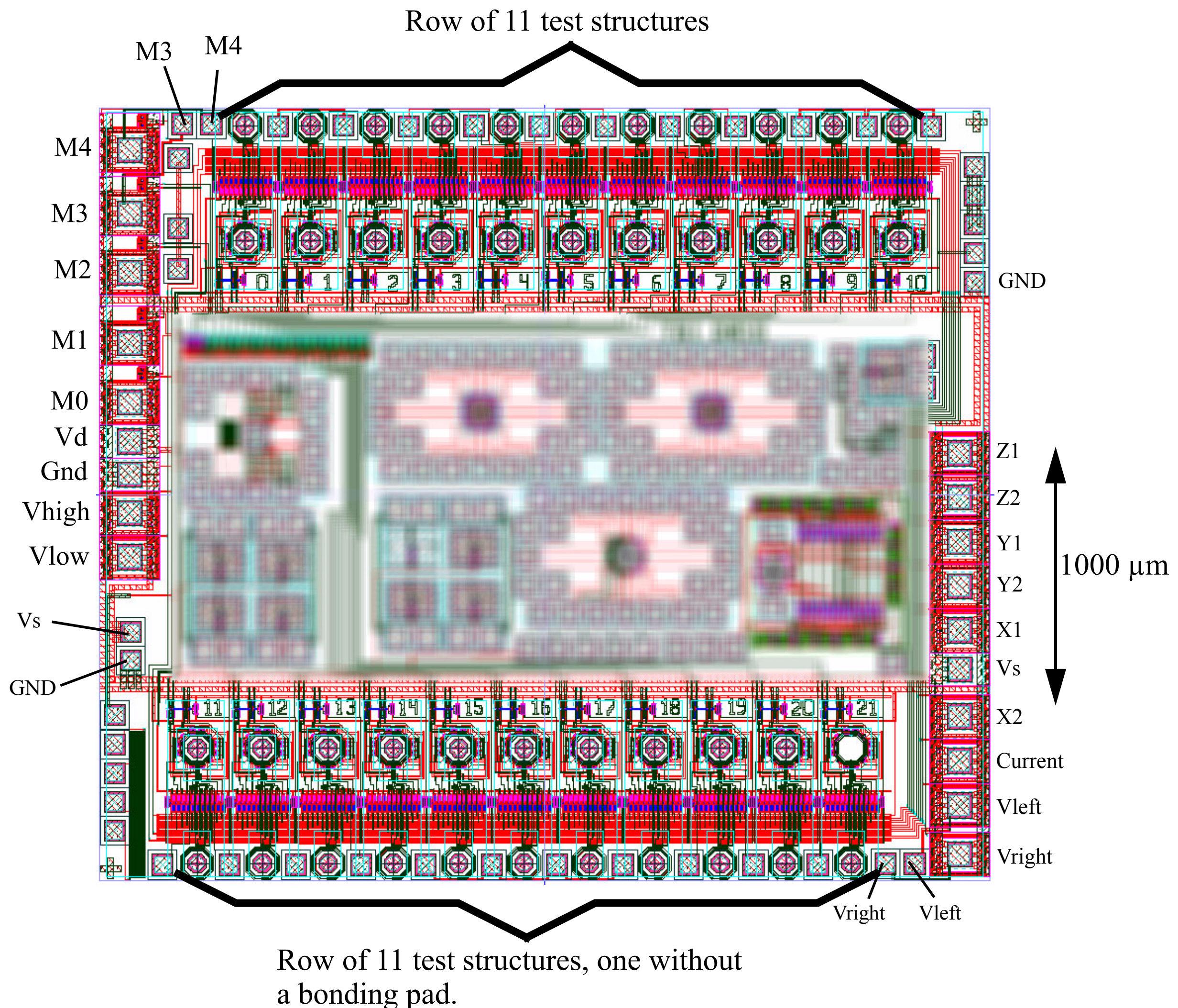

Fig. 25 Location of Structure 1's components and associated pads on the MUS chip. M0-4 are the inputs to control the decoder, Vd is the digital power supply, Gnd is the chip ground, Vhigh and Vlow measure voltage being supplied to the Wheatstone bridge RTDs, Vs is the supply voltage for the stress sensors, Z, Y, and X pads pairs are for the stress sensors, Current is for the CCS for the RTDs, and Vleft and Vright measure the voltage signal from the Wheatstone bridge RTDs.

To operate a constant current is run through the sensor line; changes to the steady state voltages correspond to applied forces. The substrate has two grounding pads which are joined in a circle around the sensor and at least one is required to ensure the sensor is operating correctly as seen in Fig. 27.

One of the linear z-force test structures is without a bond pad opening, instead only have the passivation layer above it, thus ultrasonic ball bonding can be applied multiple times without having the ball bond stick. This test structure also has a localized RTD so that temperature readings can be taken in addition to the underpad stresses, shown in Fig. 28.

2.4.3 Structure 3: Oversized Stress Pads with Single Stress Sensor

A standard stress sensor is placed underneath an over-sized bond pad so that the z-force can be characterized at various points around a ball bond. By placing the ball bond at different distances from the z-sensor, a two dimensional profile of bonding forces is generated. The sensor is at a 45 degree angle and shaped as a diamond to increase sensor length but minimize size. The sensors

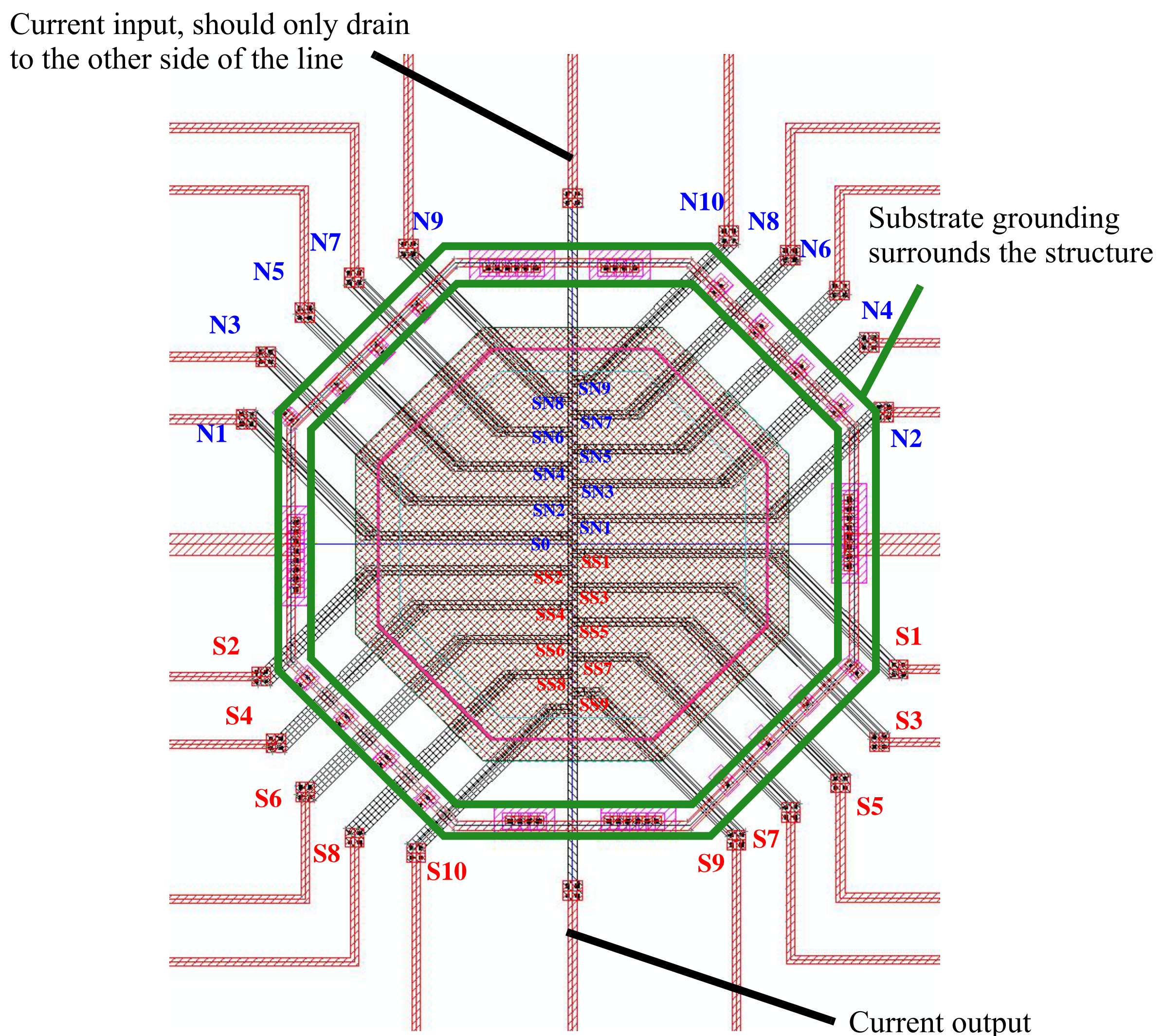

Fig. 26 Close-up view of MUS chip's structure 2: linear stress sensor and its 19 signal channels.

are arranged into groups of 4 so that they can be used in a Wheatstone bridge or individually. The resistance of an individual sensor is 1.7kΩ. The CAD layout of structure 3 is shown in Fig. 29.

The sensors in a Wheatstone bridge are to be supplied voltage ranging from 3-5 volts and the substrate grounded. The Wheatstone bridge connections between each sensor have to be completed either through wirebonds or with connections external to the package. To allow for a wide variety of sensor-to-ball-bond configurations (varying relative positions an orientations) the over-sized bond pad was made to be 100x150µm in dimensions. If it can be determined that having a prior ball bond on the pad does not effect subsequent measurements, it is possible to place multiple bonds on to the same pad in sequence, increasing the usage of each chip considerably.

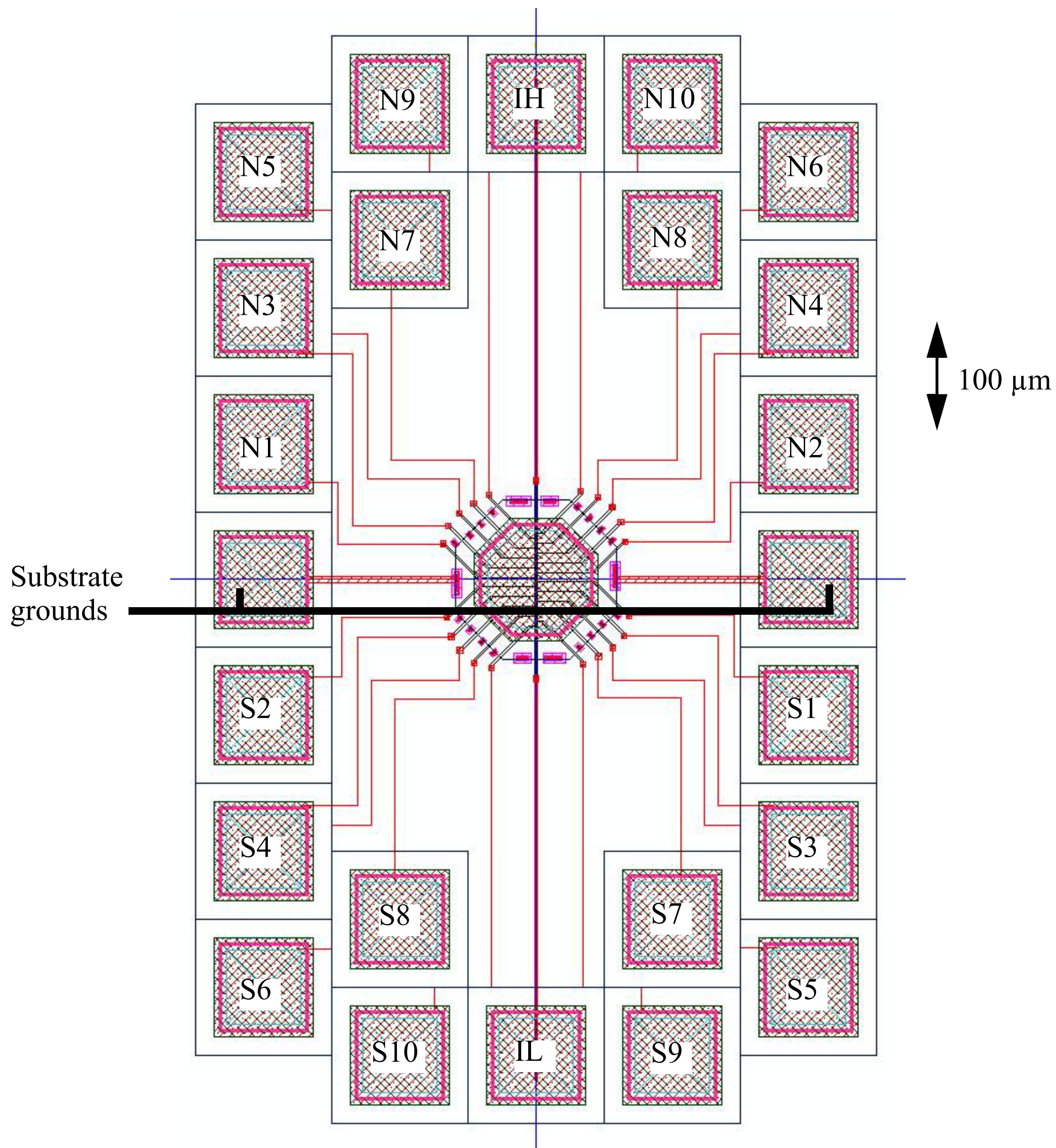

Fig. 27   MUS chip's structure 2: linear stress sensor with associated input and output pads.

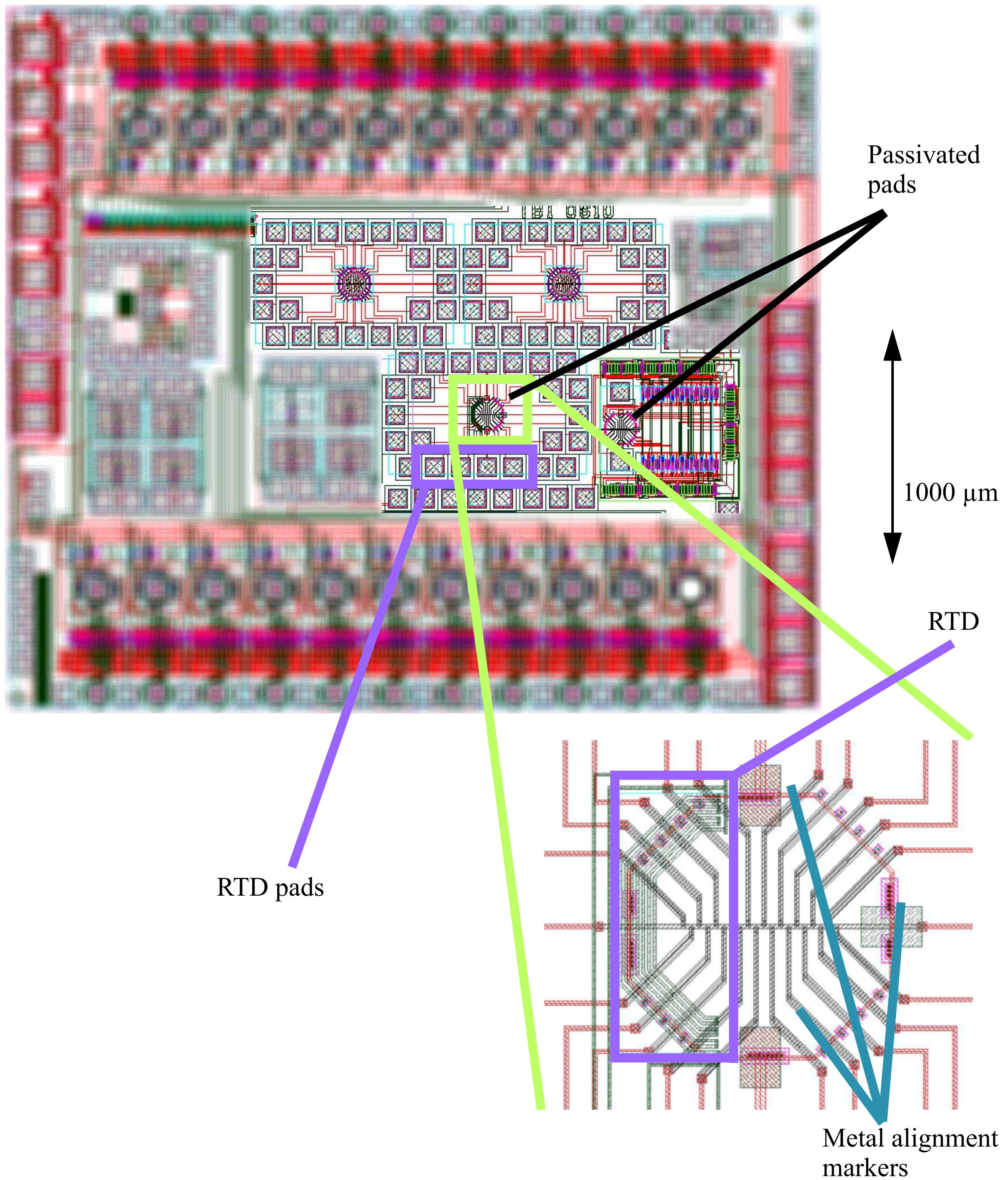

Fig. 28 Structure 2's(a) position on the MUS chip, along with a (b) close-up of the test bond site and related components. Passivated bonding areas and RTD shown as well.

One of the oversized pads is without metal or bond pad opening, so can be repeatedly used for in-situ ultrasonic tests as the ball bond can not stick. The position of structure 3 on the microchip is shown in Fig. 30.

2.4.4 Structure 4: Microheater

The microheater, whose layout is shown in Fig. 32, was designed in a silicon CMOS technology to implement both heater, logical components, and pad connections all on the same chip. The heater is supplied from a voltage controlled power source via two sets of metal lines, and the volt-

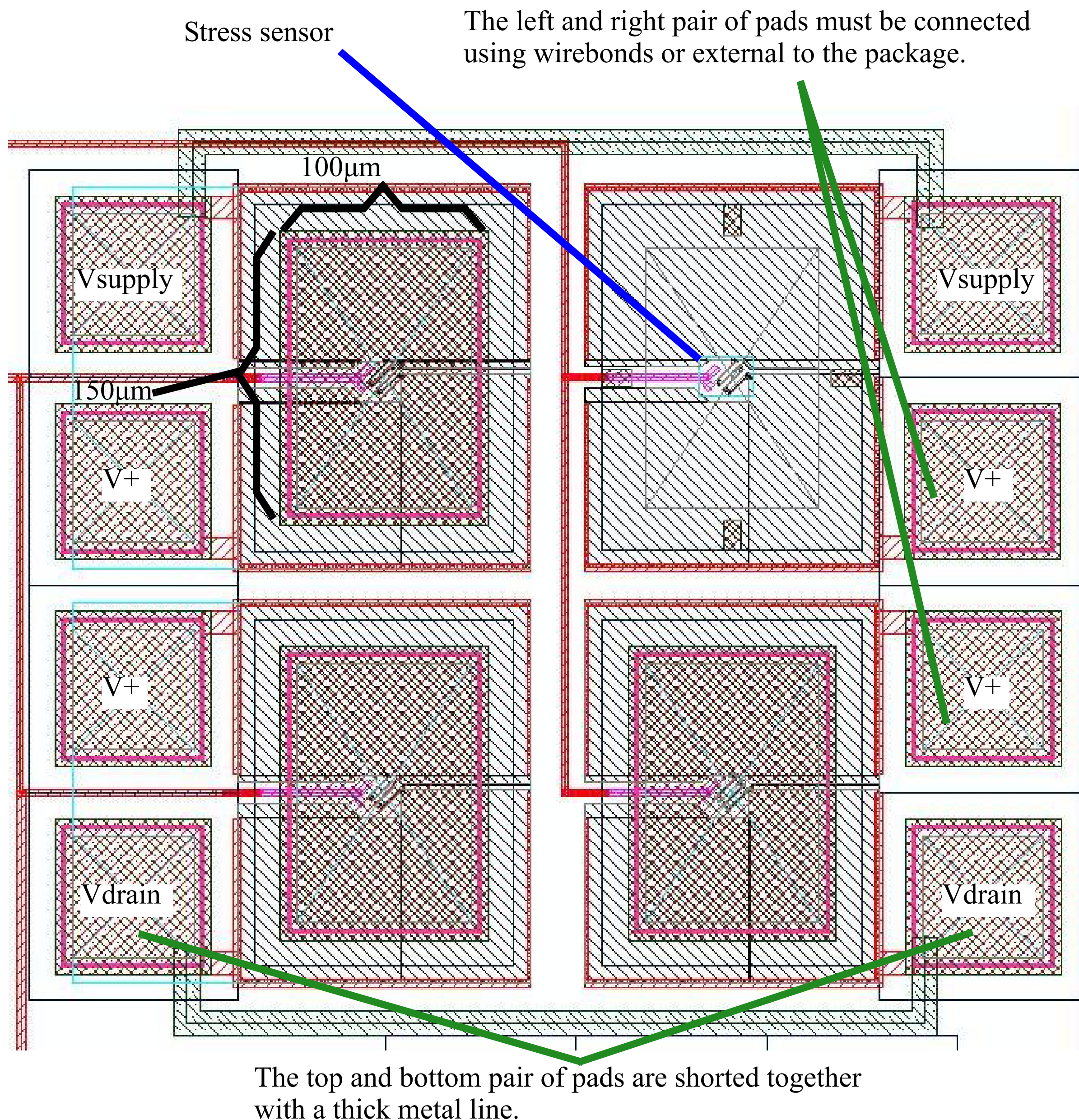

Fig. 29 The MUS chip's structure 4 has four local z-force sensors arranged to be accessible individually or as a Wheatstone bridge. Upper right sensor does not have a bond pad opening so can be bonded to repeatedly without having the bond pad stick.

age across the microheater is measured from 2 connections adjacent from the test pad. There are metals lines originating from each of the 4 corners of the test pad for measuring the pad resistance. A 50 Ω Al resistor is located 50 μm from the pad is used for monitoring the local temperature of the component.

The heating element is a N+ doped Si resistor and generates heat resistively. Because the bulk Si substrate is p-doped, the microheater creates a n-p diode interface between itself and the bulk Si, which prevents current from leaking out, meaning there is pseudo-electrical isolation from the rest of the bulk. A thin SiO_2 layer [27] separates the metal in the test pad from the heating component, as illustrated in the cross section of the test pad and heater in Fig. 31. The N+ Si has much higher resistance than the metal lines so most of the heat generated is at the N+ layer.

There are lines from each corner of the bond pad allowing for 4-wire measurement of the bond pad's resistance as well lines connected to the section of the microheater directly underneath the bond pad to measure the voltage across the heating element. It is also possible to use these connections for a 4-wire measurement of the ball bond resistance if a double ball bond is used. The position of the microheater on the microchip is outlined in Fig. 32, along with the CAD layout of the microheater itself.

The micro-heater can accept up to approximately 150 mA at 300 ºC when using both heater supply pads. The micro-heater should not be brought above 300 degrees or the surrounding aluminum lines undergo plastic deformation and be rendered inoperable. Typical operating temperature

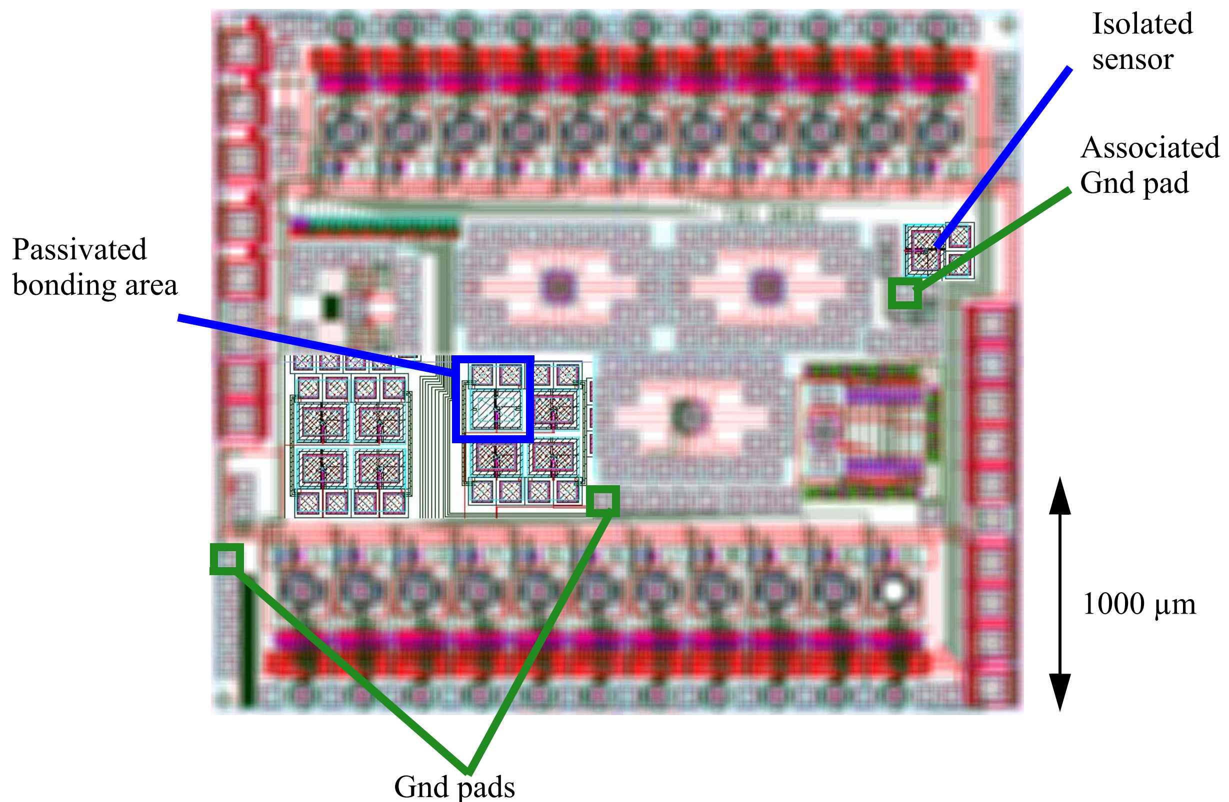

Fig. 30 Location of structure 3: oversized stress pad with sensor components and associated pads on MUS chip.

was designed to be between 200-250 ºC.Due to the large bulk of Si below the microheater, heat dissipation is rapid, cooling to within 10 ºC of room temperature in approximately 10 minutes. This makes temperature cycling of the ball bond possible so that sensitive microvolt measurements can be taken during the low temperature steps, when the microheater is off and there are no large electric field gradients in the heater to disrupt the measurements.

A micrograph showing a bird's eye view of the microchip is shown in Fig. 33, with all sensor and supply connection bonds made. The test bond in the center was left empty for pre-bonding characterization to be done.

2.4.5 Structure 5: On-chip Channel Switching Flip-Flop Chain for Underpad Stress Sensor

The ability to switch between the channels of the linear stress sensor on-chip enables cost and setup advantages, so a test structure to verify if the logic circuitry could work at the necessary

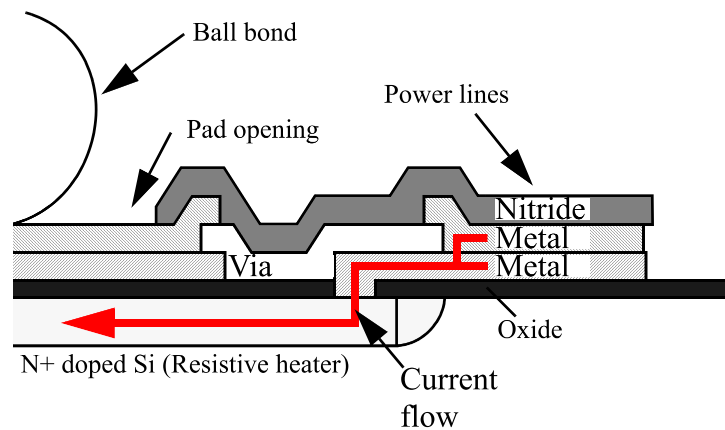

Fig. 31 Diagram showing lateral cross section of microheater on MUS chip.

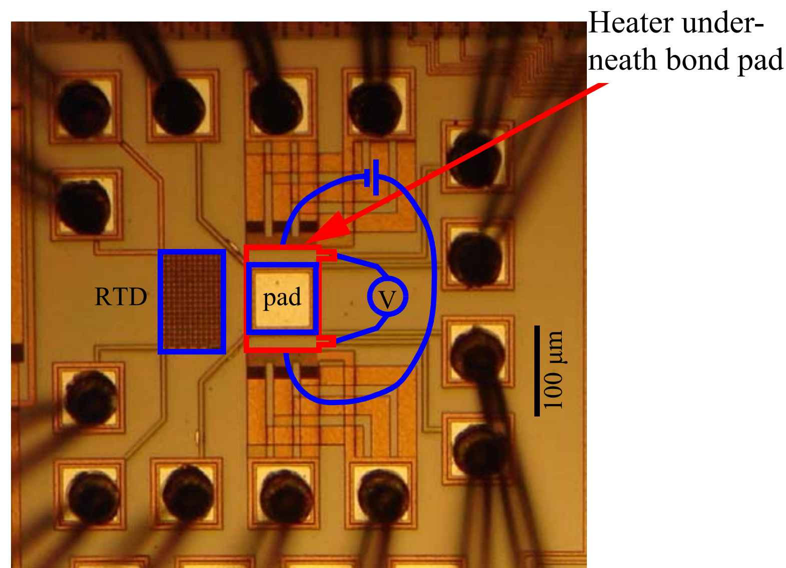

Fig. 33 Micrograph showing the MUS chip's structure 4: microheater and its bond connections to sub-structures. Overlaid with component outlines.

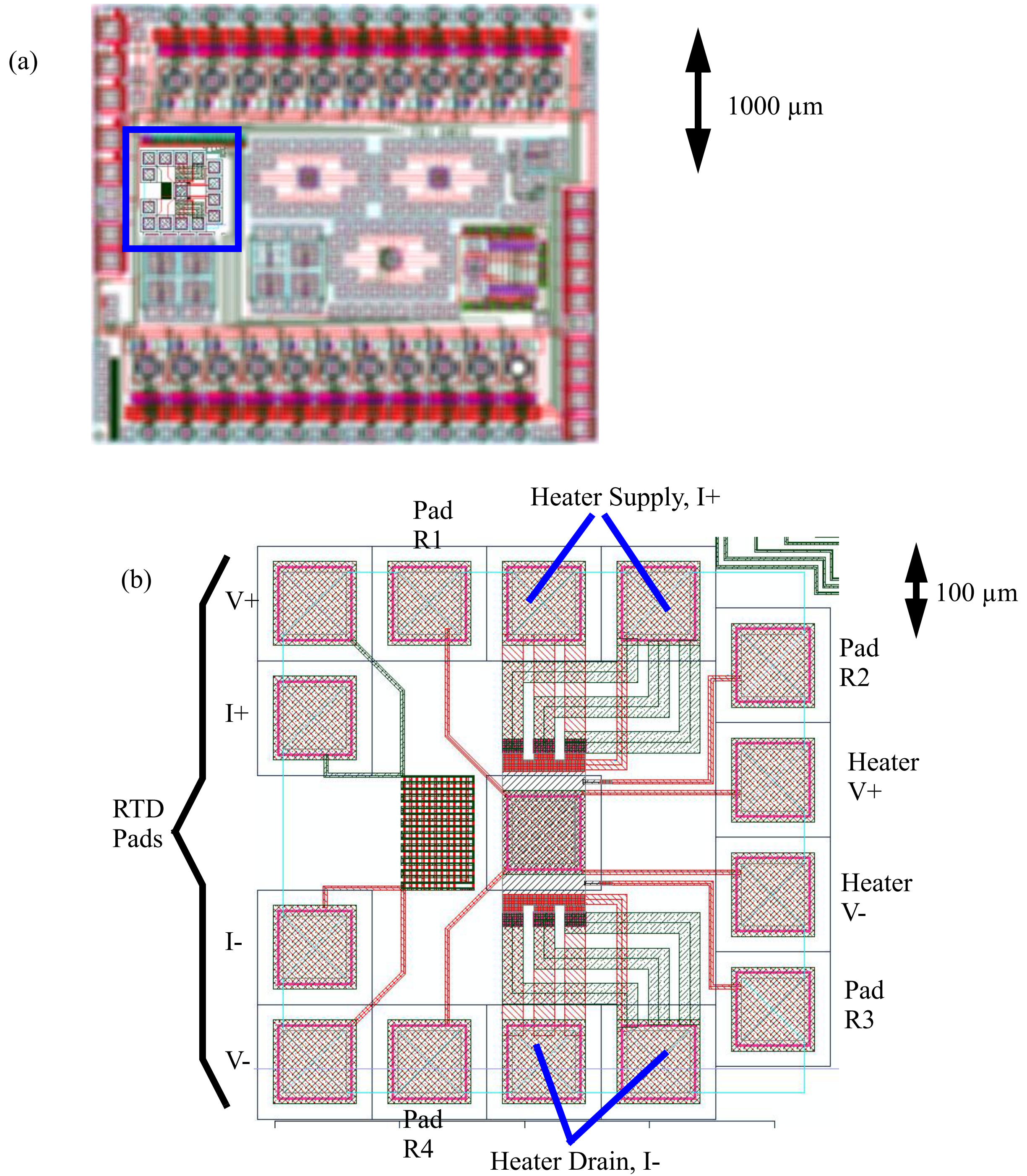

Fig. 32 Layout view of the MUS chip showing structure 4's (a) location on the chip of the microheater and (b) the I/O pads for all the sub-structures.

speeds was developed. Due to space constraints only 8 channels could be switched between, restricted by the amount of digital logic that is required per channel. The amount of space required to switch between all 19 channels would slightly exceed the space when using just bond pads due to wiring inefficiencies from only having 2 metal layers. To switch between channels effectively, a chain of D flip-flops (DFF) are used with set and reset connections so that the system can be held at the first channel until the experiment begins. The system is shown in Fig. 34.

Flip-flops are digital circuits whose output depends on three inputs and a clock; the inputs being an input signal, reset, and set, the truth table is shown in Table 5. Reset and set force the flip-flop into a 0 or 1 output, respectively, regardless of the input signal otherwise the output is the same as the input signal after every clock cycle. This means that the flip-flop retains its current value until a clock cycle is passed. Raising both Set and Reset values to high results in a race condition that does not have a definite resolution to any value. The clock signal is external and can come from an signal generator.

A flip-flop chain is created by connecting a row of flip-flops together, including the endpoints. The chain then carries a bit pattern indefinitely until a set/reset is used, the speed at which the bit

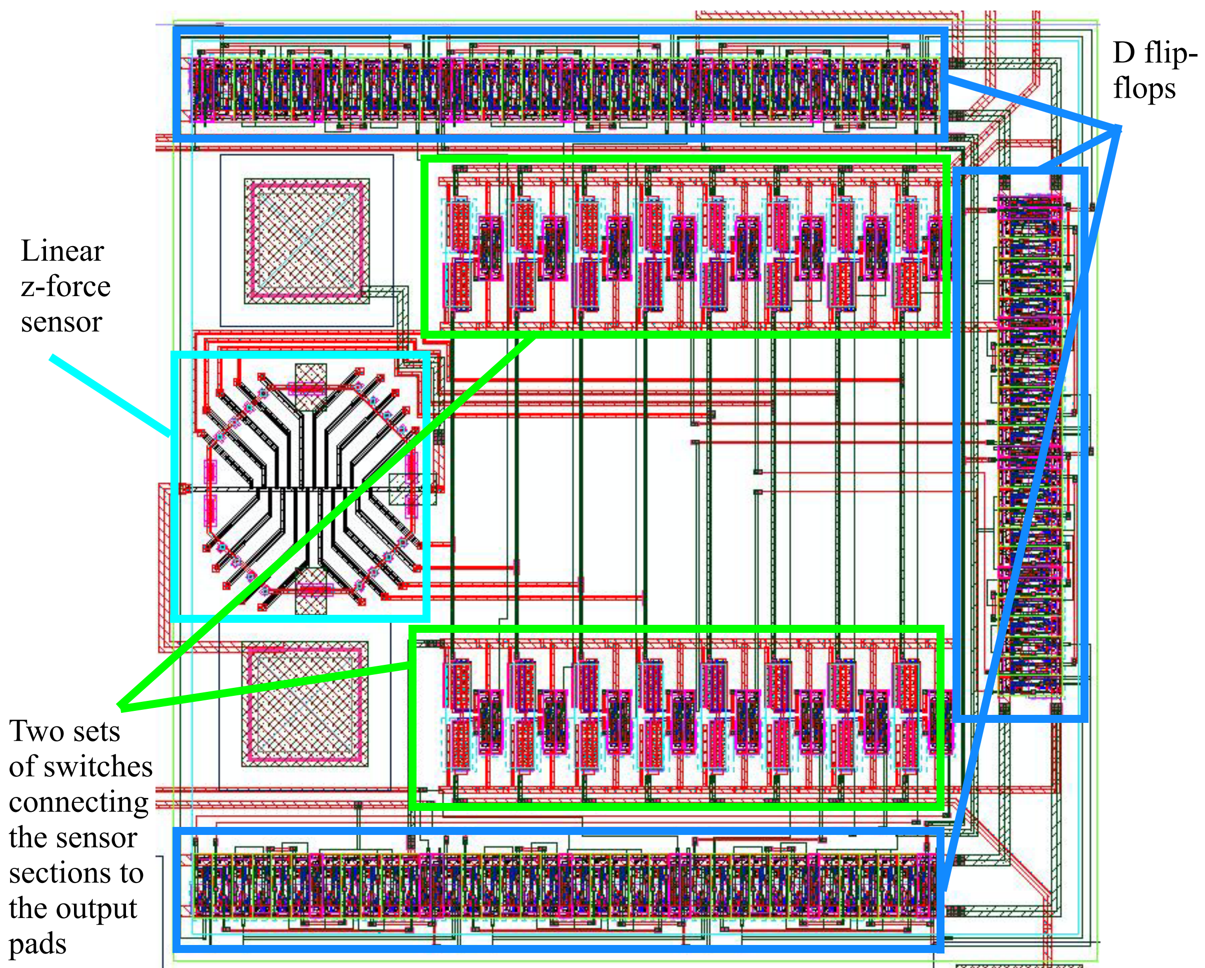

Fig. 34 The MUS chip's stucture 5 contains a flip-flop chain and associated switches connected to a linear stress sensor.

pattern progresses is dependent on the clock speed. The flip-flop chain's outputs are all fed into NAND gates which determine which set of switches to turn on ensuring only one channel is active at a time. For instance, the bit pattern used is 11000000 which activates the first channel using the first pair of switches. After each clock cycle, the bits move to the right (01100000) and a different pair of switches are activated from the NAND gate logic. A high level design diagram is shown in Fig. 35 to better illustrate the operation of the digital circuitry.

A specific channel can be held open by simply resetting the FF-chain, and only triggering the clock enough times to reach the desired channel. The maximum switching speed of these components is not known and must be tested -- the channel switching speed dictates the maximum frequency that the channels can be measured at.

2.4.6 Structure 6: High Current Switches

Due to the larger current requirements for switching of the power lines, a new switch design was needed. The old switch was adapted to allow for higher current flow up to ten times as much as with the old design. This allows for the supply voltage and ground connections for individual components to be gated from the main supply rails. A close-up of the new design is shown in Fig. 36.

The list of changes is as follows:

- Increased the size of the PMOS transmission gates by separating the two drains, allowing for a larger metal connection in the middle of the device.
- Increased the distance of the substrate biasing contacts on the PMOS by 1.3μm due to space needed for metal vias
- Added a second column of substrate biasing contacts for both the PMOS and NMOS.

2.5 Microheater and In-Situ Measurement (MISM) Chip Design

To further expand on the use of microheaters in reliability testing, a dedicated microheater chip was designed. This next chip design features the capabilities of previous designs, allowing parallel operation of test pads and in-situ measurement along with microheater technology.

2.5.1 Design

The MISM chip was designed with the Europractice 0.7 μm design kit using Cadence® and measures 1950 by 2450 μm. There are eight microheater structures connected to a bus and multiplexer, surrounding a single microheater structure independent from the rest of the chip, for a total of nine microheaters. As seen in Fig. 37 which shows the CAD layout of the entire microchip, including pad labels, the I/O pads line the top and bottom of the microchip while test bonding sites are along the left edge.

Table 5: Truth table for a D-flip-flop using in MUS chip

Set (S)	Reset (R)	Input (P)	Output (Q)
0	0	0	0
0	0	1	1
0	1	x	0
1	0	x	1
1	1	x	x

To expand on the in-situ measurement capabilities of the previous microheater, localized stress sensors were introduced. However due to space constraints only z-force sensors in Wheatstone bridge configuration could be fit between the heater supply lines and the local RTD. The test bond pad was changed from a square shape to octagonal, allowing the stress sensors to be closer to the bond location. Due to space constraints, the RTD was resized as well, from 50 Ω to 45 Ω, and uses both metal layers to maximize resistance in the limited space available. It is connected to the chip bus and can be supplied with up to 2 mA driving current in operation. There are two auxiliary pads which can be used for contact/pad resistance measurements if lead resistance becomes an issue for the nanovoltmeter. Microheaters number 1 and 6 have their auxiliary pads attached to the high and low voltage power lines for the microsensors instead for voltage testing measurements when characterizing the power switches. The CAD layout of one of the microheaters is shown in Fig. 38, highlighting the sub-components.

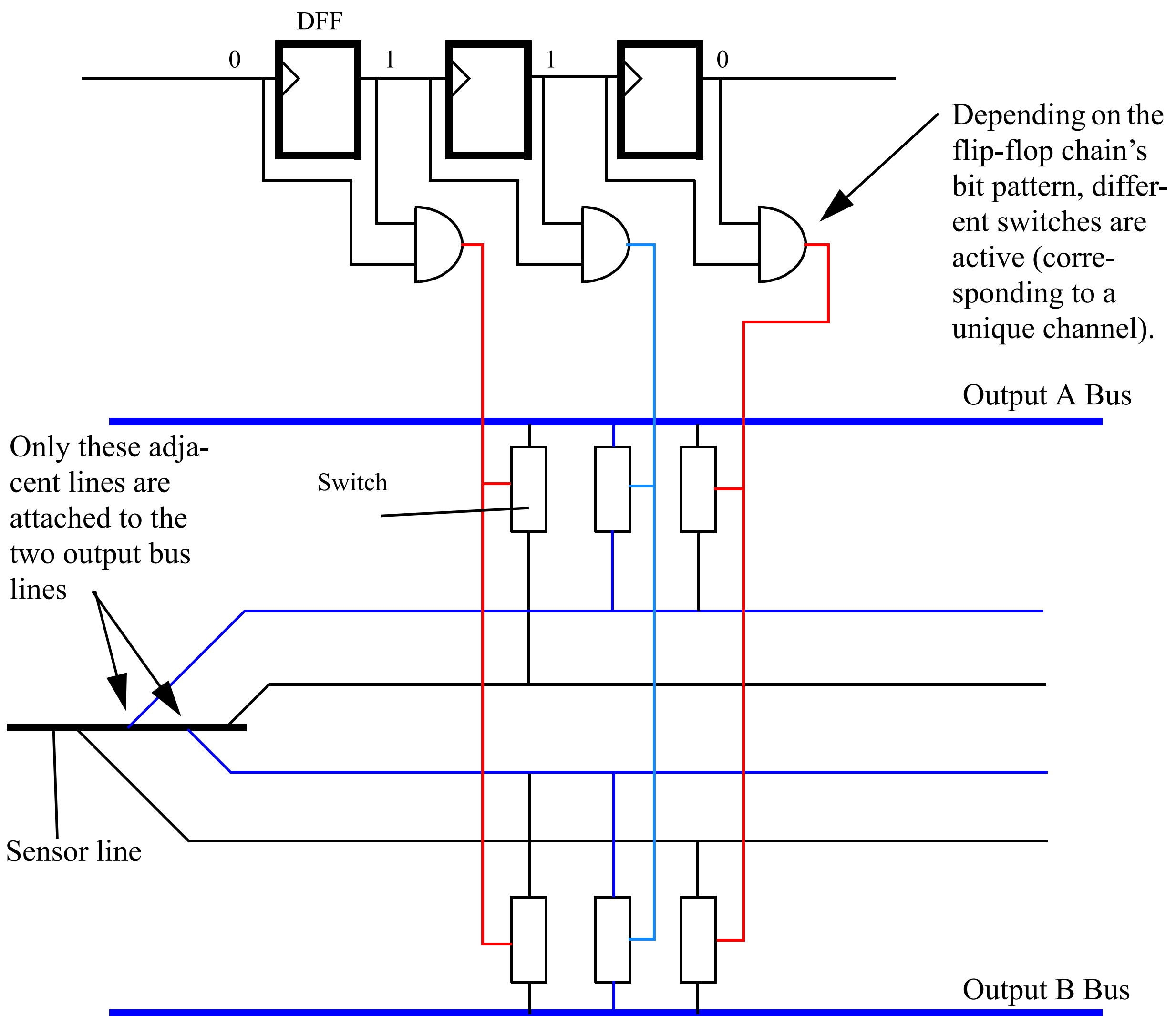

Fig. 35 High level design overview of the operation of the channel multiplexer in the MUS chip's structure 5. Uses DFFs to continuously switch between signals.

The maximum amount of current able to pass through the N+ layer has not been documented by the microchip fabricators, so for this iteration of the design, the allowable currents are based on the previous microheater's performance. The previous microheater was able to operate at currents exceeding 140 mA with a resistance of 120 Ω, using 261 vias. The new design's microheater has a resistance of approximately 112 Ω so the current to achieve a comparable temperature is slightly lower, and a similar number of vias were used (276). One consideration is that the neck of the heating component is only 50 µm in width which could constrain the maximum current depending on the maximum current density allowable in the N+ layer.

The off-bus microheater is a completely independent structure that is not connected to the chip bus or multiplexer. It has microsensors around the test pad and a local RTD, but no pad resistance capability due to space constraints. The layout of the sensors and RTD is exactly the same as the on-bus microheaters so this structure can be used to debug for any structural issues with the design. This structure is located exactly in the middle of the chip, as shown in Fig. 37. The pads and sub-components are labelled in Fig. 39.

The low current switches for previous chips were designed with low voltage and high resistance measurements in mind so the currents allowable were in the sub-milli-Ampere range. This new microchip design has several low resistance components requiring improved current thresholds in the switches. The metal widths of the transmission gates in the switches were increased from 1.0 to 2.2 µm and the number of vias from 2 to 8, meaning currents up to 2.5 mA at 150 ºC are allowable through the switches. The layout of three newly improved switches is shown in Fig. 40.

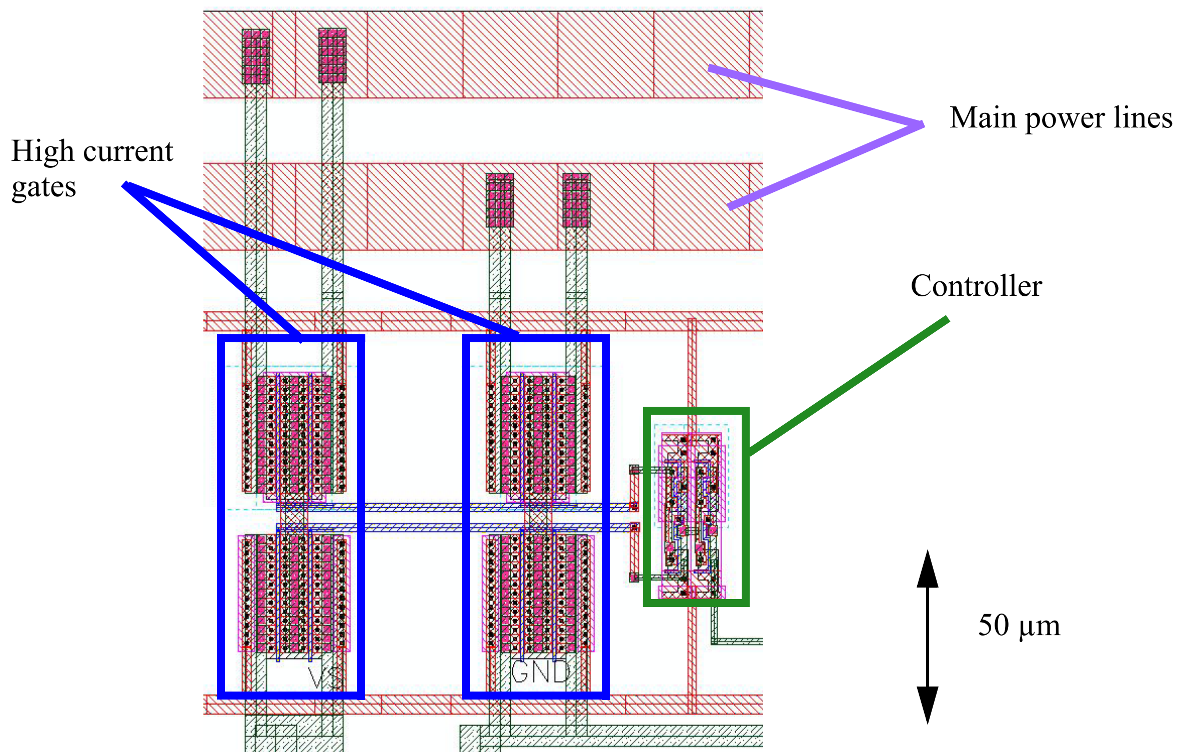

Fig. 36 MUS chip's high power switch used to gate connections to the ground and power supply.

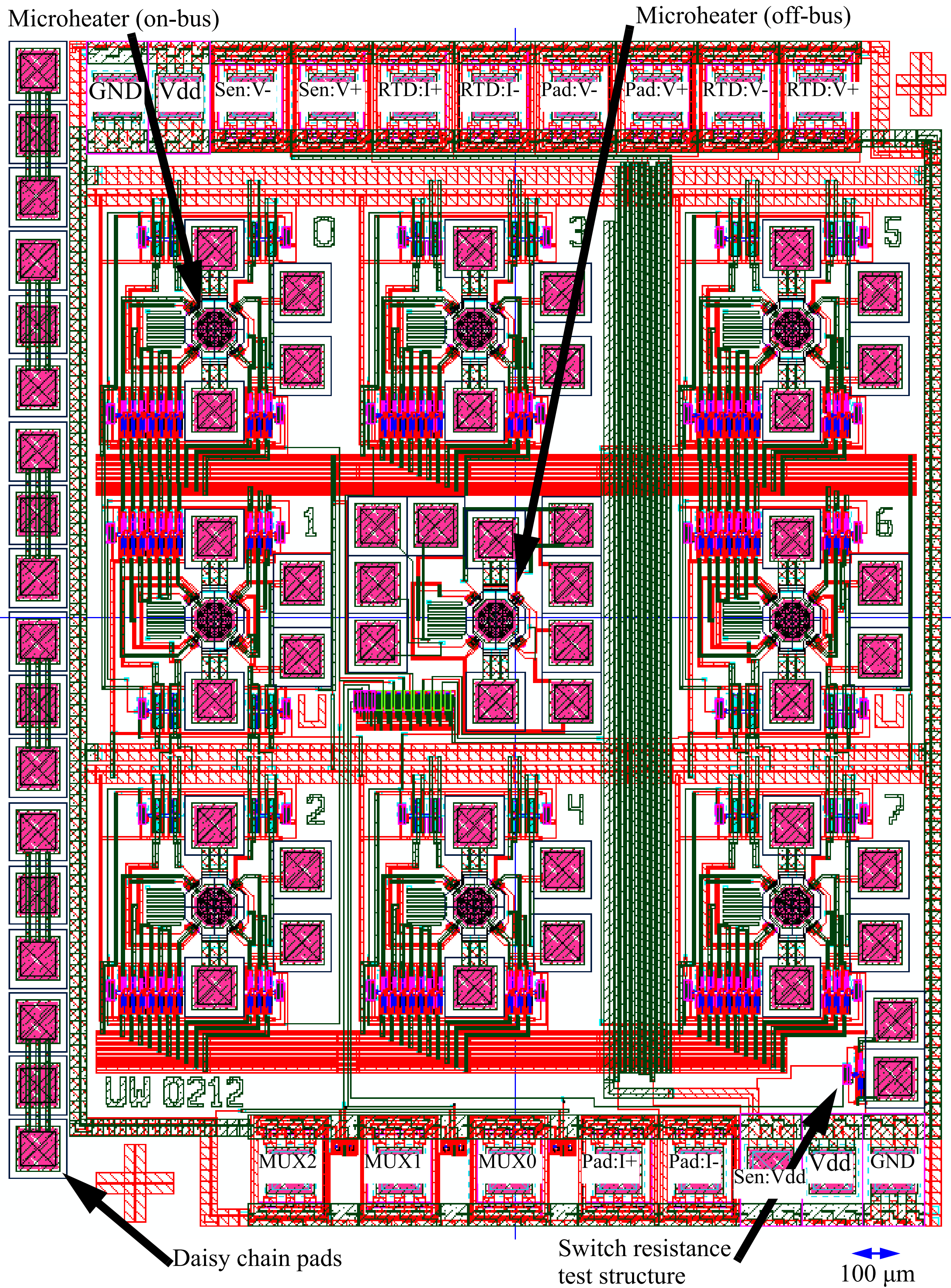

Fig. 37 Layout of the entire MISM chip.

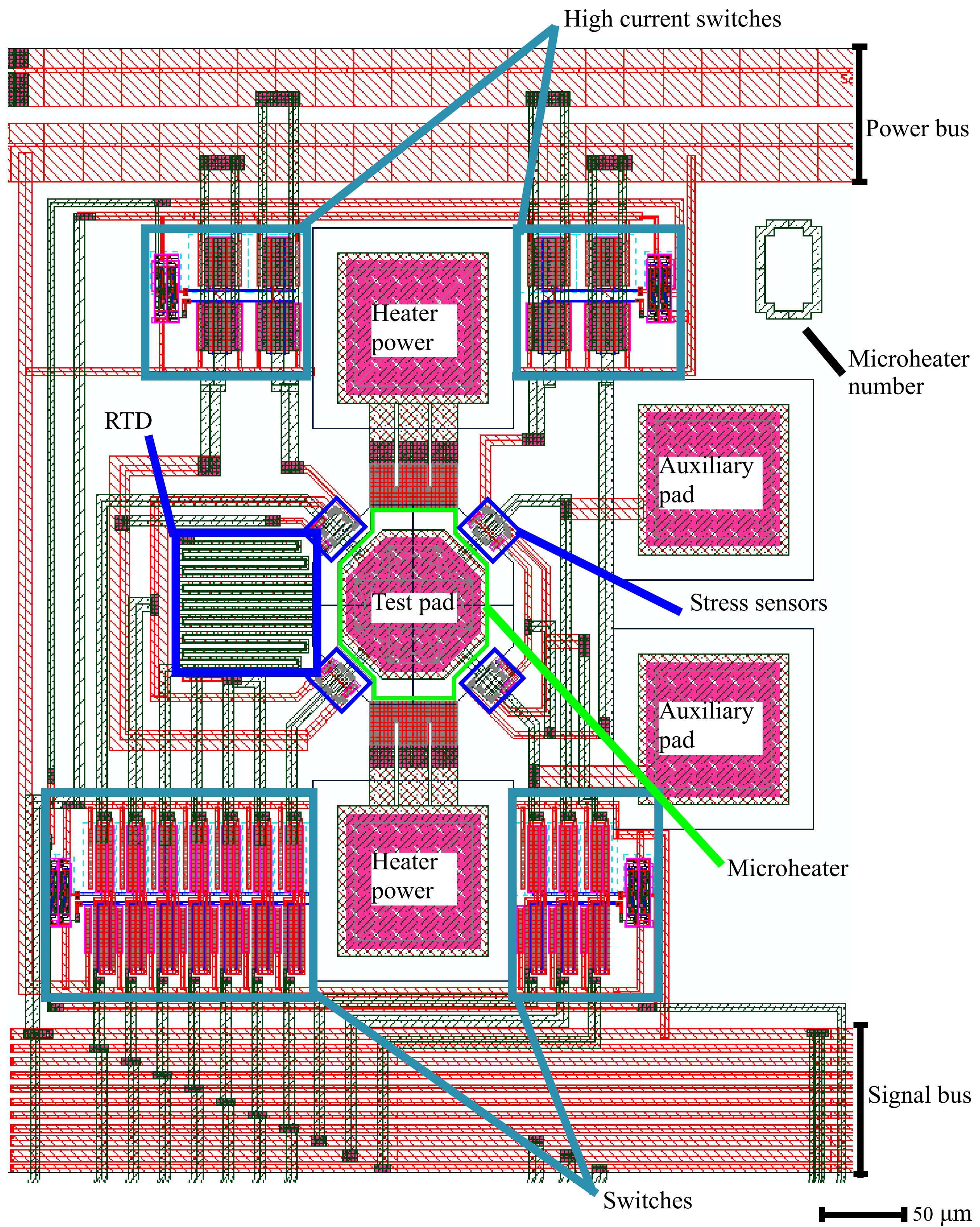

Fig. 38 Layout of an individual microheater on the MISM chip with each sub-component identified.

2.5.2 Switch Resistance

Due to the redesign of the switch, a test structure to measure the characteristics of the new switch was included. The voltage high and ground for this switch are shared with the main chip lines, and it is controlled by the MUX 0 control signal. The resistance measurement across the switch is done using 2 wire measurement.

2.5.3 Power Switch Voltage Drop

For microheaters number 1 and 6, the auxiliary pads are connected to the ground and power lines (after they go through the power switches), to determine the amount of voltage drop from the power supply to the sensors. The measured voltage drop is cumulative of the line resistance and the switch resistance.

2.5.4 Bonding diagrams

Since the microheaters are positioned in a square, there are multiple ways to bond the microchip using a 28 pin package. While it is possible to operate all 8 multiplexed microheaters at a time as

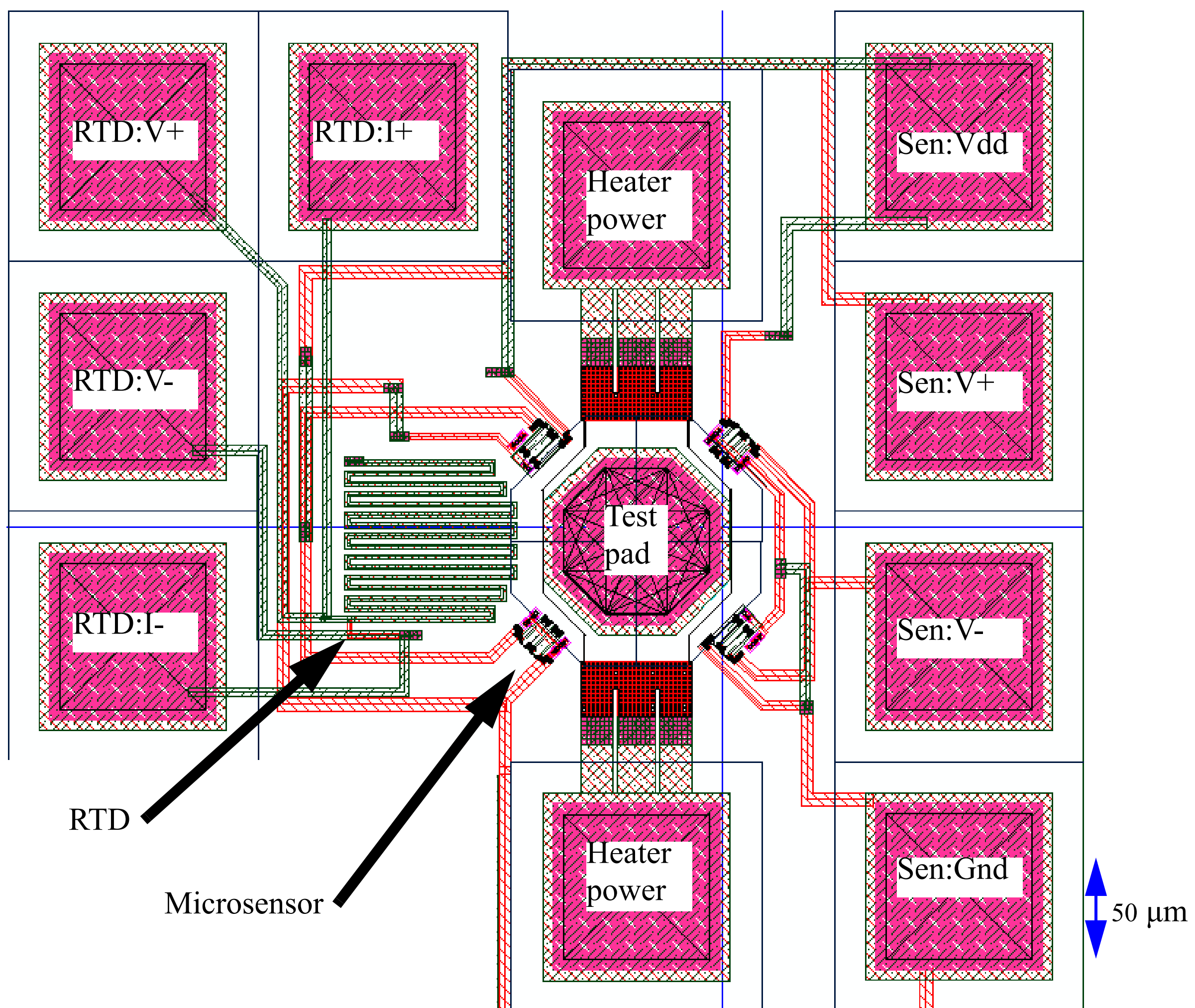

Fig. 39 MISM chip’s off-bus microheater. Structure is completely independent from the rest of the microchip.

seen in bonding diagrams 1-3 in Appendix F, this requires the grounds for microheaters to be shared for the entire chip. Bonding diagram 4 shows how to bond the chip using the auxiliary pads for pad resistance measurements.

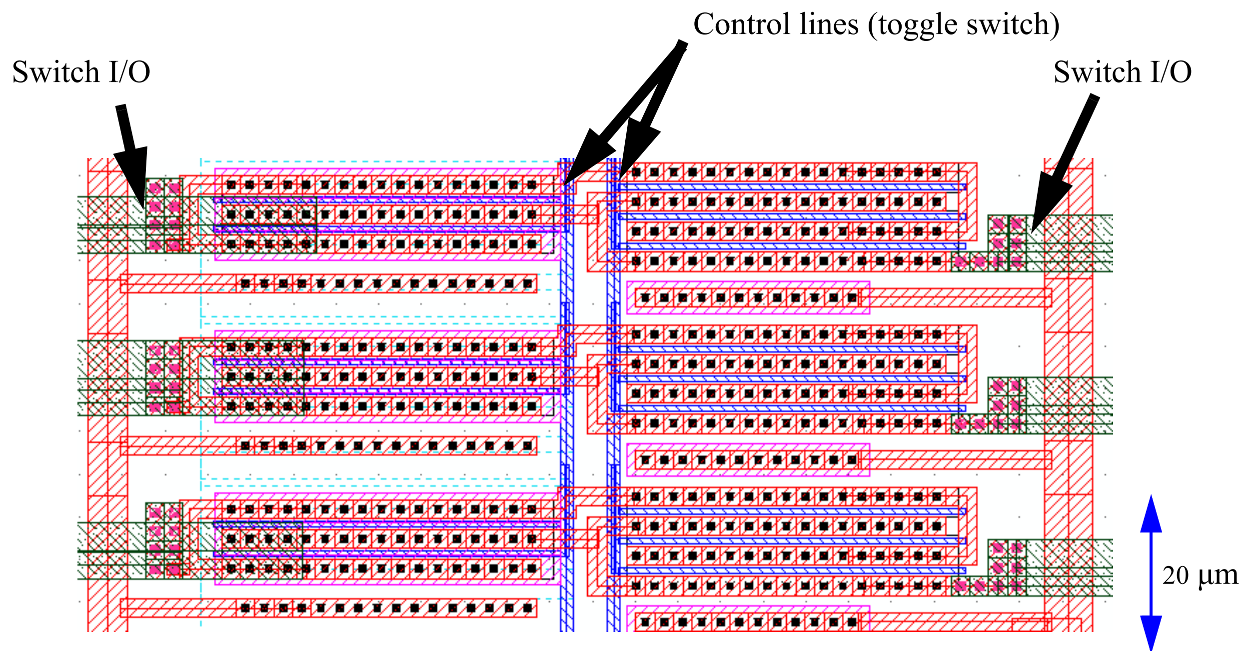

Fig. 40 Layout of three switches on the MISM side-by-side. The layout is rotated 90 degrees in this figure to conserve space.

3. Results of Microheater Experiment

The experimental plan is to use the MUS chip's fourth structure (microheater) to prove functionality of the microheater concept for aging a ball bond with rapid, high temperature storage. Then the novel in-situ measurement method of using pad resistance to monitor the ball bond during aging is also shown during the aging of a single Au ball bond at 250 ºC for 150 h. The setup for this experiment is shown, the microheater characterization is summarized, and then the results of aging the Au ball bond is shown.

3.1 Equipment

The setup used consists of a sample holder underneath a microscope (Nikon Measurescope UM-2), constant current sources (both custom made and Agilent B2911A), computer controlled voltage supply (Agilent E3649A), DAQ (MC USB-1208FS), multimeters (Agilent 34411A), and nanovoltmeter (Agilent 34420A) as shown in Fig. 41. A computer is used to run the Matlab scripts operating all the equipment and storing the measurement data, which are listed in Appendix A. The thermal characterization script is called "temp_characterization.m", the power characterization script is called "heater_setvoltage_v02.m", and the cycling experiment script is called "heater_longterm_cycling.m". The schematic of the setup is shown in Fig. 42.

If the room's temperature range throughout the day becomes an issue, due to the resistance of subcomponents changing with temperature, the setup can also be placed in an inactive oven so the insulation can dampen external temperature fluctuations. An inverted petri dish bottom is used to cover the sample when in an oven to prevent particulate matter from collecting on the microchip surface. To further insulate measurement and power lines from EM radiation (radio, etc), all

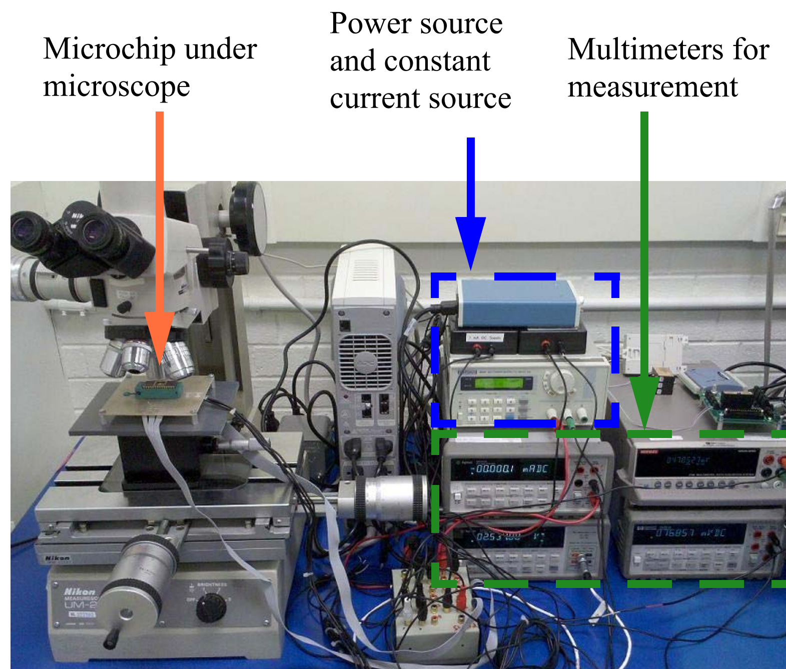

Fig. 41 Setup used for running of microheater experiments.

paired, non-ribbon wires are twisted together. To remove electrothermal effects from the pad resistance measurement, a constant current source able to continuously switch current direction is used [28].

The scripts listed in Appendix A are capable of controlling the microheater for any defined amount of time to cycle an user-defined temperature profile in a step-wise format, such as a step function or staircase function. Pad resistance data can be recorded throughout the experiment however only during the zero power stages can it be considered useful so every cycle should include at least 10 minutes of 0 power to enable the sample to cool to room temperature and stabilize. When the microheater is powered, the large electric fields across the bonding pad skew any pad resistance measurement. The connection diagram in Fig. 43 shows how the equipment should be connected to the package.

3.2 Software

The software script is capable of controlling the microheater for any user-defined amount of time to cycle a user-defined temperature profile in a step-wise format, such as a step function or staircase function. Pad resistance data can be recorded throughout the experiment however only during the zero power stages can it be considered useful so every cycle should include at least 15 minutes of 0 power to enable the sample to cool to room temperature and stabilize.

The data from the nanovoltmeter and multimeters, along with voltages is written to a text file on the computer's hard drive for later analysis. The script displays a plot showing the pad resistance, temperature, and heater state for the latest 2 hours of operation, this ensures for extremely long tests, there are no memory shortage issues while trying to plot several hundred hours worth of data. The temperature is controlled using a PID feedback loop where the voltage is adjusted depending on the temperature value.

3.3 Test Materials

The microheater was bonded with optimized Au ball bonds for the sensor and supply lines, which saw no visible IMC formation even if the microheater was held at 300 ºC for several hundred hours. The test bonds were also Au ball bonds. A micrograph of a bonded chip is shown in Fig. 44.

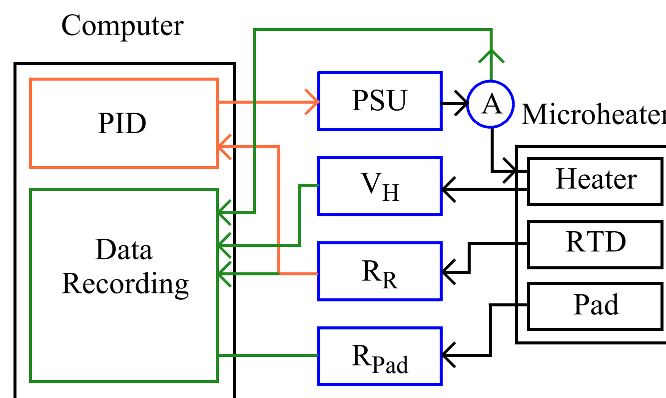

Fig. 42 Layout and connections of equipment in the microheater setup.

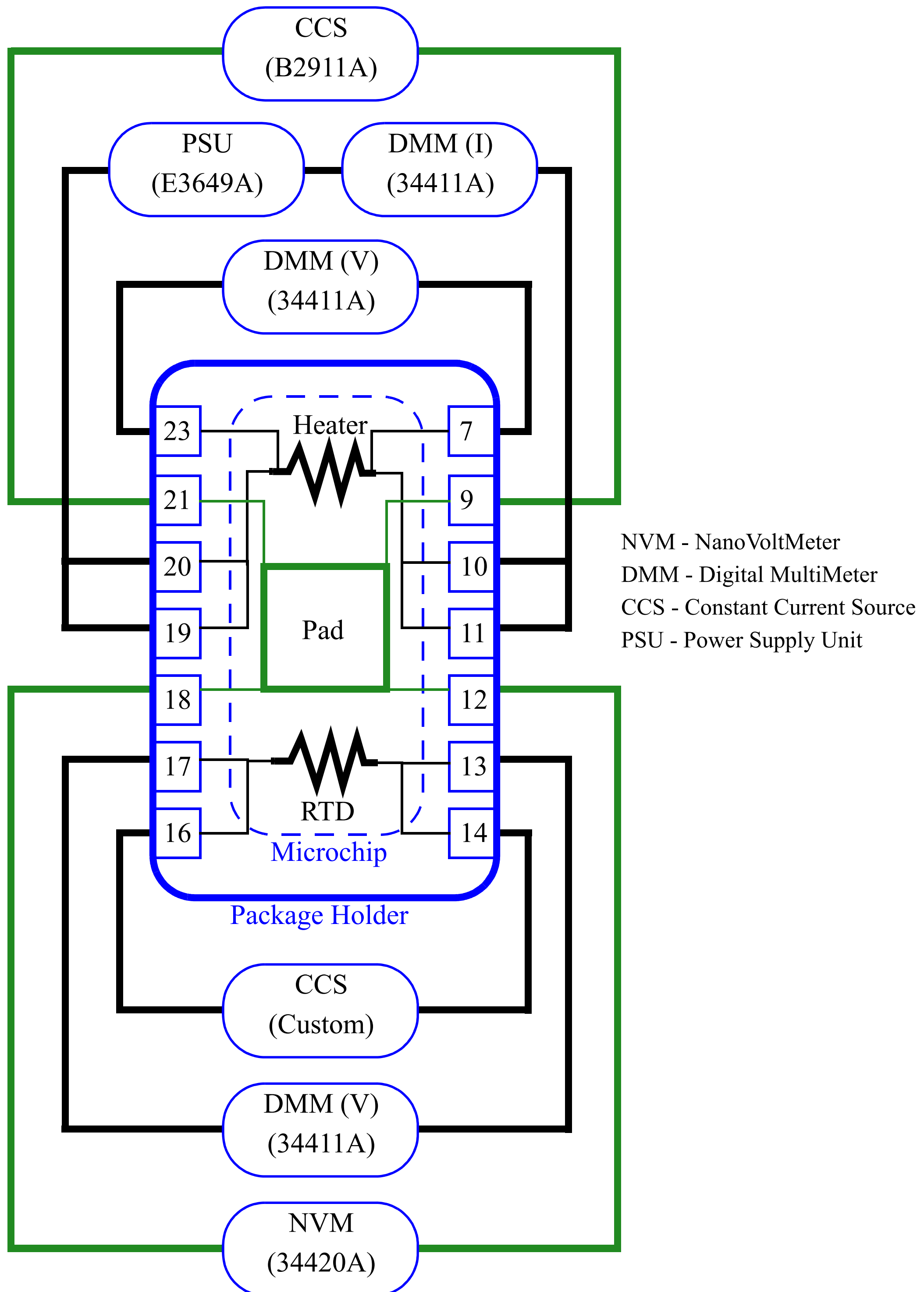

Fig. 43 Diagram showing which pieces of equipment connect to which package pin numbers for the microheater experiment.

In this thesis Au ball bonds are used to characterize and determine the capabilities of the microchip designs since Au ball bonds are well understood and the results from the microchip can be freely compared to existing data. Bonding surfaces are either Al containing 1% Si on the microchip, or Au on the ceramic dual in-line package (CERDIP).

3.4 Characterization

To determine the relationship between temperature and resistance of all the subcomponents of the microheater and six samples were used, denoted Q01 to Q06. Each of the samples was heated in an oven while the resistance was measured. The oven's temperature was ramped up in steps of 30 ºC from 30 ºC to 90 ºC, and at each of the steps, the resistance and temperature were averaged. A linear fit of these points was used to establish a temperature versus resistance equation.

The thermal characterization results in slope and y-intercept values m_R and b_R for the RTD and m_H and b_H for the microheater, respectively, based on the linear approximations of the R(T) curves,

$$R_R = m_R T + b_R \quad \textbf{[Eq. 3]}$$

$$R_H = m_H T + b_H \quad \textbf{[Eq. 4]}$$

Values for m_R, b_R, m_H and b_H are given in Table 6 for samples Q01 to Q05.

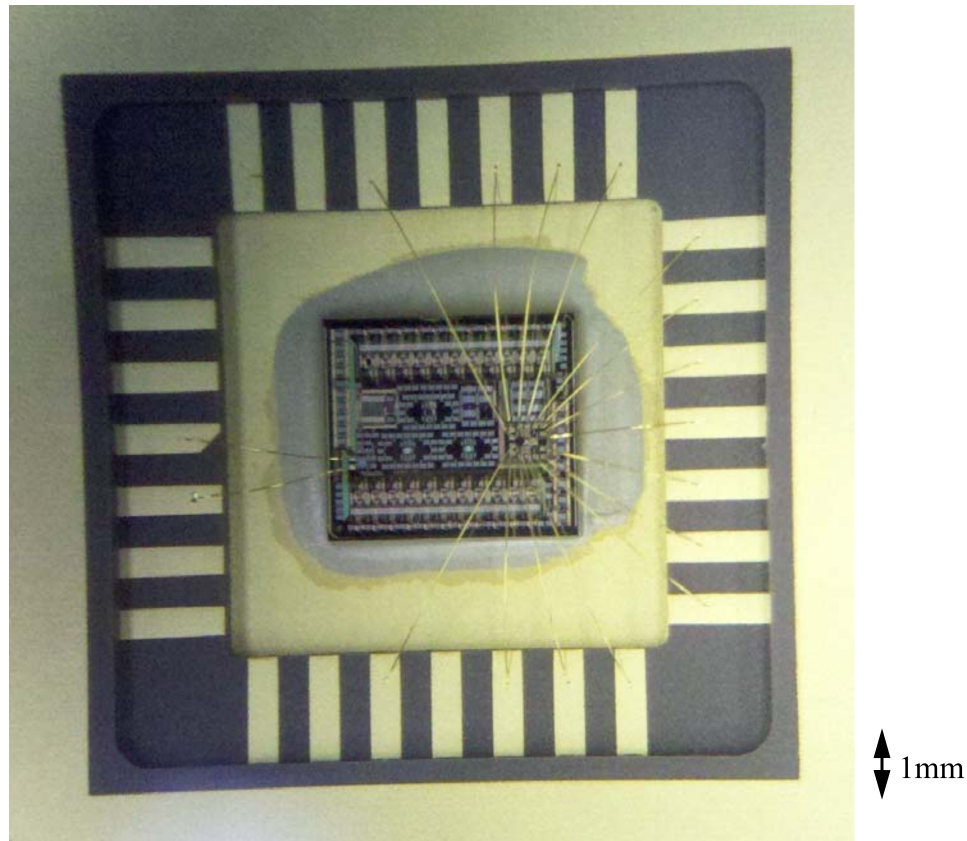

Fig. 44 Photograph of the bonded sample TC5 (MUS chip), the curved edges of the package are due to the camera's lens warping straight lines.

Following the thermal characterization, the samples underwent self-heating characterization to find the temperature disparity between the RTD and the heater itself. The microheater was ramped up by supplying voltages in steps of 1V up to 10V while the resistance of each subcomponent was measured. Then for each ramp step, once the self-heating temperature stabilized, the resistance was plotted versus the power running through the heater. Linear fits for power values low enough to show a linear relationship were produced linking the heater temperature to the RTD temperature. An example of these correlations for sample Q01 is shown in Fig. 45.

The power characterization results in slope and y-intercept values n_R and c_R for the RTD and n_H and c_H for the microheater, respectively, based on linear fits of the *R(P)* curves for power values below 1 W,

$$R_R = n_R P + c_R \quad \textbf{[Eq. 5]}$$

$$R_H = n_H P + c_H \quad \textbf{[Eq. 6]}$$

Values for n_R, c_R, n_H and c_H are given in Table 7 all the Q samples.

This method was used over directly sampling the heater resistance due to non-linear effects once the temperature exceeded 150 ºC, see Fig. 46.

3.5 Effect of Ball Bond on Calibration

While all calibration of the microheater was done with the test bond already on the microheater, to understand the effects the presence of a ball bond had on changing the calibration a sample was made to test this. First only the bonds for power and sensing were made and the calibration of the microheater and RTD were done. Then after the test bond was placed the calibration was done again. Due to some issues with the bonding process, sample TC3 was missing the usual heater voltage connections, instead measuring heater voltage from the power lines, as seen in Fig. 47. This resulted in the heater resistance being 20 Ω higher than what it would be otherwise, due to the measurement including line, via, and doped Si resistances. However, this did not affect the calibration with respect to temperature.

Table 6: Thermal Characterization of Microheaters

x-axis	y-axis	Property	Q01	Q02	Q03	Q04	Q05	Q07	AVG	STD
Oven Temp [°C]	Heater Resistance	m [ºC/Ω]	0.1198	0.09138	0.0959	0.1289	0.1435	0.1347	0.119	0.020
		b [ºC]	73.41	75.42	74.28	73.40	83.99	69.62	75.0	4.0
	RTD Resistance	m [ºC/Ω]	0.1618	0.1209	0.1265	0.1706	0.1703	0.1721	0.150	0.022
		b [ºC]	45.47	46.71	45.65	44.62	45.84	44.64	45.66	0.67
RTD TCR @ 20ºC		[10^{-3}/ºC]	3.316	2.454	2.628	3.553	3.46	3.576	3.16	0.45
Heater TCR @ 20ºC		[10^{-3}/ºC]	1.58	1.18	1.26	1.696	1.65	1.86	1.54	0.21

Table 7: Power Characterization of Microheaters

Component	Property	Q01	Q02	Q03	Q04	Q05	Q07	AVG	STD
Heater Resistance	n [ºC/W]	16.45	16.38	16.04	16.37	15.18	18.53	16.5	0.47
	c [ºC]	71.87	74.17	74.83	76.6	87.2	70.45	75.8	5.4
RTD Resistance	n [ºC/W]	12.27	14.76	13.23	14.13	11.86	14.54	13.5	1.1
	c [ºC]	48.43	49.67	48.56	48.86	49.86	49.49	49.1	0.58

Tables 8 and 9 show the changes to the thermal and power characteristics. For the thermal characteristics, the y-intercept values did not change significantly while the slope changed by 4.5%, indicating the presence of the ball bond is affecting thermal sensitivity. For the power characterization, it becomes clear that the ball bond's presence has reduced the ability of the heater to achieve a desired temperature, which is shown visually in a plot in Fig. 48.

3.6 Temperature Control Methods

The control of the microheater when ramping to a specific temperature can be done in several ways. One is to keep a look-up table where certain voltages correspond to previously measured temperatures and then to extrapolate required voltages for temperatures not on the look-up table. This has the disadvantage of the code needing to be updated for every microchip and since voltages are extrapolated anyway, this is inefficient coding. Another disadvantage is that the heater is

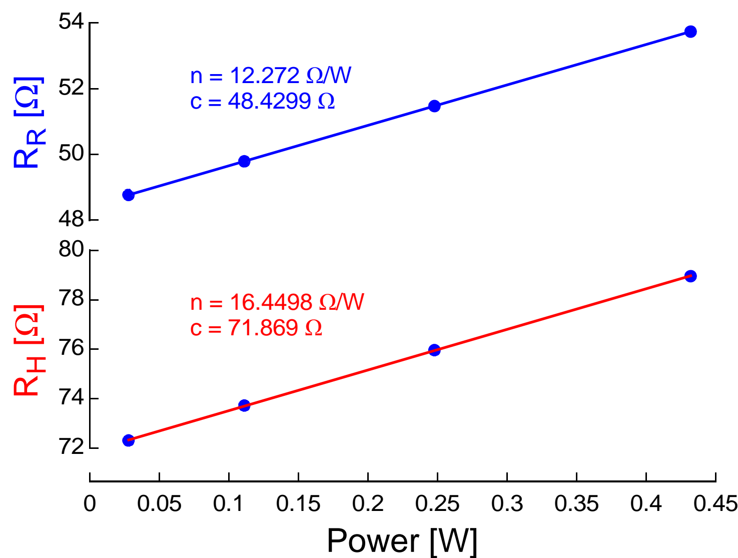

Fig. 45 Example values obtained during power characterization of sample Q01.

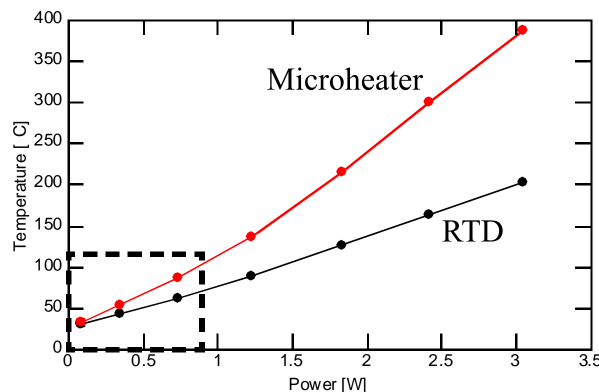

Fig. 46 RTD and microheater temperatures at various power levels. Values in dashed box are used for the determination of the heater versus RTD temperature extrapolation, as non-linear effects are observed at higher temperatures.

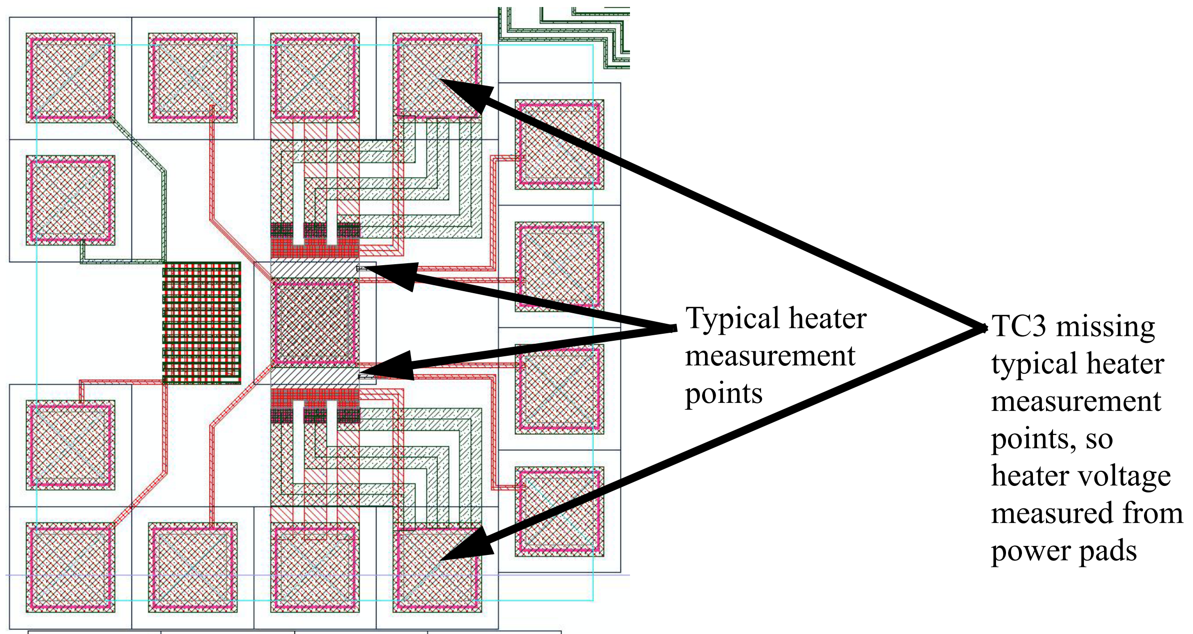

Fig. 47 Schematic showing the modifications to how the heater's voltage was measured for sample TC3. These changes do not change the temperature characteristics, but would show a resistance offset compared to other samples due to the extra line resistance from the vias and portions of the N+ dopped Si directly beside the vias at the edges of the microheater.

Table 8: Thermal Characterization Differences

	R = mT+b	unbonded	bonded	% diff
RTD	m [Ω/ºC]	0.1576	0.1647	4.5
	b [Ω]	45.55	45.49	-0.1
Heater	m [Ω/ºC]	0.1482	0.1549	4.5
	b [Ω]	92.66	92.59	-0.1

Table 9: Power characterization differences

	T = mP+b	unbonded	bonded	% diff
RTD	m [ºC/W]	74.63	71.46	-4.2
	b [ºC]	26.21	24.31	-7.2
Heater	m [ºC/W]	108.8	103.9	-4.5
	b [ºC]	25.96	24.19	-6.8

only set to the required temperature so the ramp time is longer than if the heater is set to a higher voltage first and then reduced as it heats.

Another ramping method is to use a PID feedback loop. The PID feedback loop is a simple control theory tool where the error signal between the actual temperature and the desired temperature is used to calculate the voltage of the microheater continuously, the abstract schematic of a PID controller is shown in Fig. 49. The PID controller calculates the voltage by using 3 previously calibrated values, one for multiplying the error signal itself (proportional term), one for multiplying with the differential (rate of change) of the error signal, and one for multiplying with the integral (sum) of the error signal.

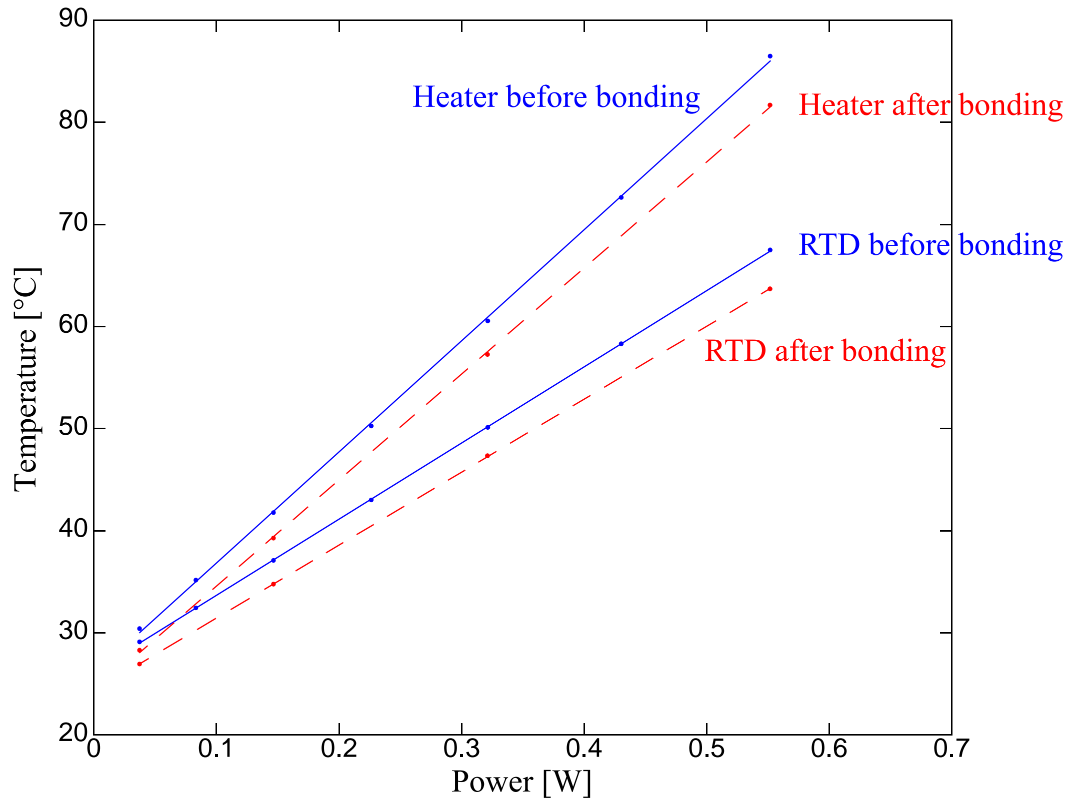

Fig. 48 Plot showing the temperature vs power characterization of a microheater before a test ball bond was made (solid) and after the ball bond was made (dashed).

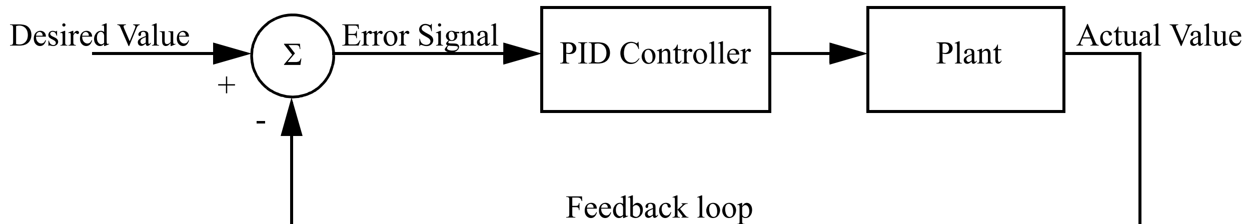

Fig. 49 Schematic of the PID controller feedback loop. The PID Controller directly operates the Plant, which is the system which needs control, using the error signal between the actual value and the desired value to adjust the control signal going to the Plant.

To get theses PID values first the system being controlled, otherwise known as the “Plant” in control theory, must be approximated with a mathematical formula. In our analysis, a fourth order system is used as a compromise between accuracy of the model and complexity, the equation shown in Eq. 7.

$$G(s) = \frac{U}{As^4 + Bs^3 + Cs^2 + Ds + E} \quad \textbf{[Eq. 7]}$$

Then the microheater ramped with a step function input and this response curve, an example of which is shown in Fig. 50, is approximated using Eq. 7, the results shown in Eq. 8.

$$G(s) = \frac{120}{s^4 + 10s^3 + 50s^2 + 80s + 1} \quad \textbf{[Eq. 8]}$$

Matlab was then used to apply the Ziegler-Nichols method to this approximation of the Plant, however because the equation is simply an approximation the values had to be manually adjusted using results from a live sample. The final PID values are shown in Table 10.

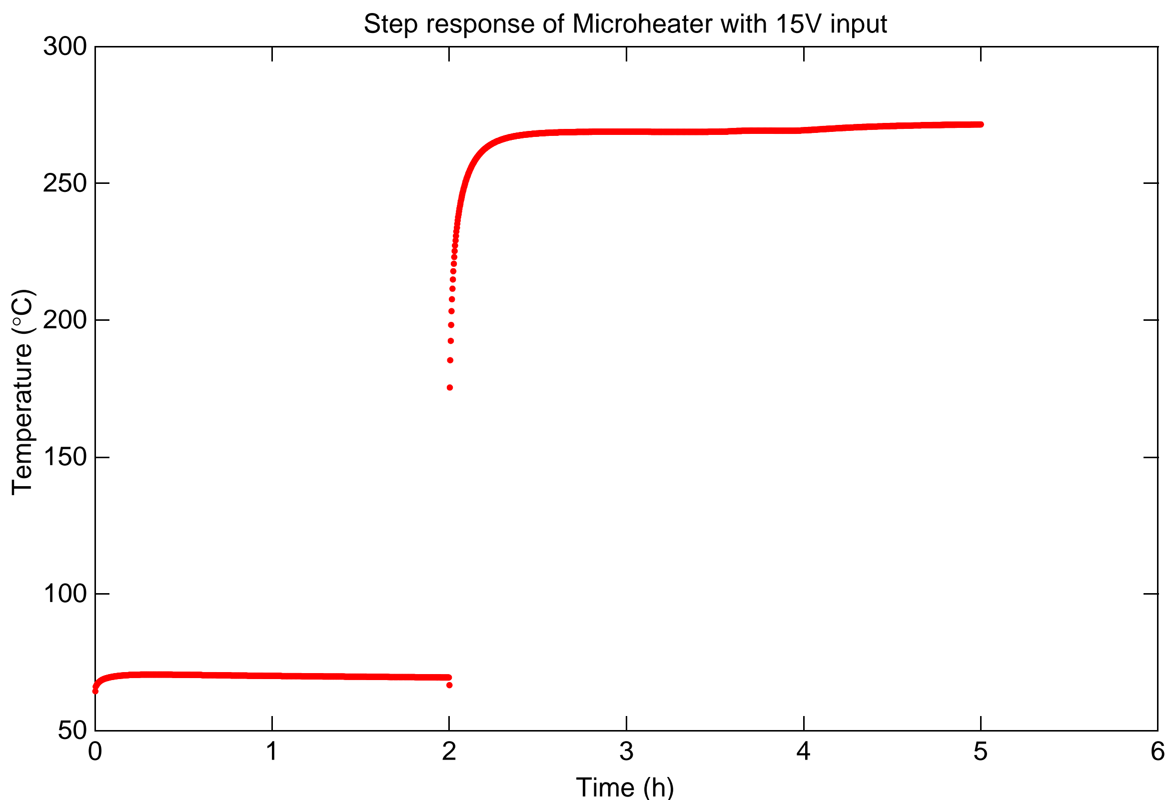

Fig. 50   Step response the of sample Q01’s microheater.

Table 10: PID values for the microheater

P	I	D
0.01	0.05	0.018

3.7 Testing Procedure (HTS)

The test bond is aged by cycling the heater repeatedly between a powered state and off state. For these experiments the heater is typically held at 250 ºC for 45 minutes and then transitioning to 15 minutes of no power during which the pad resistance measurements are taken, for 250 hours. The software can be programmed to cycle in any arbitrary pattern, such as a staircase heat profile, for any total experiment duration.

3.8 Pad Resistance

The pad resistance method uses a similar method as the contact resistance method, but instead of running the current and voltage paths through the ball bond, all measurements are done from lines attached to the corners of the bond pad. The electric field lines generated by the applied constant current fan out from the side where the majority of current is flowing, meaning that the voltage sensing points do not see the entire voltage differential across the pad, as seen in Fig. 51. Using the van der Pauw method [29] of deriving the square resistance of a proportionally larger, flat object using a four-wire measurement made from the corners, we can compensate for this mathematically.

The Van der Pauw equation (Eq. 9) uses the symmetry of the bond pad and taking $R_{AB,CD} = R_{BC,DA}$ due to the bonding pad being symmetric along the x and y-directions, it reduces the equation to a simpler form (Eq. 10).

$$\exp\left(-\pi\frac{R_{AB,CD}}{R_s}\right) + \exp\left(-\pi\frac{R_{BC,DA}}{R_s}\right) = 1 \qquad \textbf{[Eq. 9]}$$

$$Rs = \frac{\pi}{\ln 2}R \qquad \textbf{[Eq. 10]}$$

Therefore the actual pad resistance is approximately 4.5324 times greater than the measured pad resistance from any of the sides.

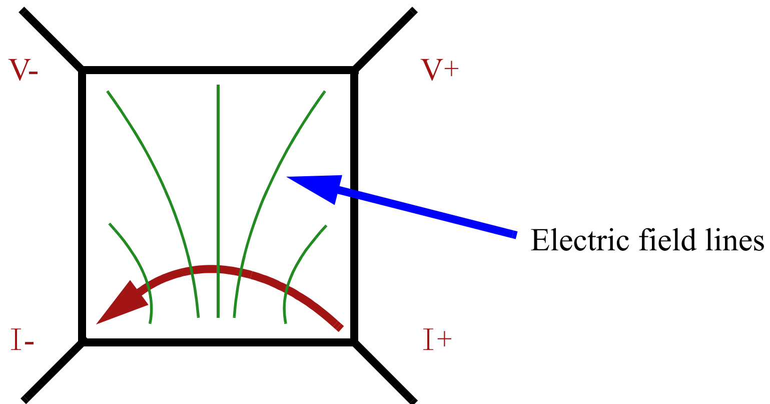

Fig. 51 Pad outline with isolines (thin lines) approximating electric field generated by the current (curved arrow indicates current direction) across the two bottom corners of bonding pad during 4-wire resistance measurement.

3.9 Microheater Post-Aging Drift

An experiment was run to determine the extent of the irreversible changes to the heater and RTD after VHTS, which would affect the actual temperature of the heater during operation if the characterizations of them change significantly. Sample Q03 was characterized and then heated at 300 ºC for 113 h before being characterized again. The resistance vs. temperature values before and after aging are shown in Table Eq. 11, along with the percentage differences. This means that based on the aging changes on the RTD, the actual and desired temperature can drift as much as 5% depending on the temperature, as seen in Fig. 52.

However, if both the RTD and heater are recalibrated the derived heater temperature (where we used the RTD temperature to determine the heater temperature), then the actual and reported tem-

Table 11: Before and after aging characterization of RTD and heater

	R = mT+b	Before	After	% diff
RTD	m [Ω/ºC]	0.1618	0.1761	-8.1
	b [Ω]	45.47	44.23	2.8
Heater	m [Ω/ºC]	0.1198	0.1316	-9.0
	b [Ω]	73.41	68.39	7.3

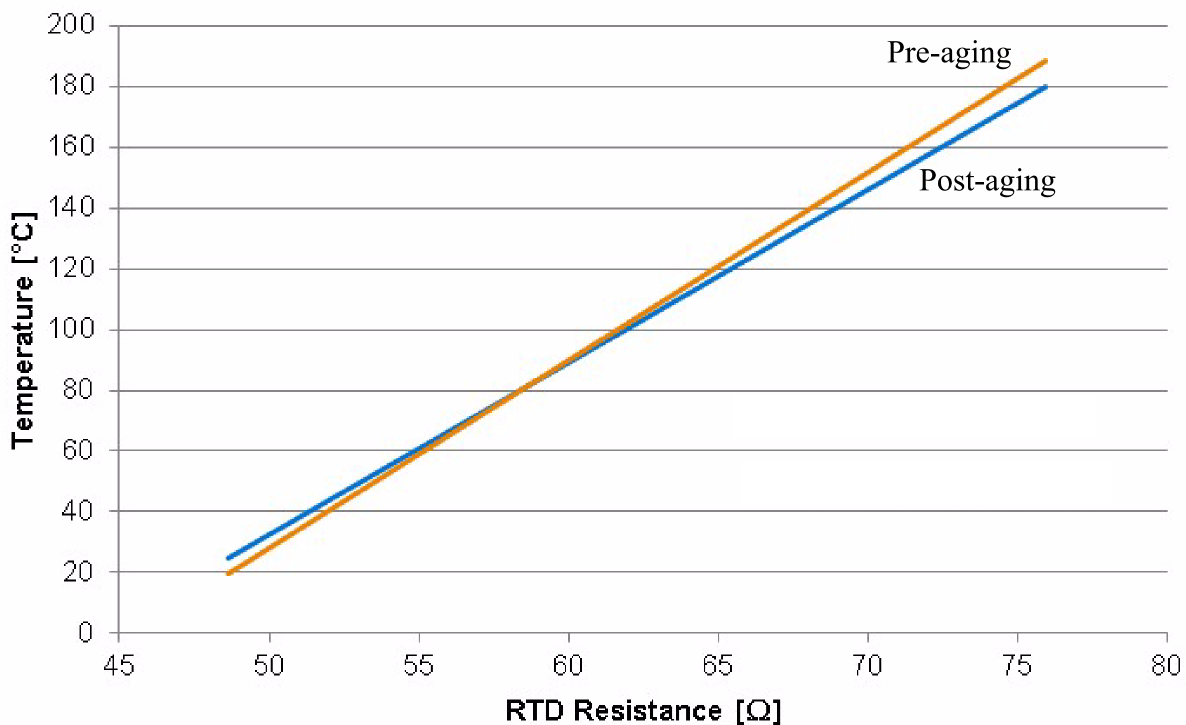

Fig. 52 Plot showing the linear fits of the actual temperature and reported temperature of the RTD, which are different due to irreversible changes from being heated by the microheater. The reported temperature uses pre-aging characterization data and the actual temperature uses post-aging characterization data.

peratures become more of a constant offset of approximately 12 ºC as seen in Fig. 53. This is because both the RTD and heater undergo similar irreversible changes as was seen in Table 11 where their slopes decreased but their intercepts increased.

3.10 Resistance Analysis

An Au ball bond using 25 µm wire was made on the microheater's test pad. An image of the bond is shown in Fig. 54 (a). The microheater was cycled in 1 h periods, 25±2 ºC for 15 min and then 250 ºC for 45 min, during the 150 h long experiment to age the ball bond. The pad resistance was ignored when the heater was in operation due to the large voltage gradient across the pad, which skewed current flow and voltage readings during the four-wire resistance measurements. During aging, the pad resistance values were averaged once per period when the temperature stabilized at 25 ºC, as shown in Fig. 55.

The first data point represents the pad resistance with no VHTS done to the test pad. While the calculated pad resistance of 20.6 mΩ matches with the observed empty pad resistance of 20.4 mΩ, the addition of the ball bond lowers the measured pad resistance to 18.6 mΩ due to the increase in conductive material. During the aging, the increase in resistance agrees with the fact that Au-Al IMC products have higher resistances than the base Au or Al metals, shown in Table 12 [16]. Four distinct phases can be seen during the aging of the ball bond, however the consumption of the surface of the pad's Al occurs during the first phase. The mechanism for the drop in resistance seen in phase 2 is not known, but a possible explanation is a change in IMC composition. Au-rich IMCs have higher resistance than Al-rich IMCs, so if the Au ball bond

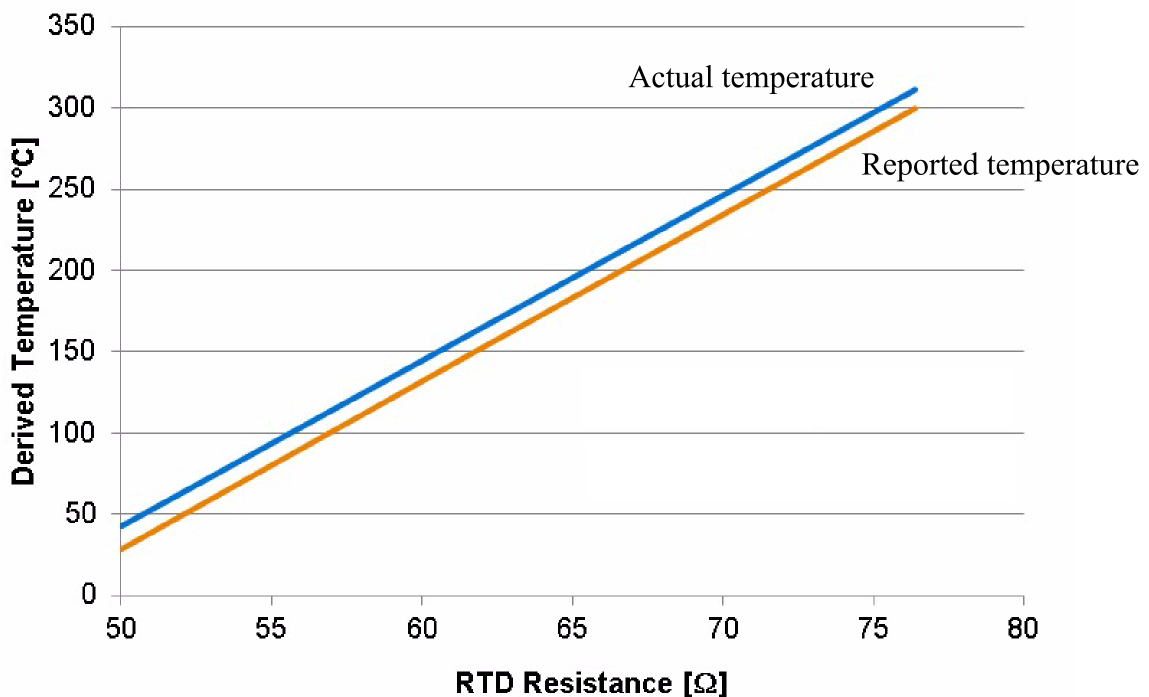

Fig. 53 Plot showing linear fits for the reported and actual derived temperatures for the micro-heater after aging. The reported temperature (orange) shows the derived temperature using characterized values before aging. The actual temperature (blue) shows the derived temperature after irreversible changes have occured, using the characterizations from after the aging experiment.

becomes isolated from the IMCs while they are still forming, due to voiding or oxide formation, then as they consume the remaining Al in the bonding pad they become Al-rich IMCs. The resistance increase seen in phase 3 can then be explained by these Al-rich IMCs becoming oxidized or further voiding occurring as the IMCs progress. During the 4th phase, the pad resistance does not increase as the pad has been completely consumed by IMC formation and becomes stabilized. and some IMC formation actually progresses along the signal lines for the pad resistance measurements as seen in Fig. 56.

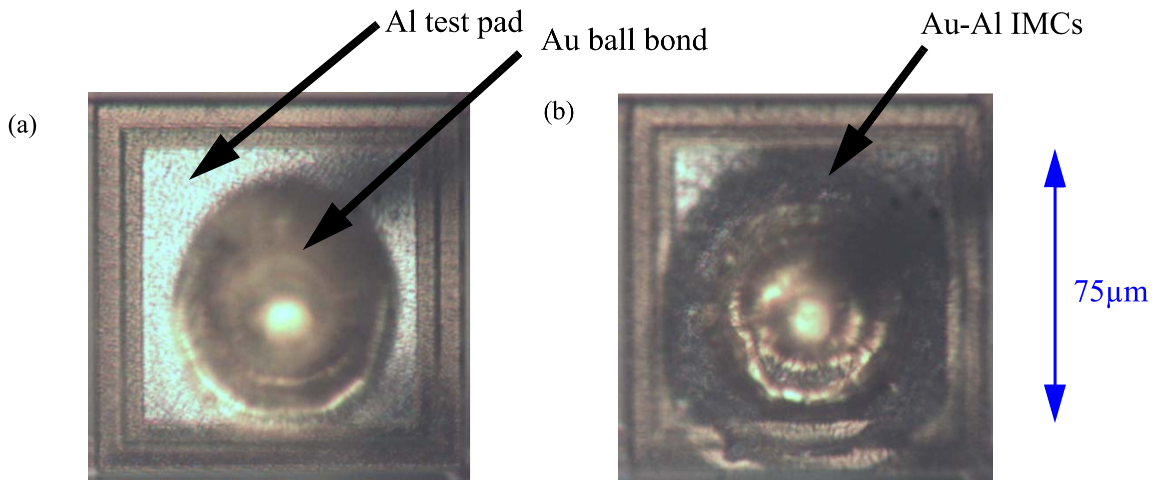

Fig. 54 Optical image of an Au ball bond on the microheater test pad before (a) and after (b) 24 h of aging.

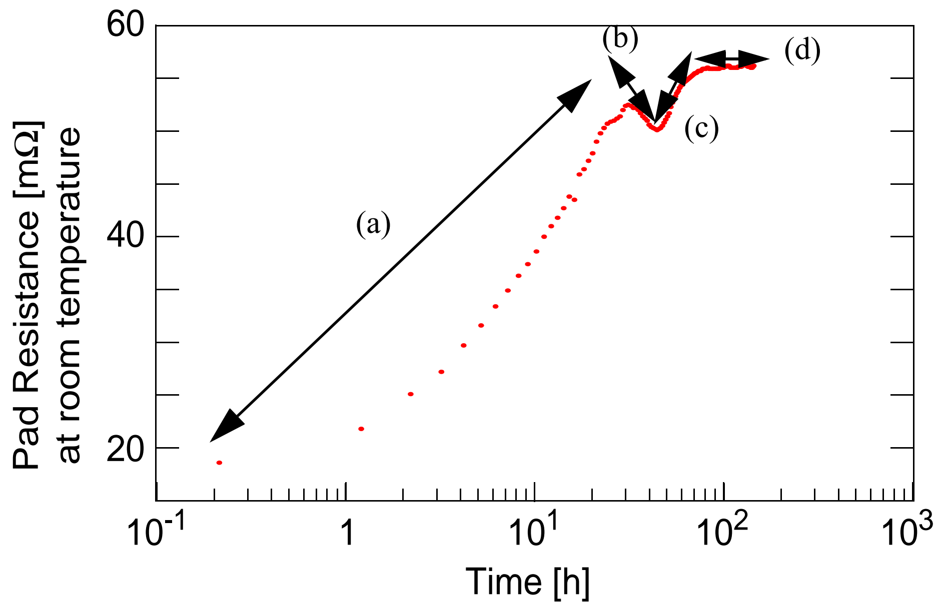

Fig. 55 Pad resistance of sample TC5 during a VHTS test. Four phases were identified, (a) phase 1 is when the pad's Al is consumed to form IMCs, (b) phase 2 has a decrease in resistance, (c) phase 3 sees an increase in resistance again, before (d) phase 4 the pad resistance stabilizes until electrical failure occurs.

Another sample where an Au double ball bond was aged for 120 h at 300 ºC, SEM images were also taken to show consumption of the pad surface by IMCs, as shown in Fig. 57. The pad resistance measurements failed after 150 h, when voltage could no longer be measured because of an open circuit occurring at one of the corner lines. The dark regions seen in image (c) correspond to the Au-rich IMCs as seen in image (b) which was taken using backscattering to give a very high contrast between Au-containing materials and Al or Si.

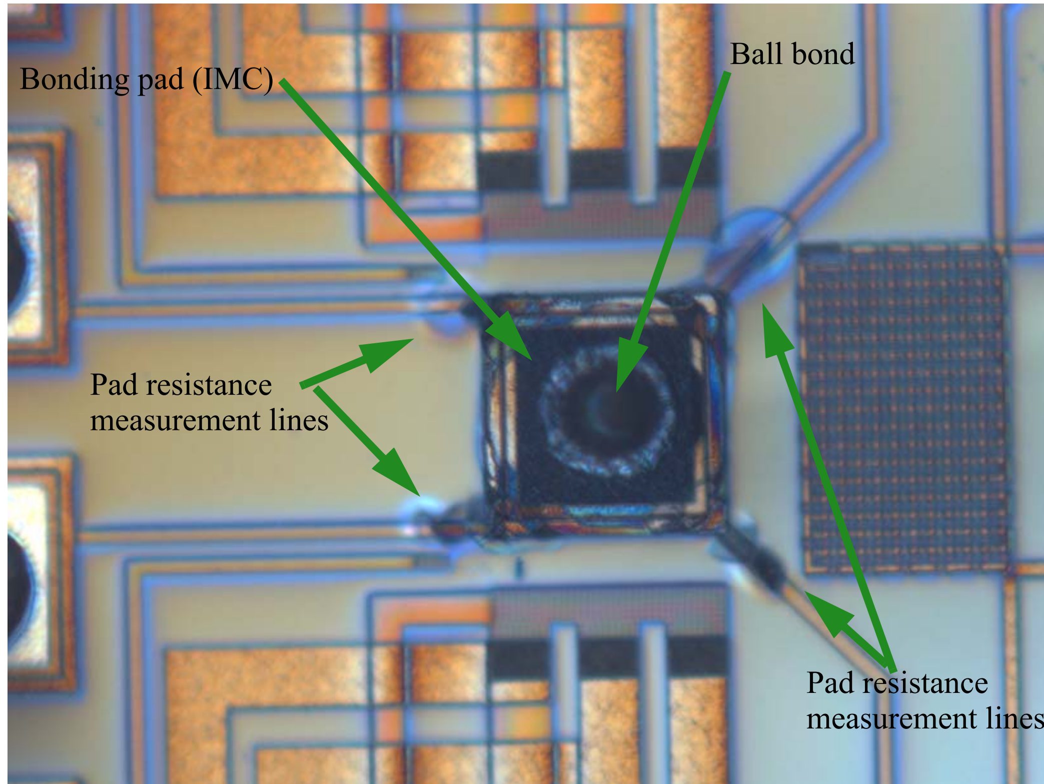

Fig. 56 Au ball bond after 150 h of VHTS. The bonding pad has been completely consumed and progression of Au-Al IMC formation is seen along the measurement lines of for the pad resistance measurement.

Table 12: Resistivities of Au, Al, and their common IMC products [16]

Material	Resistivity [Ωcm]
Au	2.3
Al	3.2
$AuAl_2$	7.9
AuAl	12.4
Au_2Al	13.1
Au_8Al_3	25.5
Au_4Al	37.5

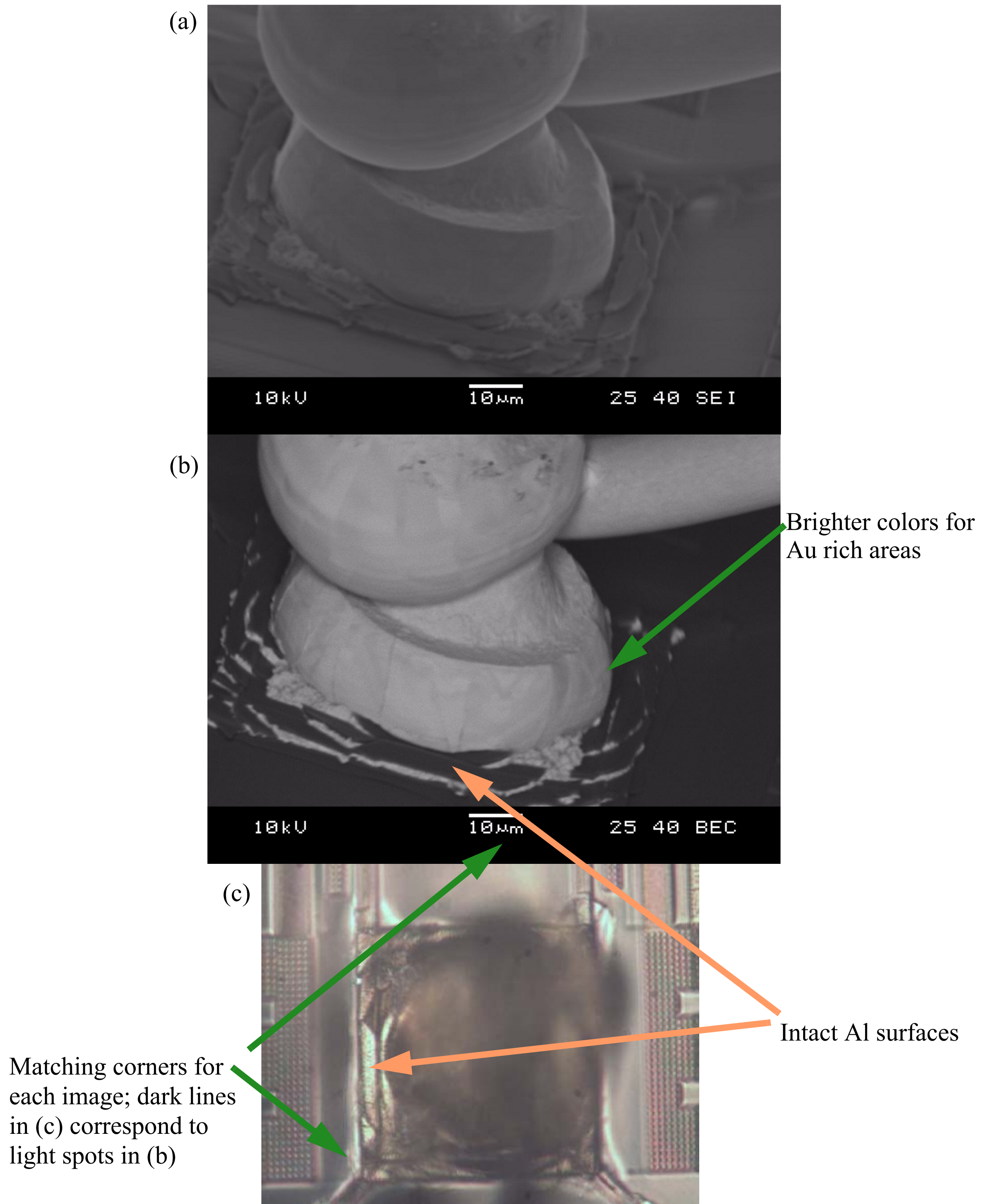

Fig. 57 Sample Q01 after 120 hours of aging. SEM images for (a) the surface shape, (b) back-scattering to highlight gold-rich areas are shown, and (c) the micrograph of the same test bond, seen from above.

4. Results of PM Chip Aging

In this experiment [30], several Pd coated Cu (PCC) wires and Au wires bonded to the PM chip were aged for four weeks at constant 200 ºC in a conventional oven. Occasionally the experiment was interrupted to correct for any software issues or to observe the samples. After the experiment, SEM images were taken of the samples to observe oxidation and aging effects on the ball bonds.

4.1 PCC Ball Bond Analysis

Micrographs of the ball bonds were taken before aging took place and then again after the experiment ended as oxidized Cu is much darker than Cu. Then the sample PCC bonds were observed under a scanning electron microscope to see the surface oxidation of both the ball bond and wire, if any. Finally, x-ray diffraction analysis (EDS) was used on a ball bond with both oxidized and non-oxidized areas to confirm how the presence of palladium prevented visible oxidation.

The oxidation almost completely covers the ball bond's surface, as seen in Fig. 58, where the darkened areas on the ball bond is oxidized Cu. The second set of images for the ball bonds post-aging are focused on the top and mid-sections of the ball bond to better show the texture differences and colors of the oxidized and non-oxidized areas. The lighter colored areas are not as oxidized due to the presence of Pd on the surface of the ball.

In Fig. 59, we can see the texture differences in the oxidized and non-oxidized areas of the ball bond, where the oxidized areas are fuzzy. EDS results in Fig. 60 show that the ball bond surface was predominantly copped and oxygen, with only patches of Pd found on the sample. No IMCs at the periphery of the Cu-Al interface were visible, however Al splash-off (Al flash) can be seen.

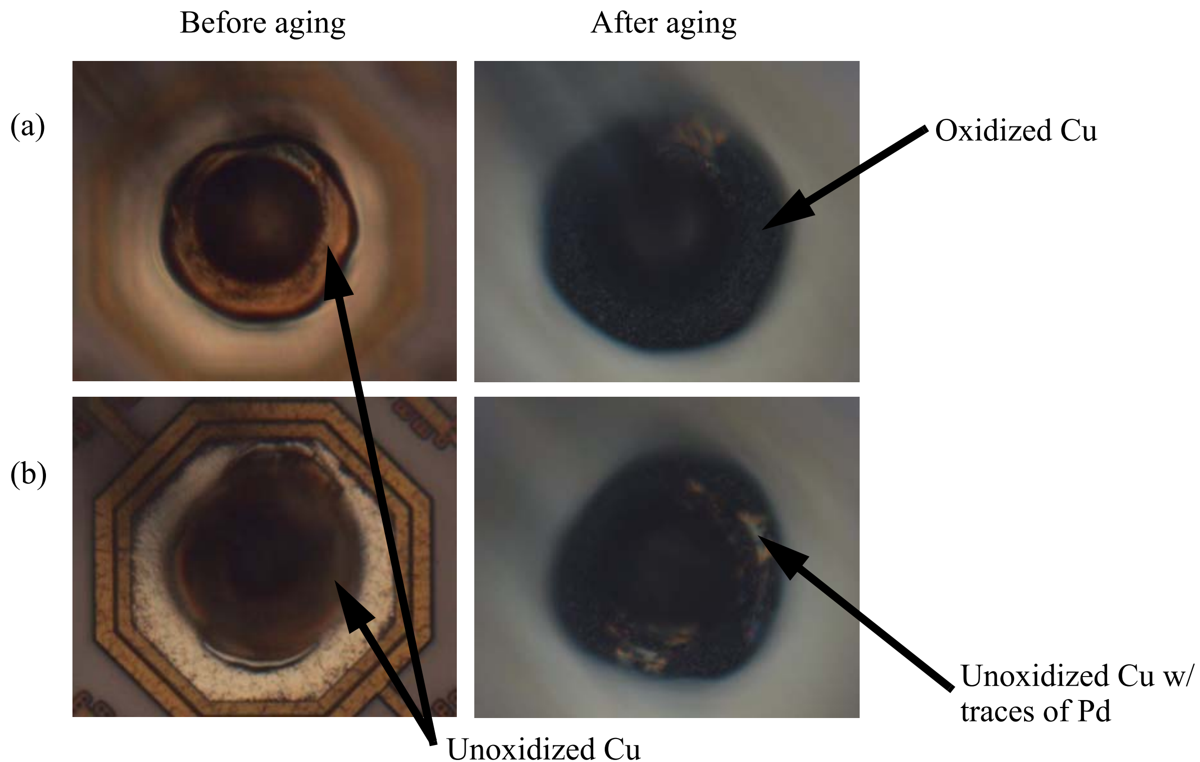

Fig. 58 Comparison of the PCC ball bond on pad 0 (a) and pad 4 (b) before and after aging.

This splash-off occurs because Cu is much harder than Au or Al and requires greater bonding forces than when joining Au to Al.

4.2 PCC Wire Analysis

From visual inspection, the wires were oxidizing despite the palladium coating, as seen in Fig. 61. Despite the presence of oxidation, the SEM image of the wire in Fig. 62 shows that the surface is smooth.

4.3 Gold Ball Bonds

Gold ball bonds degraded much faster than the PCC bonds, with intermetallics forming between the ball bond and the Al pad, shown in Fig. 63. EDS analysis showed that the composition of the IMCs (at the surface) was 94.6% Au and 5.4% Al. This extension of the IMC formation from underneath the ball bond, directly Au-Al interface, to the surrounding bonding pad correspond to the growth of IMCs seen in the VHTS aging with the microheater.

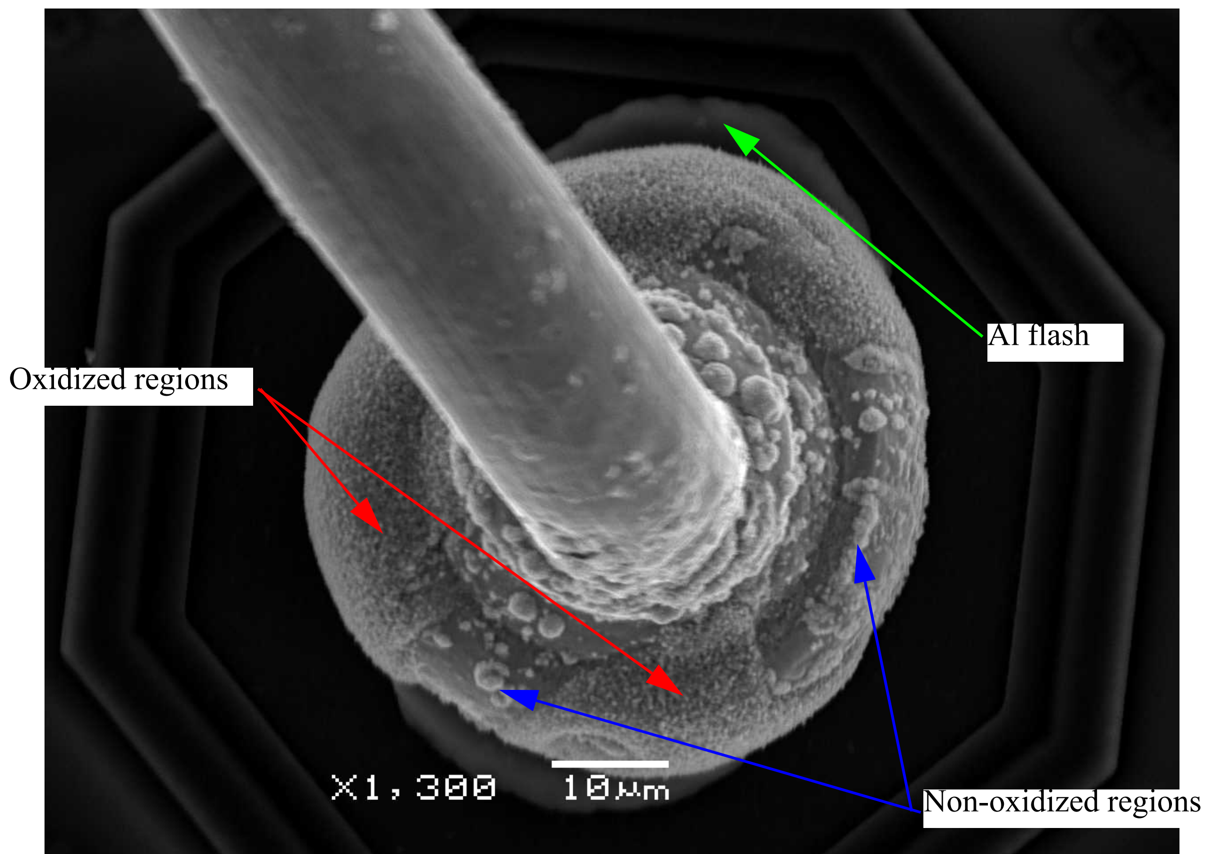

Fig. 59 Scanning electron microscope image of a PCC ball bond after HTS.

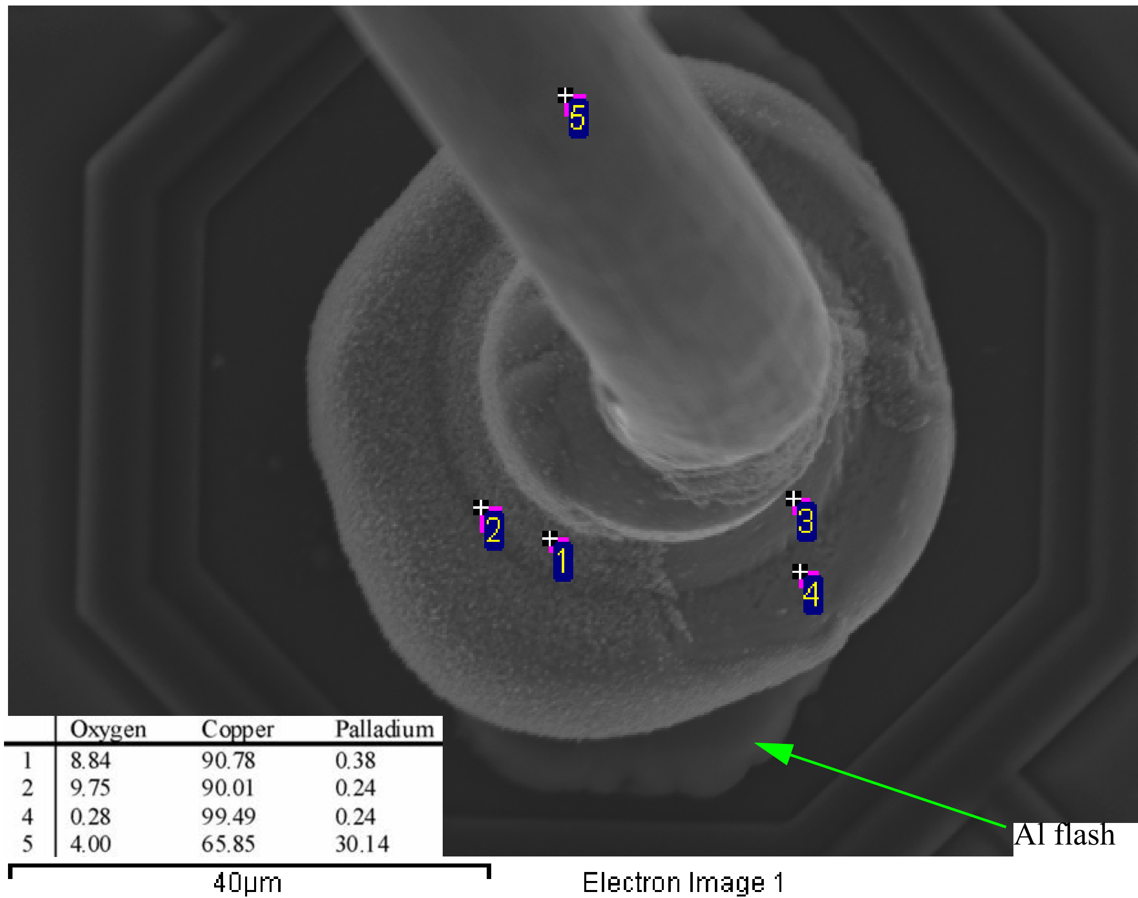

	Oxygen	Copper	Palladium
1	8.84	90.78	0.38
2	9.75	90.01	0.24
4	0.28	99.49	0.24
5	4.00	65.85	30.14

Fig. 60 EDS analysis showing the oxygen, copper, and palladium concentrations on a PCC ball bond and the wire.

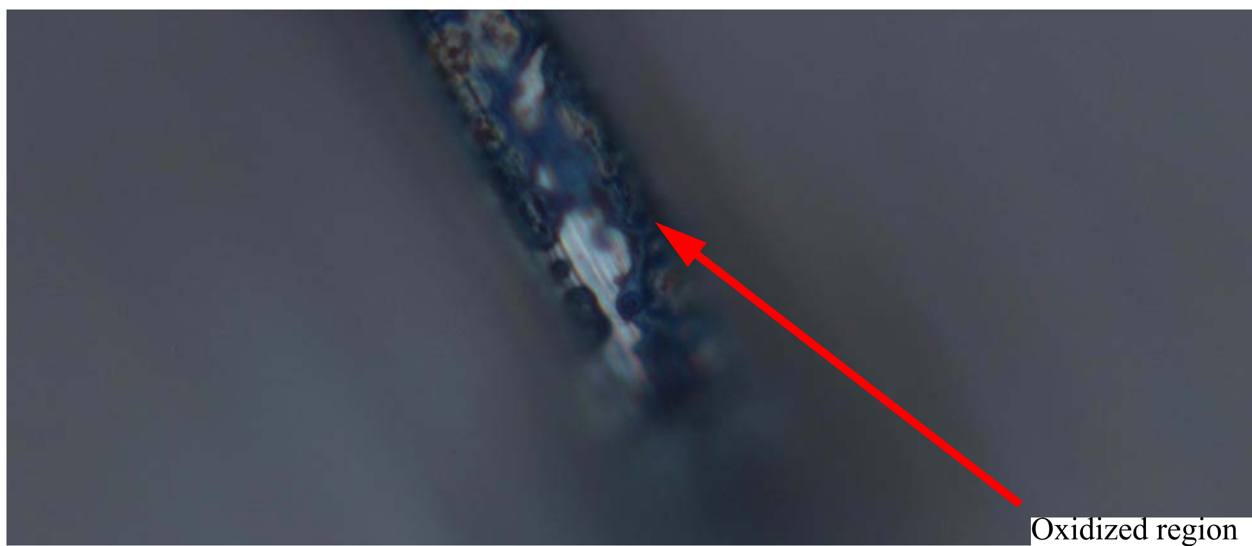

Fig. 61 Micrograph of the surface of PCC wire near the ball bond, after aging.

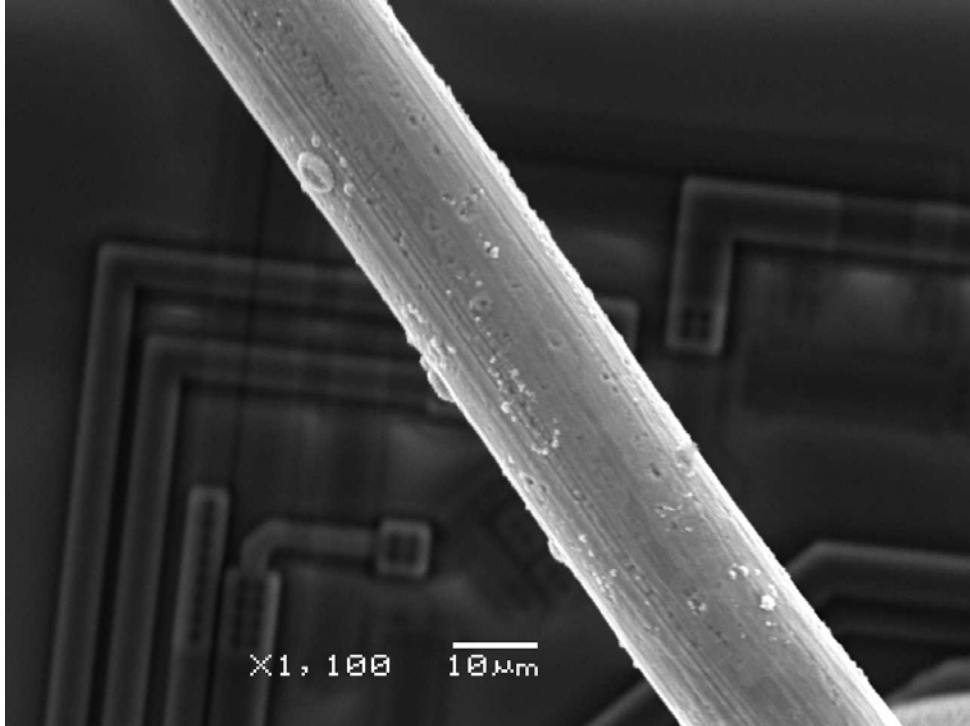

Fig. 62 SEM image of PCC wire after HTS.

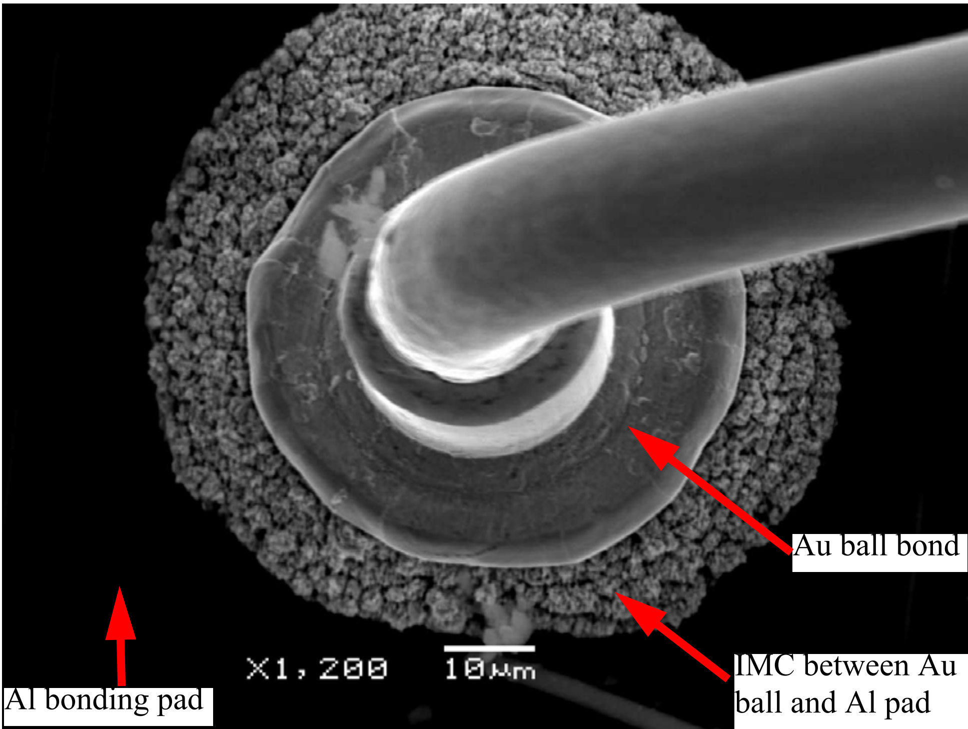

Fig. 63 Gold ball bond after high temperature aging.

5. Conclusions and Outlook

Using the MUS chip, the ability to take in-situ pad resistance measurements was proven. Measurements can be automated with a computer to be taken real-time and continuously throughout the duration of the experiment to give a life-time plot of the test bond. Pad resistance measurements have the advantage of showing the electrical integrity of the ball bond joint and does not require specialized probes or double ball bonds to make the measurement, as the leads for current and voltage are at the corners of the bond pad.

The microheater was able to provide a method of highly accelerating the aging of a test bond by raising the test bond's temperature to up to 300 ºC for more than 100 h while not significantly aging nearby I/O bonds. The pad resistance experiments using the microheater were done at lower temperatures as Au forms IMCs with Al readily. The operation of the microheater was done using an external power supply controlled by a computer which ramped or kept the temperature steady successfully with a calibrated PID controller. The drift of the microheater was shown to result in a 5% difference between the actual temperature and the recorded temperature due to irreversible changes in the microheater's RTD and the heater itself.

With the development of novel wire bonds, which provide much more stable joints with Al bonding pads, it becomes more difficult to age samples because the sensing and power (I/O) bonds must be made with known bonding materials such as gold. This results in a chance that the test bonds outlive the I/O bonds. Localizing the heat to only the test bonds means that the I/O bonds age at a much slower rate and aggressive aging techniques can be used for these novel wire bonds that require high temperatures to undergo IMC formation or oxidation in realistic time frames, as temperature increases metal diffusion and chemical reaction rates.

These results show that pad resistance measurements can correlate to bond reliability allowing for a new method of non-destructive bond aging analysis. The formation of IMCs and Kirkendall voiding cause increases in the resistance of the pad-ball interface which thus increase the resistance of the pad.

The practical application of these studies is to allow for a test-on-a-chip device where once provided with a power supply and measurement equipment, a series of microchips can analyze wire bonds with different bonding parameters non-destructively and in real-time. Non-destructive, real-time testing means fewer samples are needed as a single sample can report throughout its life time instead of having portions of the sample set removed at regular intervals to be cross-sectioned. This also reduces the need for large ovens to heat samples in, as only a power supply is needed to age the sample.

Future steps would be to continue testing of the other microchip designs discussed in this thesis, such as underpad sensors, localized temperature sensors for bonding power measurements, and the new iteration of the microheater, which also includes localized stress sensors.

References

1. Prasad, S. K.; “Advanced Wirebond Interconnection Technology”, Kluwer Academic Publishers, 2004, Boston.
2. Shah, A., M. Mayer, Y. Zhou, J. Persic, and J. T. Moon. "Optimization of ultrasound and bond force to reduce pad stress in thermosonic Cu ball bonding." In Electronics Packaging Technology Conference, 2009. EPTC'09. 11th, pp. 10-15. IEEE, 2009.
3. I. Itabashi, “Gold Use in Electronics: Bonding Wire”, LBMA Precious Metals Conference 2004, Shanghai, pp. 77-80, 2004.
4. Yoo, K.-A., Uhm, C., Kwon, T.-J., Cho, J.-S., Moon, J.-T., “Reliability study of low cost alternative Ag bonding wire with various bond pad materials”, (2009) Proceedings of the Electronic Packaging Technology Conference, EPTC, art. no. 5416424, pp. 851-857.
5. Cho, Jong-Soo, Hee-Suk Jeong, Jeong-Tak Moon, Se-Jin Yoo, Jae-Seok Seo, Seung-Mi Lee, Seung-Weon Ha, Eun-Kyu Her, Suk-Hoon Kang, and Kyu-Hwan Oh. "Thermal reliability & IMC behavior of low cost alternative Au-Ag-Pd wire bonds to Al metallization." In Electronic Components and Technology Conference, 2009. ECTC 2009. 59th, pp. 1569-1573. IEEE, 2009.
6. Qin, I., A. Shah, C. Huynh, M. Meyer, M. Mayer, and Y. Zhou. "Effect of process parameters on pad damage during Au and Cu ball bonding processes." In Electronics Packaging Technology Conference, 2009. EPTC'09. 11th, pp. 573-578. IEEE, 2009.
7. Fan, Chonglun, Joseph A. Abys, and Alan Blair. "Gold and aluminum wire bonding to palladium surface finishes." Circuit World 25, no. 3 (1999): 23-27.
8. Y. Huang, “Study of Au Ball Bond Mechanism and Reliability on Pd/Ni/Cu Substrate”, University of Waterloo, 2009.
9. Hang, C. J., C. Q. Wang, M. Mayer, Y. H. Tian, Y. Zhou, and H. H. Wang. "Growth behavior of Cu/Al intermetallic compounds and cracks in copper ball bonds during isothermal aging." Microelectronics reliability 48, no. 3 (2008): 416-424.
10. Hund, Tom D. "Thermosonic gold-ball bond accelerated life test." In Electronic Components and Technology Conference, 1990.., 40th, pp. 436-441. IEEE, 1990.
11. Rabaey, J.M., Chandrakasan, A., Nikolic, B., "Digital Integrated Circuits A Design Perspective Second Edition", Pearson Education Inc, 2003.
12. England, Luke, and Tom Jiang. "Reliability of Cu wire bonding to Al metallization." In Electronic Components and Technology Conference, 2007. ECTC'07. Proceedings. 57th, pp. 1604-1613. IEEE, 2007.
13. M.J. McCracken, “Assessing Au-Al Wire Bond Reliability Using Integrated Stress Sensors”, University of Waterloo, 2010.
14. Kim, Hyoung-Joon, Joo Yeon Lee, Kyung-Wook Paik, Kwang-Won Koh, Jinhee Won, Sihyun Choe, Jin Lee, Jung-Tak Moon, and Yong-Jin Park. "Effects of Cu/Al intermetallic compound (IMC) on copper wire and aluminum pad bondability." Components and Packaging Technologies, IEEE Transactions on 26, no. 2 (2003): 367-374.
15. Mayer, M. "Non-destructive monitoring of Au ball bond stress during high-temperature aging." In Electronic Components and Technology Conference, 2008. ECTC 2008. 58th, pp. 1762-1768. IEEE, 2008.

16. Harman, G., “Wire Bonding in Microelectronics Third Edition”, McGraw-Hill, 2010.
17. Huang, Y., H. J. Kim, M. McCracken, G. Viswanathan, F. Pon, M. Mayer, and Y. N. Zhou. "Effect of Pd Surface Roughness on the Bonding Process and High Temperature Reliability of Au Ball Bonds." Journal of Electronic Materials 40, no. 6 (2011): 1444-1451.
18. Senturia, S. D., "Microsystem Design", Springer, 2001.
19. Phatthanakun, R., P. Deekla, W. Pummara, C. Sriphung, C. Pantong, and N. Chomnawang. "Fabrication and control of thin-film aluminum microheater and nickel temperature sensor." In Electrical Engineering/Electronics, Computer, Telecommunications and Information Technology (ECTI-CON), 2011 8th International Conference on, pp. 14-17. IEEE, 2011.
20. Kimura, Mitsuteru, and Kazuhiro Komatsuzaki. "Microheater made of heavily boron doped single crystal silicon beam." In MRS Proceedings, vol. 276, no. 1. Cambridge University Press, 1992.
21. C. Rossi, PT Boyer, and D. Esteve, “Realization and performance of thin SiO2/Si3Nx membrane for microheater applications”, Sensors Actuators, A 64, pp. 241–245, 1998.
22. Crary, Selden B. "Thermal management of integrated microsensors." Sensors and actuators 12, no. 4 (1987): 303-312.
23. Cadence®, Cadence Design Systems, Inc., http://www.cadence.com/products/cic/Pages/default.aspx.
24. Mayer, Michael, Oliver Paul, Daniel Bolliger, and Henry Baltes. "Integrated temperature microsensors for characterization and optimization of thermosonic ball bonding process." Components and Packaging Technologies, IEEE Transactions on 23, no. 2 (2000): 393-398.
25. Whitaker, Jerry C., “Microelectronics 2nd Edition”, CRC Press, 2009.
26. AMI Seniconductor, “Electrical Parameters CMOS 0.7µm - C07MA and C07MD”, Revision 14, April 2005.
27. Lambropoulos, John C., M. R. Jolly, C. A. Amsden, S. E. Gilman, M. J. Sinicropi, D. Diakomihalis, and S. D. Jacobs. "Thermal conductivity of dielectric thin films." Journal of applied physics 66, no. 9 (1989): 4230-4242.
28. “Low Level Measurements Handbook 6th Edition”, Keithley Instruments Inc, 2004.
29. LJ van der Pauw, “Method for measuring specific resistivity and Hall effect of discs of arbitrary shape”, Philips Ret Rep., 13 (1958) 1 - 9.
30. Kim, Samuel, “PCC Aging Micrographs and Analysis”, University of Waterloo CAMJ Internal Report, 2011.

Appendix A: Matlab scripts for operation of microheater

For temperature characterization, use "temp_characterization.m"

```
%{
Author: Samuel Kim
Purpose:
Heat sample in an external oven
Uses 2 multimeters for the RTD voltage (4 wire) and the PSU
current (for more accurate power calculations)
Also measures the local Pt100 to examine the conductive and
radiative heat effects on the minioven
%}

close all;
clear;

sample = 'TC6'
sampleName = [sample '_temp_chara_bonded_2'];
mkdir(sampleName);
nowDate = datestr(now);

spVoltages = [2  ];%  here you set the voltages (V)
spTimes =    [120 ] * 60;%  here you set the times [m]
% save time profile data to file
tprf=[spVoltages(:) spTimes(:)/3600];
save([sampleName '\temp_profile.txt'],'tprf','-ascii');
tempChanged = 1;
target_temp = spVoltages(1);
spVoltage = spVoltages(1);
timeDuration = sum(spTimes); % [s] (total time duration)

% Constant current source values
RTDCurrent = 1; %mA
PadCurrent = 1;%mA

 %Connecting to multimeter and accessing it
RTDMeter = gpib('agilent', 7, 26);
heaterVoltage = gpib('agilent', 7, 25);
padVoltage = gpib('agilent', 7, 22);
Ammeter = gpib('agilent', 7, 24);

ccs = gpib('agilent',7,23);
psu = gpib('agilent',7,5);

% MCC
loadlibrary c:\mcc\cbw32.dll c:\mcc\c\cbw.h alias mccFuncLib;
boardNum=0;
chanNum=3;
tempScale=0;
portNum = 10;
options=0;
AIVal=0;
AIPtr=libpointer('singlePtr',AIVal);

aitemp = analoginput('mcc',0);
%addchannel(ai,[0 1 2 3  ]);
addchannel(aitemp,[0]);
set(aitemp,'SampleRate',100);
%sr=get(aitemp,'SampleRate');
set(aitemp,'SamplesPerTrigger',50);

ccs_counter = 1;
temp = 1;
figure(1);

% POWER SUPPLY FOR MINIOVEN

%Initialize executable names for power supply automation
Voltage = 0;

% put voltage to zero
fopen(psu);
fprintf(psu,['SOUR:VOLT ' num2str(Voltage)]);
fprintf(psu,'OUTP ON');
fclose(psu);

tic;
curTime = toc;

while (curTime < timeDuration)   % MEASUREMENT LOOP  %%%%%%%%%%%%%%%%
    if ccs_counter == 1
        fopen(ccs);
        fprintf(ccs,'SOUR:FUNC:MODE CURR');
        fprintf(ccs,'SOUR:CURR 1E-3');
        fprintf(ccs,'OUTP ON');
        fclose(ccs);
        ccs_counter = 0;
    else
        fopen(ccs);
        fprintf(ccs,'SOUR:FUNC:MODE CURR');
```

```
        fprintf(ccs,'SOUR:CURR -1E-3');
        fprintf(ccs,'OUTP ON');
        fclose(ccs);
        ccs_counter = 1;
    end;
    pause(2);

    deltaT = curTime;
    curTime = toc;
    deltaT = curTime - deltaT;

    %RTD
    fopen(RTDMeter);
    fprintf(RTDMeter, 'READ?');
    tempRTD = str2double(fscanf(RTDMeter)); %    tempRTD = str2double(fscanf(RTDMeter));
    fclose(RTDMeter);

    fopen(Ammeter);
    fprintf(Ammeter, 'READ?');
    tempCurrent = str2double(fscanf(Ammeter));
    fclose(Ammeter);

    fopen(heaterVoltage);
    fprintf(heaterVoltage, 'READ?');
    tempHeater = str2double(fscanf(heaterVoltage));
    fclose(heaterVoltage);

    fopen(padVoltage);
    fprintf(padVoltage, 'READ?');
    tempPad = str2double(fscanf(padVoltage));
    fclose(padVoltage);

    start(aitemp);
    wait(aitemp,9);
    [tempresults,tempt] = getdata(aitemp);
    %     tempresults = 0;
    curTemp = mean(tempresults) * 120;

    subplot(2,2,1);
    plot(curTime/3600,tempRTD,'.'); hold on
    title(['RTD Resistance']);
    xlabel('Time [s]');
    ylabel('Resistance [Ohms]');

    subplot(2,2,2);
    plot(curTime/3600,tempHeater,'.'); hold on
    title(['Heater Voltage']);
    xlabel('Time [s]');
    ylabel('Voltage [V]');

    subplot(2,2,3);
    plot(curTime/3600,tempCurrent,'.'); hold on
    title(['Heater Current']);
    xlabel('Time [s]');
    ylabel('Current [Amperes]');

    subplot(2,2,4);
    plot(curTime/3600,curTemp,'.'); hold on
    title(['Pt100 Temp']);
    xlabel('Time [s]');
    ylabel('Temp [\circC]');


    j1=1;
    while (j1 < length(spTimes)) && (sum(spTimes(1:j1))<curTime);
        j1=j1+1;
    end
    if j1 > length(spTimes)
        j1 = length(spTimes);
    end;

 Voltage = spVoltages(j1);
    if (Voltage > 0 && Voltage < 20);
        %dos([SetVoltageExe '-v' int2str(Voltage)]);
        fopen(psu);
        fprintf(psu,['SOUR:VOLT ' num2str(Voltage)]);
        %fprintf(psu,'OUTP ON');
        fclose(psu);
    end;
    if (Voltage >= 20);
        %dos([SetVoltageExe '-v20000']);
        Voltage = 20;
        fopen(psu);
        fprintf(psu,['SOUR:VOLT ' num2str(Voltage)]);
        %fprintf(psu,'OUTP ON');
        fclose(psu);
    end;
    if Voltage <= 0;
        %dos([SetVoltageExe '-v0']);
        Voltage = 0;
        fopen(psu);
        fprintf(psu,['SOUR:VOLT ' num2str(Voltage)]);
```

```
        %fprintf(psu,'OUTP ON');
        fclose(psu);
    end;

    %time, R_RTD, T_RTD, extrapolated temp (curTemp), voltage,
    %Rc current, V_heater, Rc
    fid = fopen([sampleName,'\', 'results.txt'],'a');
    fprintf(fid,[num2str(curTime) ' ' num2str(tempRTD) ' ' num2str(Voltage) ' ' num2str(tem-
pHeater) ' ' num2str(tempCurrent) ' ' num2str(tempPad) ' ' num2str(curTemp) '\r\n']);  %' '
num2str(curTemp)
    fclose (fid);
end

% dos([SetVoltageExe '-off -v' int2str(0)]);
% dos([SetVoltageExe '-release ']);
Voltage = 0;
fopen(psu);
fprintf(psu,['SOUR:VOLT ' num2str(Voltage)]);
fprintf(psu,'OUTP OFF');
fclose(psu);
fopen(ccs);
fprintf(ccs,'OUTP OFF');
fclose(ccs);
```

For power characterization, use “heater_setvoltage_v02.m”

```
%{
Author: Samuel Kim
Purpose:
We are going to ramp the microheater voltage in user specified
increments
The hold times for each step can be assigned as well
Uses 2 multimeters for the RTD voltage (4 wire) and the PSU
current (for more accurate power calculations)
Also measures the local Pt100 to examine the conductive and
radiative heat effects on the minioven
%}

close all;
clear;

sample = 'TC3'
sampleName = [sample '_temp_chara_bonded_1'];
mkdir(sampleName);
nowDate = datestr(now);

spVoltages = [2  4  6  8  10 12];%  here you set the voltages (V)
spTimes =    [30 30 30 30 30 30 ] * 60;%  here you set the times [m] * 60 = [s]
% save time profile data to file
tprf=[spVoltages(:) spTimes(:)/3600];
save([sampleName '\temp_profile.txt'],'tprf','-ascii');
tempChanged = 1;
target_temp = spVoltages(1);
spVoltage = spVoltages(1);
timeDuration = sum(spTimes); % [s] (total time duration)

% Constant current source values
RTDCurrent = 1; %mA
PadCurrent = 1;%mA

 %Connecting to multimeter and accessing it
RTDMeter = gpib('agilent', 7, 26);
heaterVoltage = gpib('agilent', 7, 25);
padVoltage = gpib('agilent', 7, 22);
Ammeter = gpib('agilent', 7, 24);

ccs = gpib('agilent',7,23);
psu = gpib('agilent',7,5);

ccs_counter = 1;
temp = 1;
figure(1);

% POWER SUPPLY FOR MINIOVEN

%Initialize executable names for power supply automation
Voltage = 0;

% put voltage to zero
fopen(psu);
fprintf(psu,['SOUR:VOLT ' num2str(Voltage)]);
fprintf(psu,'OUTP ON');
fclose(psu);

tic;
curTime = toc;

while (curTime < timeDuration)   % MEASUREMENT LOOP  %%%%%%%%%%%%%%%%%
    if ccs_counter == 1
        fopen(ccs);
        fprintf(ccs,'SOUR:FUNC:MODE CURR');
```

```
        fprintf(ccs,'SOUR:CURR 1E-3');
        fprintf(ccs,'OUTP ON');
        fclose(ccs);
        ccs_counter = 0;
    else
        fopen(ccs);
        fprintf(ccs,'SOUR:FUNC:MODE CURR');
        fprintf(ccs,'SOUR:CURR -1E-3');
        fprintf(ccs,'OUTP ON');
        fclose(ccs);
        ccs_counter = 1;
    end;
    pause(2);

    deltaT = curTime;
    curTime = toc;
    deltaT = curTime - deltaT;

    %RTD
    fopen(RTDMeter);
    fprintf(RTDMeter, 'READ?');
    tempRTD = str2double(fscanf(RTDMeter)); %    tempRTD = str2double(fscanf(RTDMeter));
    fclose(RTDMeter);

    fopen(Ammeter);
    fprintf(Ammeter, 'READ?');
    tempCurrent = str2double(fscanf(Ammeter));
    fclose(Ammeter);

    fopen(heaterVoltage);
    fprintf(heaterVoltage, 'READ?');
    tempHeater = str2double(fscanf(heaterVoltage));
    fclose(heaterVoltage);

    fopen(padVoltage);
    fprintf(padVoltage, 'READ?');
    tempPad = str2double(fscanf(padVoltage));
    fclose(padVoltage);

    subplot(2,2,1);
    plot(curTime/3600,tempRTD,'.'); hold on
    title(['RTD Resistance']);
    xlabel('Time [s]');
    ylabel('Resistance [Ohms]');

    subplot(2,2,2);
    plot(curTime/3600,tempHeater,'.'); hold on
    title(['Heater Voltage']);
    xlabel('Time [s]');
    ylabel('Voltage [V]');

    subplot(2,2,3);
    plot(curTime/3600,tempCurrent,'.'); hold on
    title(['Heater Current']);
    xlabel('Time [s]');
    ylabel('Current [Amperes]');


    j1=1;
    while (j1 < length(spTimes)) && (sum(spTimes(1:j1))<curTime);
        j1=j1+1;
    end
    if j1 > length(spTimes)
        j1 = length(spTimes);
    end;

    Voltage = spVoltages(j1);

    if (Voltage > 0 && Voltage < 20);
        fopen(psu);
        fprintf(psu,['SOUR:VOLT ' num2str(Voltage)]);
        fclose(psu);
    end;
    if (Voltage >= 20);
        Voltage = 20;
        fopen(psu);
        fprintf(psu,['SOUR:VOLT ' num2str(Voltage)]);
        fclose(psu);
    end;
    if Voltage <= 0;
        Voltage = 0;
        fopen(psu);
        fprintf(psu,['SOUR:VOLT ' num2str(Voltage)]);
        fclose(psu);
    end;

    %time, R_RTD, T_RTD, extrapolated temp (curTemp), voltage,
    %Rc current, V_heater, Rc
    fid = fopen([sampleName,'\', 'results.txt'],'a');
    fprintf(fid,[num2str(curTime) ' ' num2str(tempRTD) ' ' num2str(Voltage) ' ' num2str(tem-
pHeater) ' ' num2str(tempCurrent) ' ' num2str(tempPad) '\r\n']);  %' ' num2str(curTemp)
    fclose (fid);
```

```
end

Voltage = 0;
fopen(psu);
fprintf(psu,['SOUR:VOLT ' num2str(Voltage)]);
fprintf(psu,'OUTP OFF');
fclose(psu);
fopen(ccs);
fprintf(ccs,'OUTP OFF');
fclose(ccs);
```

For operation of the microchip in an experiment, use “heater_longterm_cycling.m”

```
%{
Author: Samuel Kim
Date:   22SEP2011
Purpose:
We are going to ramp the microheater voltage in user specified
increments until the temperature if found to exceed a
certain limit which can be set
The hold times for each step can be assigned as well

Uses 2 multimeters for the RTD voltage (4 wire) and the PSU
current (for more accurate power calculations)

Also measures the local Pt100 to examine the conductive and
radiative heat effects on the minioven
%}

close all;
clear;

sample = 'TC5'
sampleName = [sample '_250deg_run_75h'];
mkdir(sampleName);
nowDate = datestr(now);

mDer = 8.808;
bDer = -424;

% PID Controller
K = [0.01 0.05 0.018];
Linear = 0;
Integral = 0;%1.4999e+004;
Derivative = 0;%-0.2090;

totalTime = 75 *3600; %hours
spTemps = [0 250];%  here you set the temperatures (degC)
spTimes =    [0.25 0.75] * 3600;%  here you set the times [h]
% save time profile data to file
tprf=[spTemps(:) spTimes(:)/3600];
save([sampleName '\temp_profile.txt'],'tprf','-ascii');
tempChanged = 1;
target_temp = spTemps(1);
%timeDuration = sum(spTimes); % [s] (total time duration)

% Constant current source values
RTDCurrent = 1; %mA

 %Connecting to multimeter and accessing it
RTDMeter = gpib('agilent', 7, 26);
heaterVoltage = gpib('agilent', 7, 25);
padVoltage = gpib('agilent', 7, 22);
Ammeter = gpib('agilent', 7, 24);

ccs = gpib('agilent',7,23);
psu = gpib('agilent',7,5);

ccs_counter = 1;
temp = 1;
tempPad = 0;
figure(1);

dataArrayCurrentRow = 1;
dataArrayRows = 2000;

% POWER SUPPLY FOR MINIOVEN
Voltage = 0;

% put voltage to zero
fopen(psu);
fprintf(psu,['SOUR:VOLT ' num2str(Voltage)]);
fprintf(psu,'OUTP ON');
fclose(psu);

tic;
curTime = toc;

while (curTime < totalTime)   % MEASUREMENT LOOP  %%%%%%%%%%%%%%%%
```

```
    newDataRow = [ ];%used with visualization and line writing

    if ccs_counter == 1
        fopen(ccs);
        fprintf(ccs,'SOUR:FUNC:MODE CURR');
        fprintf(ccs,'SOUR:CURR 1E-3');
        fprintf(ccs,'OUTP ON');
        fclose(ccs);
        ccs_counter = 0;
    else
        fopen(ccs);
        fprintf(ccs,'SOUR:FUNC:MODE CURR');
        fprintf(ccs,'SOUR:CURR -1E-3');
        fprintf(ccs,'OUTP ON');
        fclose(ccs);
        ccs_counter = 1;
    end;
    pause(2);

    deltaT = curTime;
    curTime = toc;
    deltaT = curTime - deltaT;

    %RTD measurements with three multimeters
    %RTD
    fopen(RTDMeter);
    fprintf(RTDMeter, 'READ?');
    tempRTD = str2double(fscanf(RTDMeter));
    fclose(RTDMeter);
    tempRTD = tempRTD*(1000/RTDCurrent);
    curTemp = tempRTD*mDer + bDer;

    fopen(Ammeter);
    fprintf(Ammeter, 'READ?');
    tempCurrent = str2double(fscanf(Ammeter));
    fclose(Ammeter);

    fopen(heaterVoltage);
    fprintf(heaterVoltage, 'READ?');
    tempHeater = str2double(fscanf(heaterVoltage));
    fclose(heaterVoltage);

    prevtempPad = tempPad;
    fopen(padVoltage);
    fprintf(padVoltage, 'READ?');
    tempPad = str2double(fscanf(padVoltage));
    fclose(padVoltage);
    tempPad = tempPad*(1000/RTDCurrent);

    j1=1;
    while (j1 < length(spTimes)) && (sum(spTimes(1:j1))<(mod(curTime, sum(spTimes))));
        j1=j1+1;
    end
    if j1 > length(spTimes)
        j1 = length(spTimes);
    end;
    target_temp = spTemps(j1);

    if (target_temp == 0)
        Linear = 0;
        Integral = 0;%1.4999e+004;
        Derivative = 0;%-0.2090;
        Voltage = 0;
    else
        prevError = Linear;
        Linear = target_temp - curTemp;
        Derivative = (Linear - prevError)/deltaT;
        Integral = Integral + (Linear + prevError)*deltaT/2;

        Voltage = Linear*K(1) + Integral*K(2) + Derivative*K(3);
    end;

    if (Voltage > 0 && Voltage < 25);
        fopen(psu);
        fprintf(psu,['SOUR:VOLT ' num2str(Voltage)]);
        fclose(psu);
    end;
    if (Voltage >= 25);
        Voltage = 25;
        fopen(psu);
        fprintf(psu,['SOUR:VOLT ' num2str(Voltage)]);
        fclose(psu);
    end;
    if Voltage <= 0;
        Voltage = 0;
        fopen(psu);
        fprintf(psu,['SOUR:VOLT ' num2str(Voltage)]);
        fclose(psu);
    end;

    newDataRow = [curTime tempRTD (tempRTD*mDer + bDer) Voltage tempHeater tempCurrent tempPad (pi/
log(2))*(abs(tempPad)+abs(prevtempPad))/2];% tempCurrent
```

```
    if dataArrayCurrentRow == 1
        dataArray = [newDataRow];
    end;
    if dataArrayCurrentRow >= dataArrayRows
        dataArray = [dataArray(2:dataArrayRows,:); newDataRow];
    end;
    if dataArrayCurrentRow < dataArrayRows
        dataArray = [dataArray; newDataRow];
        dataArrayCurrentRow = dataArrayCurrentRow + 1;
    end;
    if dataArrayCurrentRow > dataArrayRows
        dataArrayCurrentRow = dataArrayRows;
    end;

    clf;
    subplot(2,2,1);
    plot(dataArray(:,1)/3600,dataArray(:,3),'.'); %hold on
    title(['Extrapolated Temperature']);
    xlabel('Time [h]');
    ylabel('Temperature [\circC]');

    subplot(2,2,2);
    plot(dataArray(:,1)/3600,dataArray(:,5),'.'); %hold on
    title(['Heater Voltage']);
    xlabel('Time [h]');
    ylabel('Voltage [V]');

    subplot(2,2,3);
    plot(dataArray(:,1)/3600,dataArray(:,6),'.'); %hold on
    title(['Heater Current']);
    xlabel('Time [h]');
    ylabel('Current [A]');

    subplot(2,2,4);
    plot(dataArray(:,1)/3600,dataArray(:,8)*1000,'.'); %hold on
    title(['Pad Resistance']);
    xlabel('Time [h]');
    ylabel('Resistance [m\Omega]');

    %time, R_RTD, T_RTD, extrapolated temp (curTemp), voltage,
    %Rc current, V_heater, Rc
    fid = fopen([sampleName,'\', 'results.txt'],'a');
    fprintf(fid,[num2str(curTime) ' ' num2str(tempRTD) ' ' num2str(tempRTD * mDer + bDer) ' '
num2str(curTemp) ' ' num2str(Voltage) ' ' num2str(tempHeater) ' ' num2str(tempCurrent) ' '
num2str(tempPad) ' ' num2str((pi/log(2))*(abs(tempPad)+abs(prevtempPad))/2) '\r\n']);  %
    fclose (fid);
end

Voltage = 0;
fopen(psu);
fprintf(psu,['SOUR:VOLT ' num2str(Voltage)]);
fprintf(psu,'OUTP OFF');
fclose(psu);
fopen(ccs);
fprintf(ccs,'OUTP OFF');
fclose(ccs);
```

Appendix B: PM Chip bonding diagram

Bonding diagram for the PM chip using the CSB02803
28-pin CERDIP.

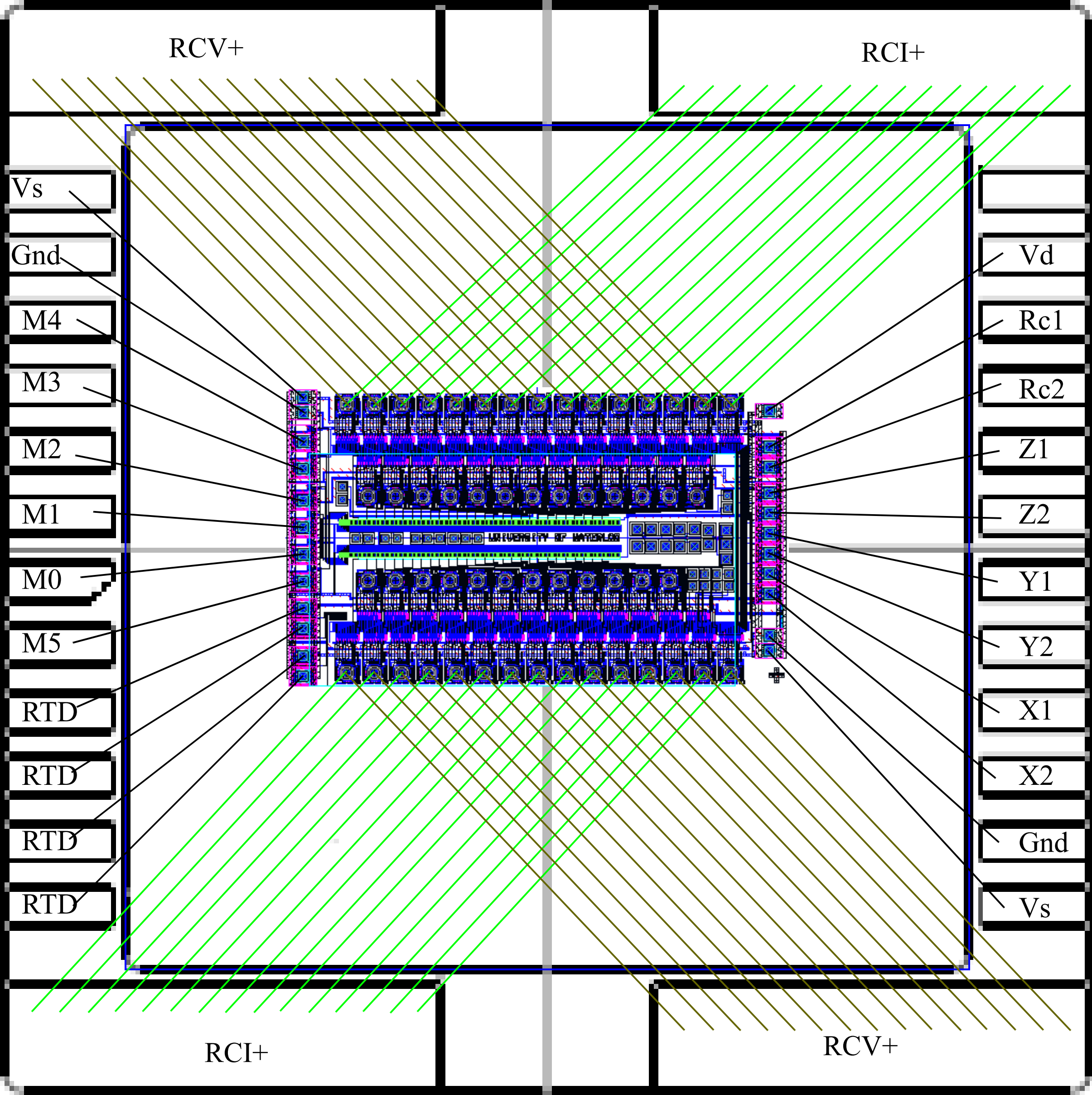

Appendix C: Bonding diagram for PM chip v2

Bonding diagram using the CSB02803 28-pin CERDIP.

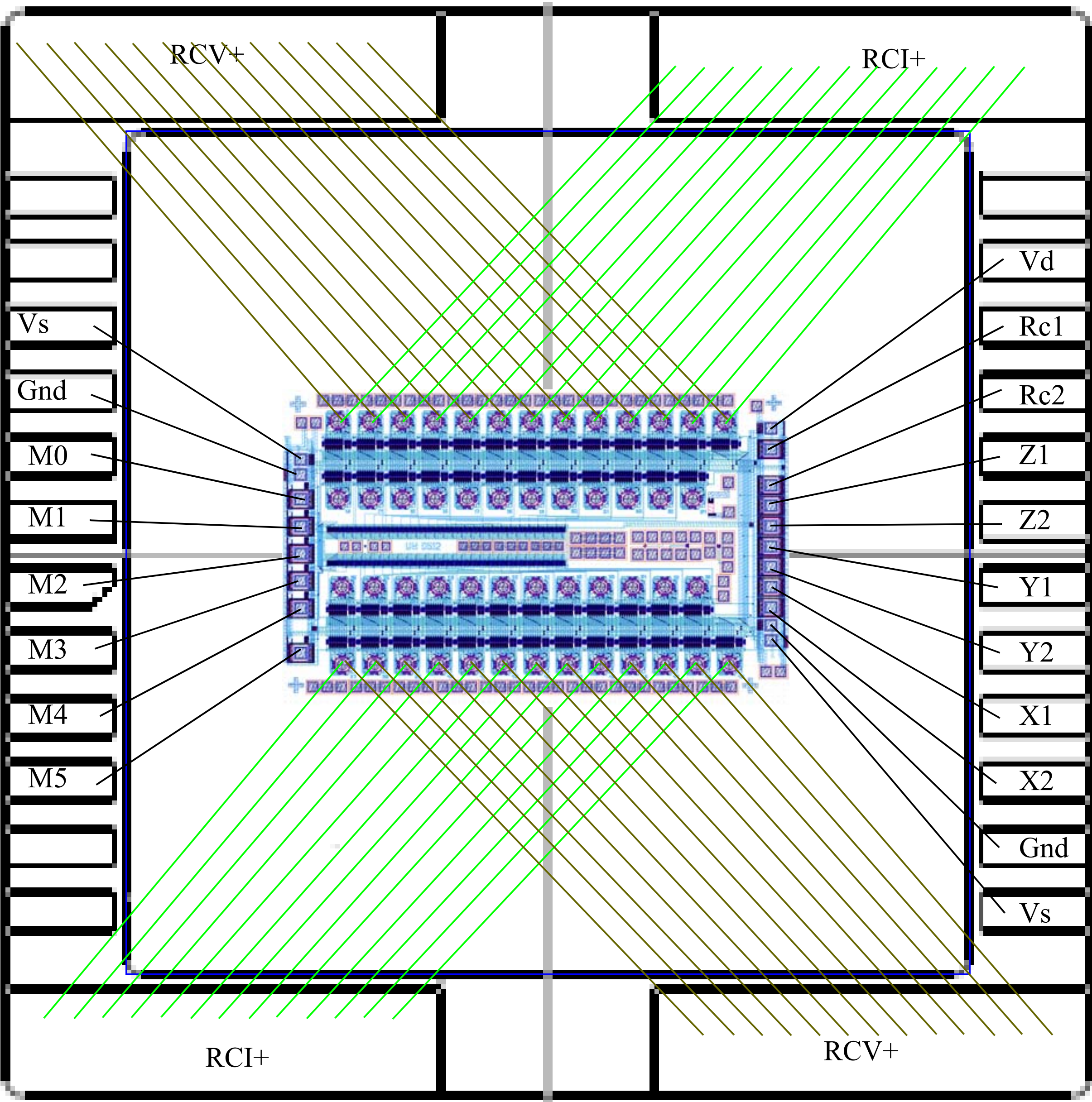

Appendix D: Bonding diagrams for thick-wire microheater chip

Bonding diagram using the CSB02803 28-pin CERDIP.

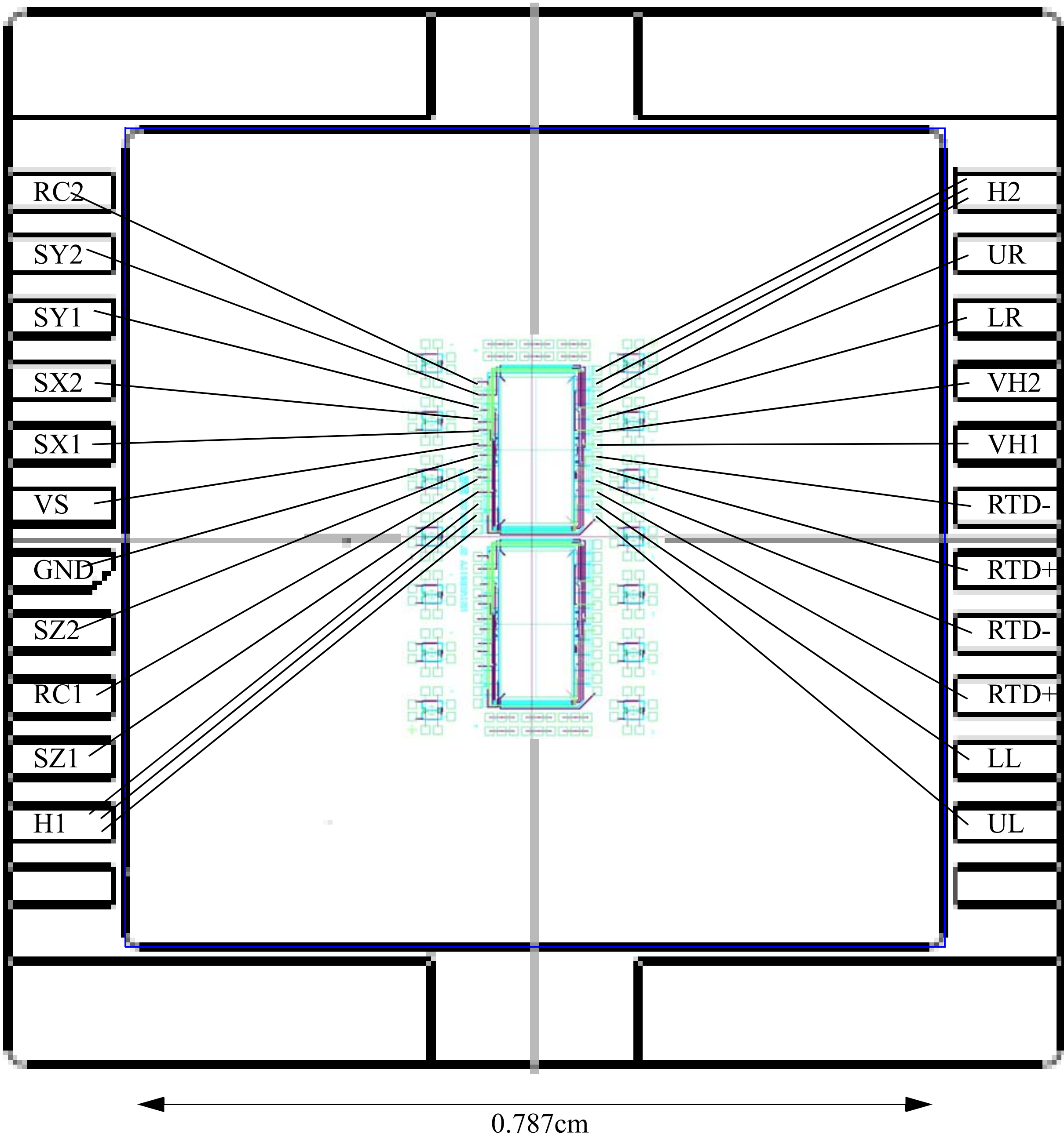

Bonding diagram using the SB02806 28-pin CERDIP

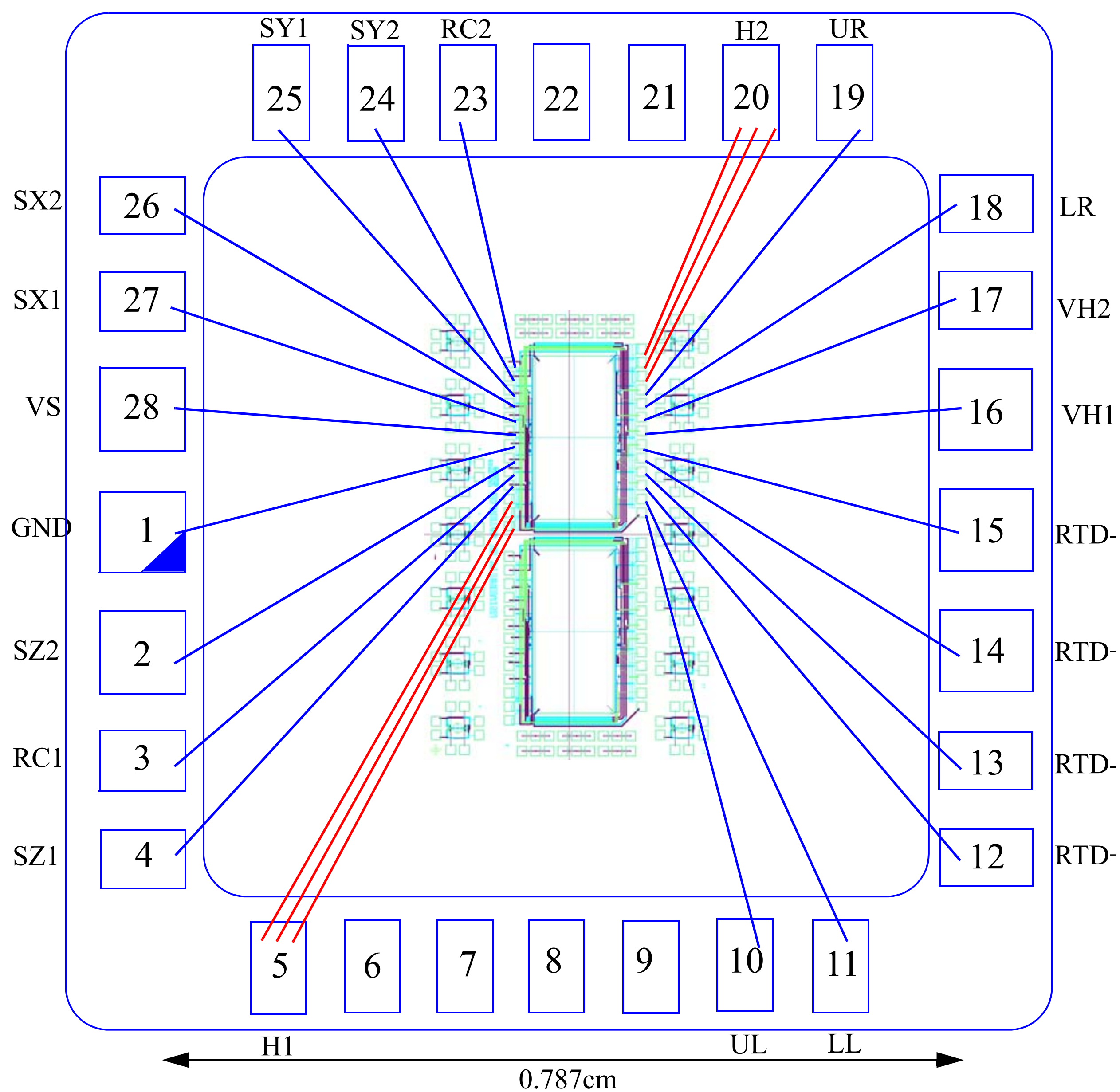

The meaning of each connection is shown in the table below.

Table 13: Pad and purposes for thick-wire microheater chip

Pad	Purpose	Pad	Purpose	Pad	Purpose	Pad	Purpose
H1	Underpad heater power	SZ1	Z sensor	RC1	Pad contact resistance	SZ2	Z sensor
GND	Sensor ground	VS	Sensor supply	SX1	X sensor	SX2	X sensor
SY1	Y sensor	SY2	Y sensor	RC2	Pad contact resistance	UL	Upper-left pad voltage line
LL	Lower-left pad votlage line	RTD+	Two connec-tions for current and voltage	RTD-	Two connec-tions for current and voltage	VH1	Voltage of northern edge of the pad
VH2	Voltage of the southern edge of the pad	LR	Lower-right pad voltage line	UR	Upper-right pad voltage line	H2	Underpad heater power

Appendix E: Bonding diagrams for the MUS chip

Bonding diagram 1 for RTD test pads (structure 1) using
the CSB02803 28-pin CERDIP

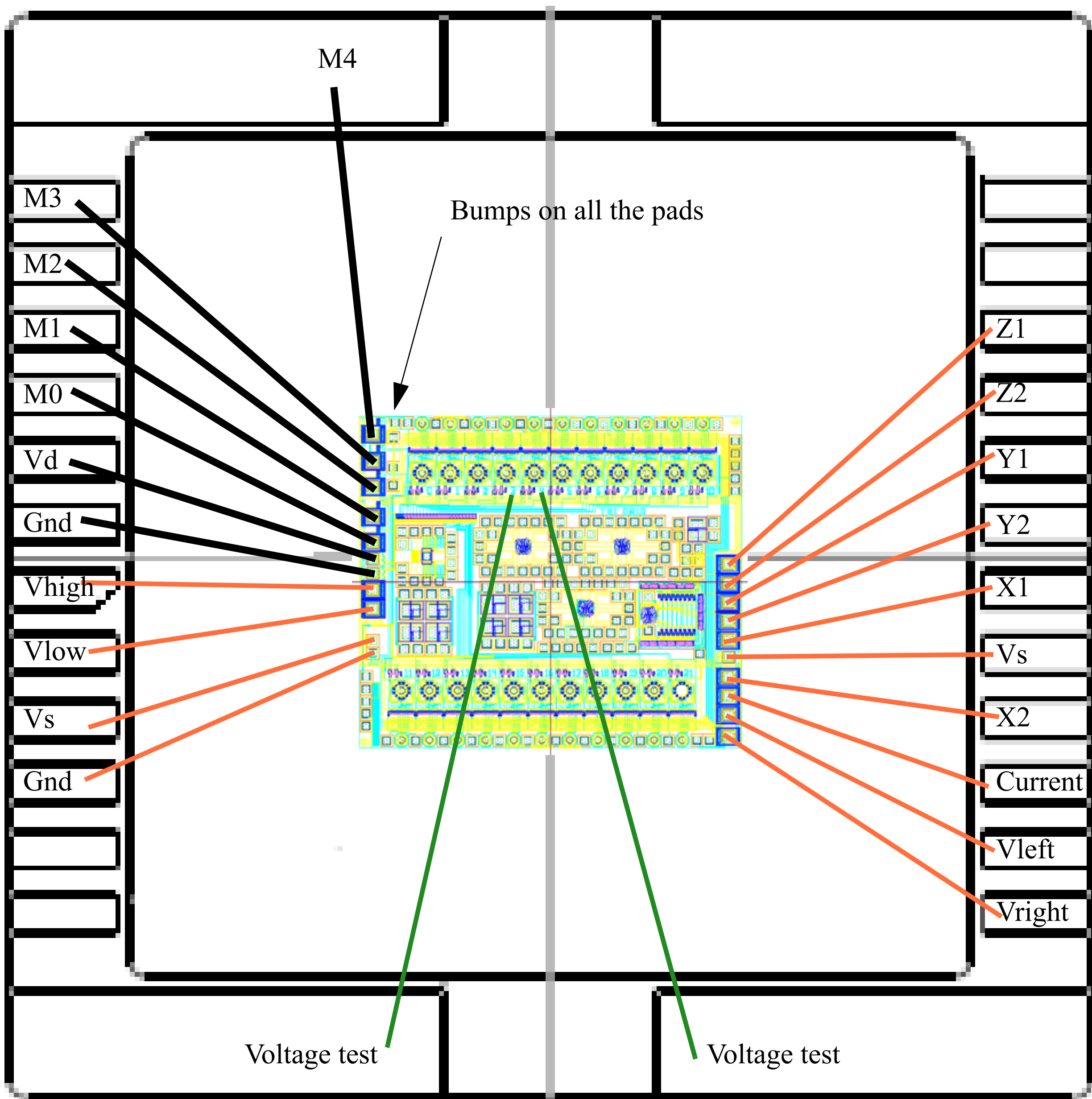

Bonding diagram 2 for using both structure 3 and structure 2 simultaneously with the SB02806 28-pin CERDIP. Pads are labelled with their corresponding channel names from Chapter 2.

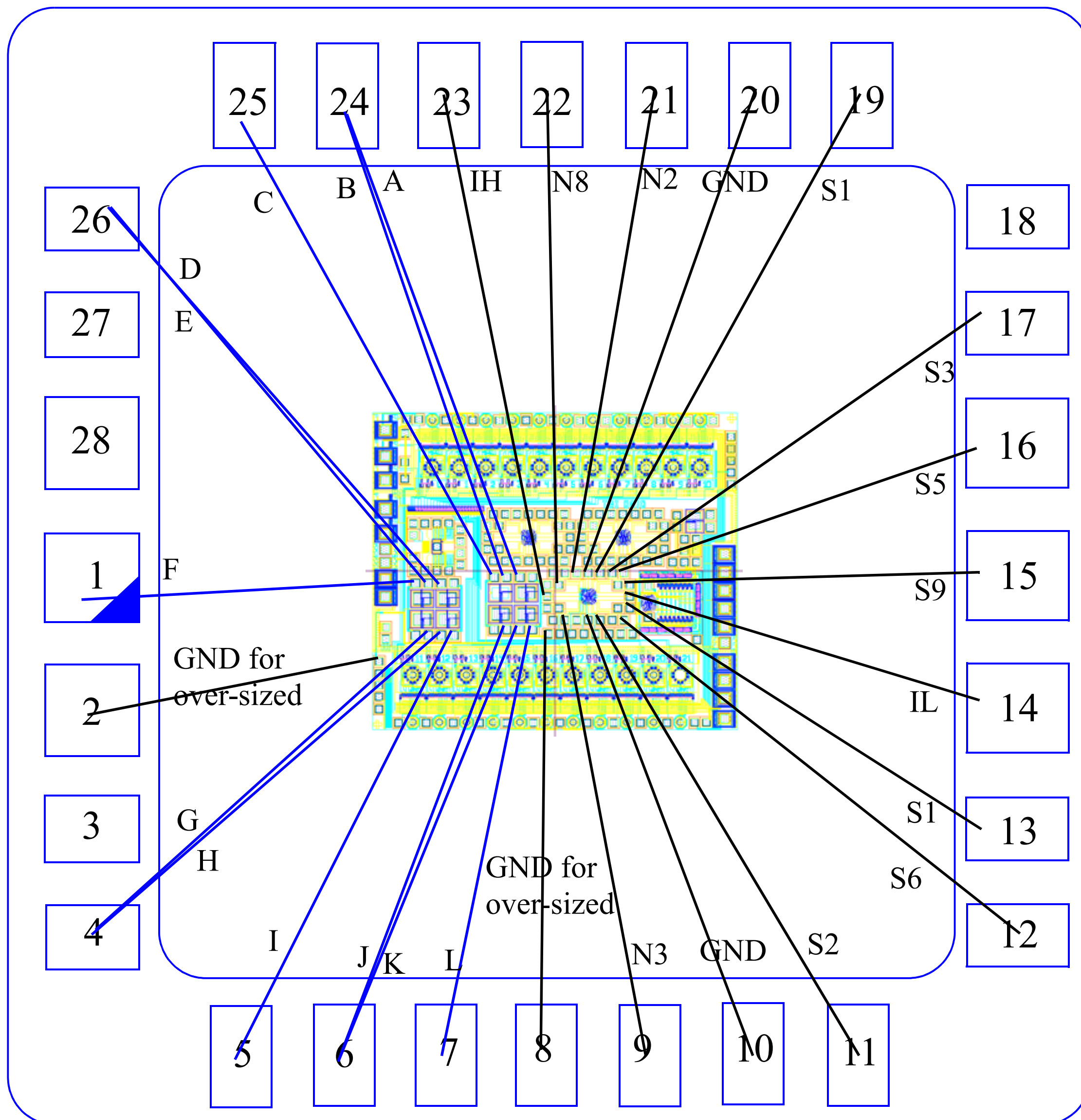

Bonding diagram 3 for structure 4, the microheater, using the SB02806 28-pin CERDIP. The V+ and V- pads are for powering the heater and the VH+/- pads are for measuring the voltage across the heater.

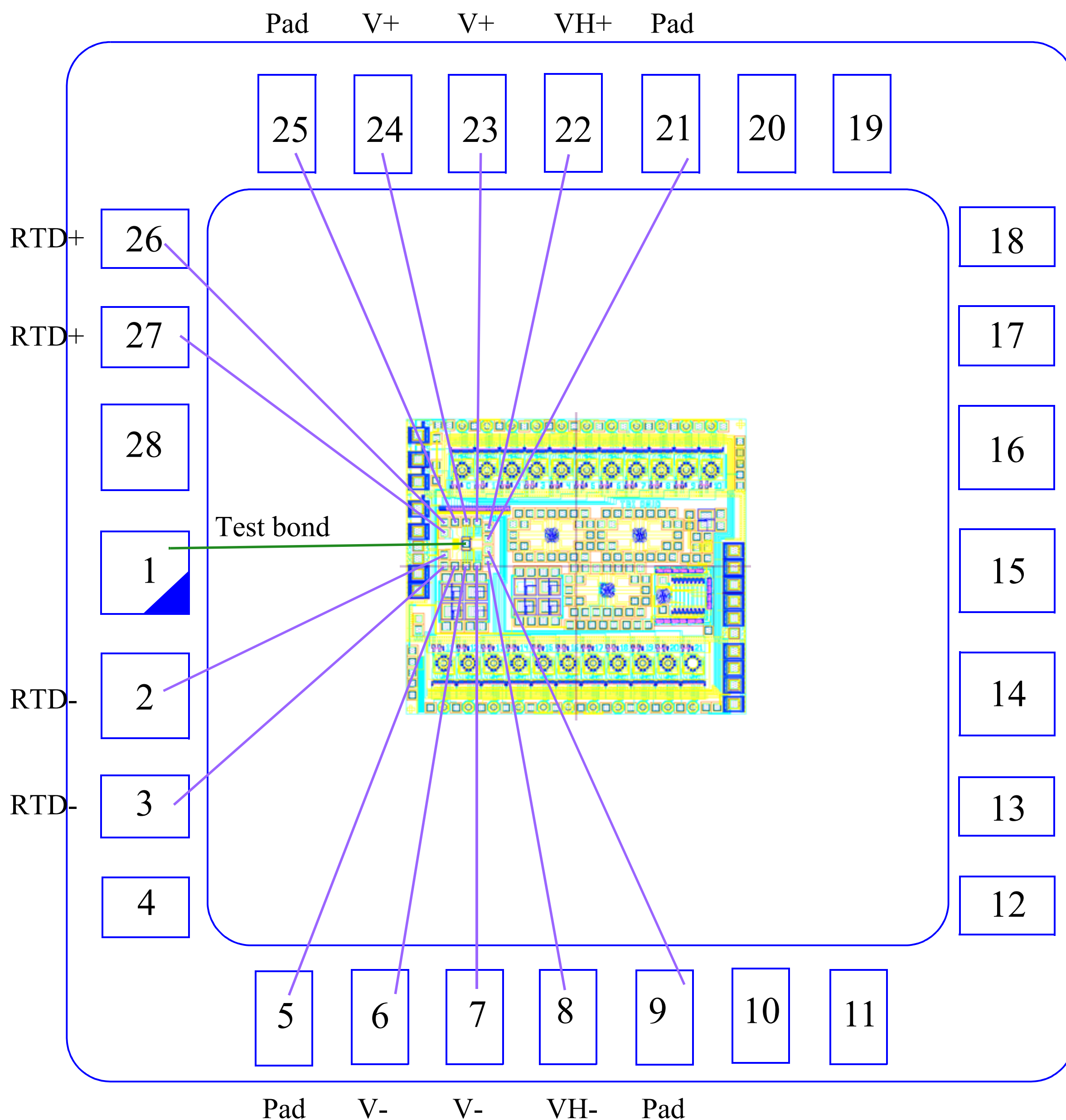

Appendix F: Bonding diagrams for the MISM chip

Bonding Diagram 1
Microheater ground on die paddle
Test bonds to outer ring

Package Type: SB02806

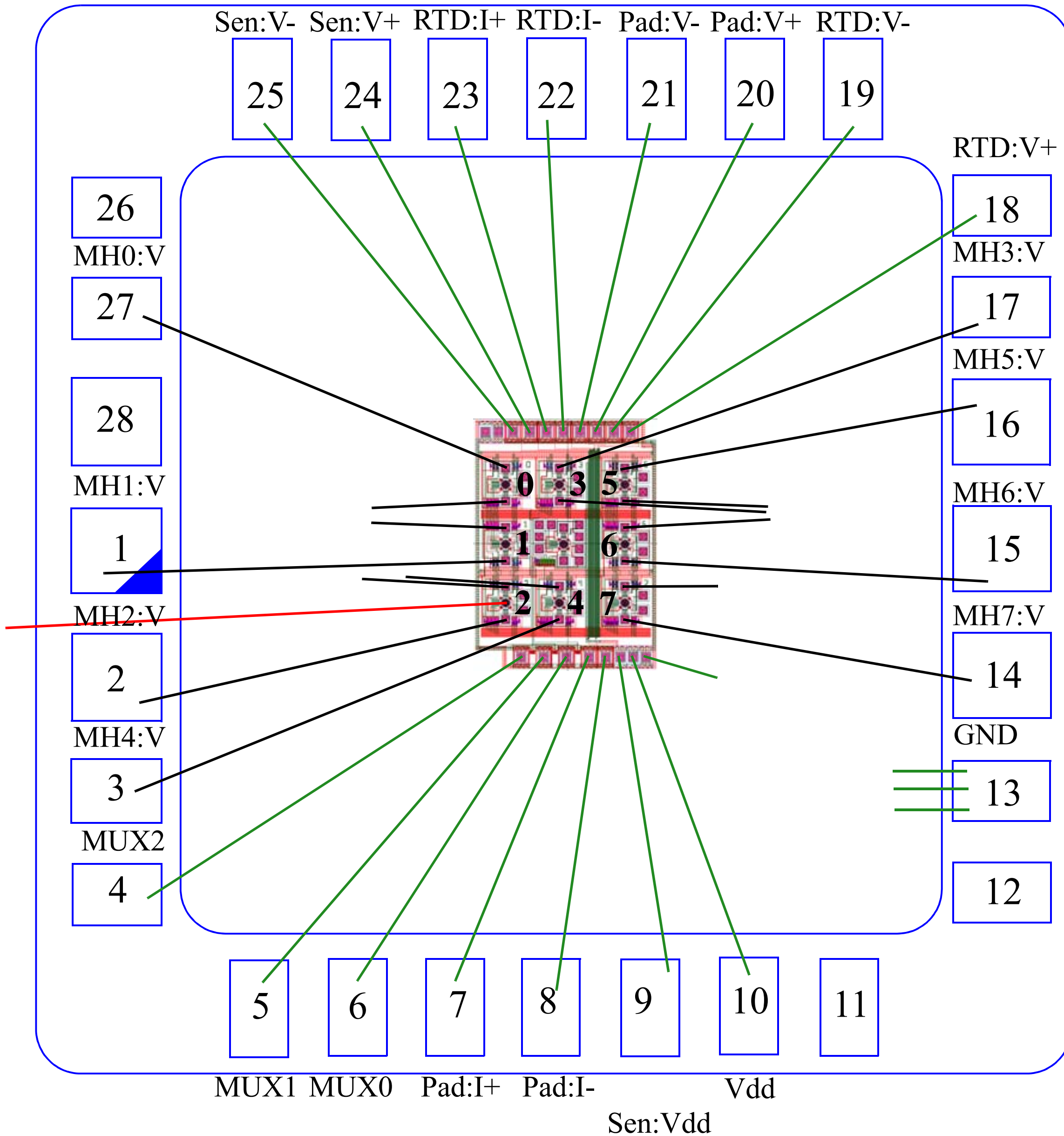

Substrate used as common ground for all components
including heaters

Bonding Diagram 2

Grounds separate, some microheaters share grounds, test bonds to outer ring

Package Type: SB02806

Available from Spectrum Semi

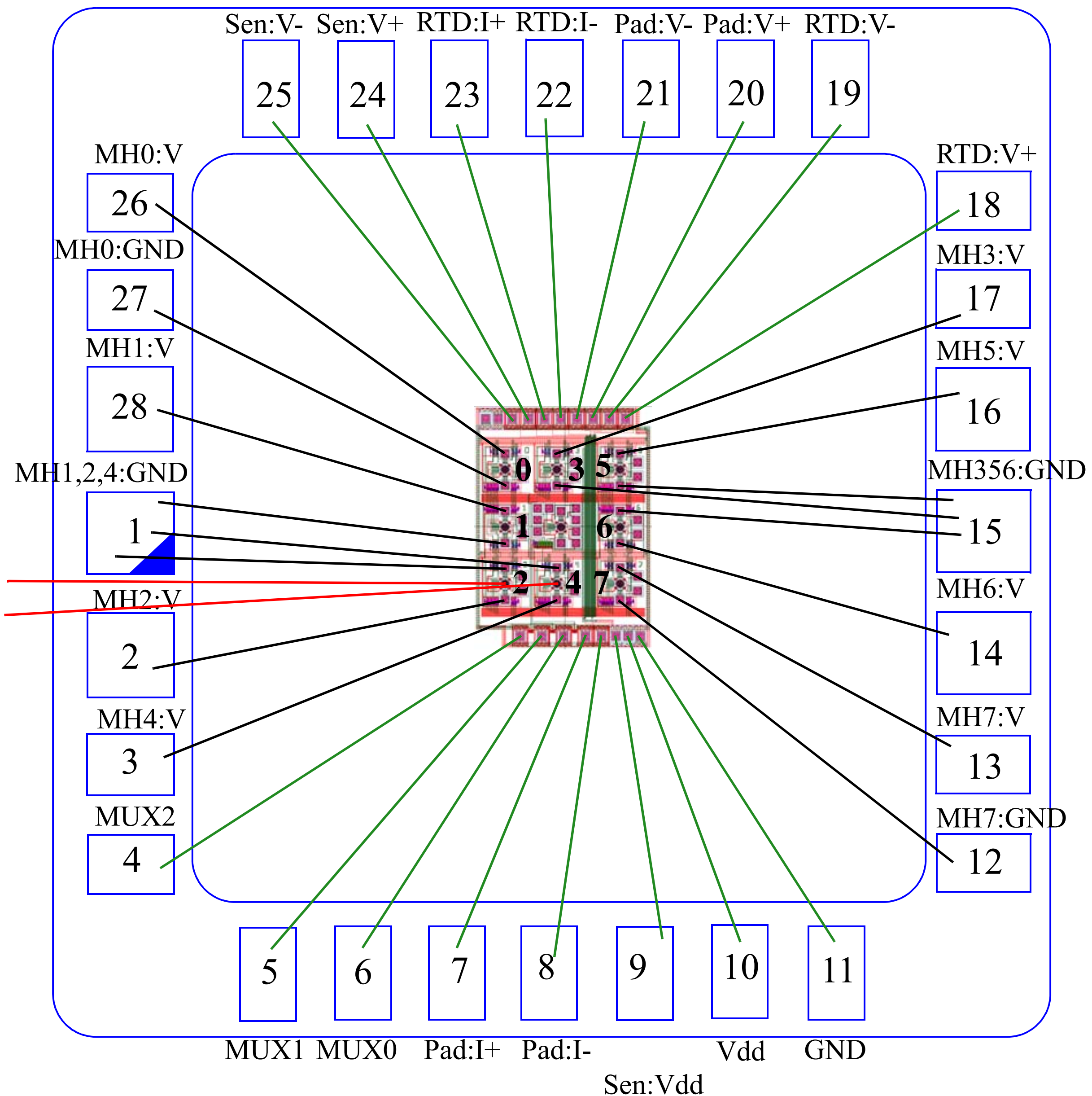

Neighbouring power grounds are shared

Green - Digital inputs and analog outputs

Black - Microheater power and ground. To enable individual power control one possibility is: One microheater has an external 20ohm resistor applied between it and the power source and controls the power source's voltage directly. The other 6 attached microheaters all have variable resistors that range from 0-40ohms and this resistance can be controlled from a DAQ.

Red - Test wirebonds are not all shown. 2nd bonds go to substrate or outer metallized ring on the package.

Bonding Diagram 3

Whole chip common ground on die paddle, test bonds to shared leads

Package Type: SB02806

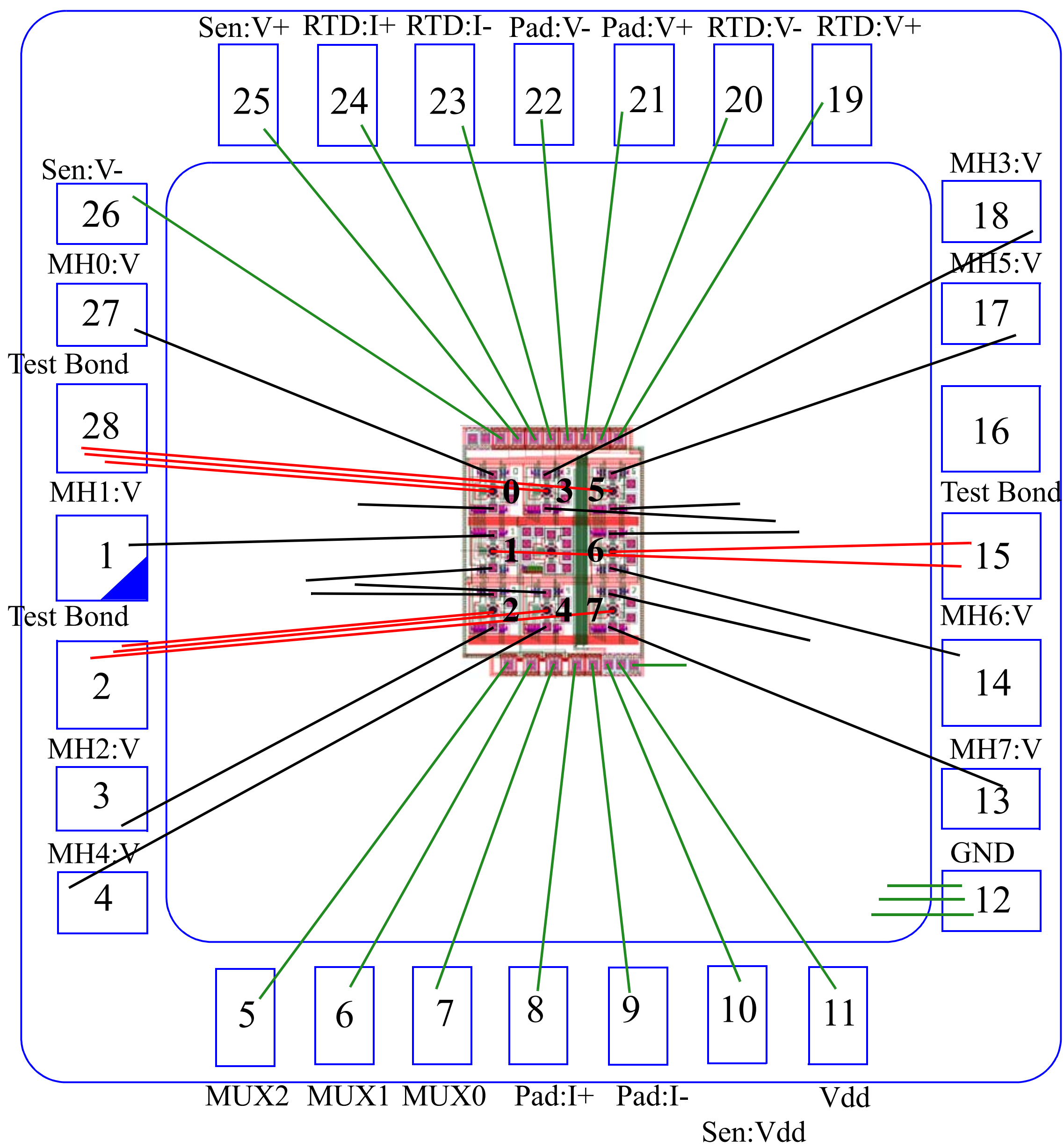

Bonding Diagram 4

Three (3) microheaters using auxiliary pads for pad resistance. Whole chip common ground on die paddle, pad resistance to leads, test bonds to leads

Package Type: SB02806

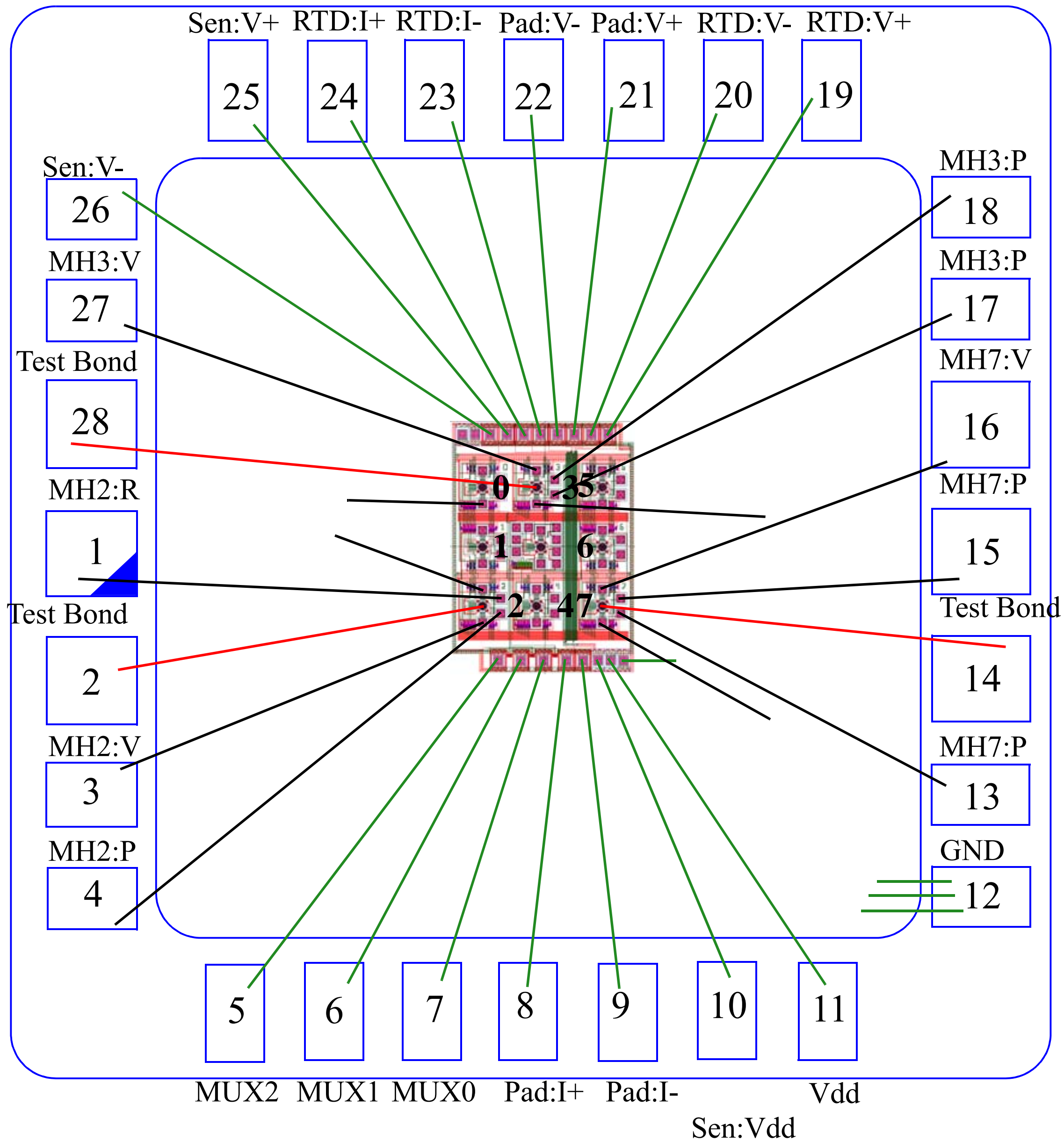

Bonding diagram for use of auxiliary pads for the pad voltage measurements in case the bus lead resistance is too high.

Only 3 pads can be connected at a time using this method however with some re-arrangement of the bonding connections the chip can be re-used by connecting to a different set of test pads.

MH# stands for microheater #, the V stands for voltage power, the P stands for pad resitance voltage leads.